technische universität
dortmund

Photon echo from trions in semiconductor quantum wells and quantum dots

DISSERTATION

presented to the Faculty of Physics of the Technische Universität
Dortmund, Germany
in partial fulfilment of the requirements for the degree of

DOKTOR RER. NAT.

Author : Alexander Kosarev

Technische Universität Dortmund, Germany,

March 2023

Abstract

The present work is dedicated to the study of the ultrafast coherent dynamics of the excitonic complexes localized in semiconductor nanostructures. We consider the optical control of the optical and spin coherence of the negatively charged excitons using the photon echo technique. In the first two chapters, we overview the basic knowledge of the research area and the experimental techniques. In the third chapter, we considered the freezing of the dephasing in the inhomogeneously broadened ensembles of InGaAs quantum dots driven by the application of a resonant control pulse with an area of multiple of 2π. The freezing of dephasing allows us to vary the timing of the photon echo by up to 5 ps, which even slightly exceeds the echo duration. In the fourth chapter, we consider the resident electron dynamics in the CdTe quantum well. Long-lived three-pulse photon echoes in combination with the pump-probe Kerr rotation allowed us to analyze comprehensively the resident electron dynamics since they are differently impacted by the hopping of the resident electrons between the different localization sites. From the data, we evaluate the hopping rate all-optically. In the fifth chapter, we demonstrate the long-lived three-pulse photon echoes from the ensembles of the InGaAs quantum dots. It allowed us to extend the coherent optical response by at least an order of magnitude. We show that the transverse g-factor of the heavy hole in the trion state strongly impacts the temporal evolution of the system, and therefore modifies the long-lived three-pulse photon echo signal.

Kurzfassung

Die vorliegende Arbeit widmet sich der Untersuchung der ultraschnellen Dynamik exzitonischer Komplexe, die in Halbleiter-Nanostrukturen lokalisiert sind. Wir betrachten die optische Kontrolle der optischen und Spinkohärenz der negativ geladenen Exzitonen unter Verwendung der Photonenechotechnik. In den ersten beiden Kapiteln geben wir einen Überblick über das Grundwissen zum Forschungsgebiet und den Versuchstechniken. Im dritten Kapitel betrachteten wir das Einfrieren der Dephasierung in den inhomogen verbreiterten Ensembles von InGaAs-Quantenpunkten, angetrieben durch das Anlegen eines resonanten Steuerpulses mit einer Fläche von einem Vielfachen von 2π. Durch das Einfrieren können wir das zeitliche Maximum des Photonenechos um bis zu 5 ps variieren, was die Echodauer sogar geringfügig überschreitet. Im vierten Kapitel betrachten wir die Dynamik von residenten Elektronen im CdTe-Quantentopf. Langlebige Dreipuls-Photonenechos in Kombination mit der Pump-Probe-Kerr-Rotation ermöglichten uns eine umfassende Analyse der Dynamik von residenten Elektronen, da sie durch das Springen der residenten Elektronen zwischen den verschiedenen Lokalisationsorten unterschiedlich beeinflusst wird. Aus den Daten werten wir optisch die Hopping-Rate aus. Im fünften Kapitel demonstrieren wir die langlebigen Dreipuls-Photonenechos von InGaAs-Quantenpunkt Ensemblen. Es erlaubte uns, die kohärente optische Antwort um mindestens eine Grössenordnung zeitlich zu erweitern. Wir zeigen, dass der transversale g-Faktor des schweren Lochs im Trion-Zustand die zeitliche Entwicklung des Systems stark beeinflusst und daher das langlebige Dreipuls-Photonenechosignal modifiziert.

Contents

Chapter 1

Introduction

Semiconductor heterostructures were developed over 50* years ago [Alf+76] and to this day remain a keystone of modern high technologies. The most noticeable achievements were attained by Nobel prizes: for instance, in 2000 the Nobel Prize was granted for developing semiconductor heterostructures used in high-speed- and optoelectronics [Alf01; Kro01] and for the concept of the integrated circuit [Kil01], or in 2014 for the invention of efficient blue light-emitting diodes which has enabled the production of bright and energy-saving white light sources [Nak15].

The current development of semiconductors is focused not only on the miniaturization of the lithographic process but also on the employment of low-dimensional nanostructures. When the smallest linear size of the structure reaches a certain limit [EE82; Gru10] the dimensional quantization starts to contribute to properties of the system [Li+21; Yan+21]. The most noticeable are changes in carrier mobility [Dat97], energy, and density of states [Gru10; Fox06]. The former is important for electronic devices, while the latter can sufficiently improve the performance of optoelectronic devices which attracted a lot of attention to it.

In particular, usage of such nanostructures as quantum dots (QDs) and quantum wells (QWs) improved the performance of the existing devices such as lasers [Nis+17; AS82], solar cells [Sel+20; Sog+16], transistors [MG19; He+21], displays [Yan+20], and so on. The devices were initially developed using bulk semiconductors, while the nanostructured materials were embedded here for higher performance and better properties of the devices. The main properties of the semiconductor and the nanostructures are discussed in Chapter 2.

On the other hand, the nanostructures have uncovered a completely new area of

*The concepts have appeared even earlier, for instance: Shockley, W., 1951, U.S. patent 2,569,347 (filed June 26, 1948)

semiconductor science and technologies, allowing deterministically design the quantum emitters and manipulate of their state. Operation with the quantum emitter localized in nanostructure as QDs, which can be considered as integrated-in-chips "artificial atoms" [Rod+20; Sta+04] which are well compatible with the existing electronics. At the same hand, compared to color centers in crystals such as NV-centers in diamond, silicon carbide, or rare earth ions, optical transitions possess large oscillator strength which allows one to perform optical initialization on femtosecond time scale.

In semiconductors, the electron-hole pairs are considered as a so-called exciton – which is a quasiparticle. They can be well approximated by the two-level system (TLS or *qubit*) and therefore are the subject of interest in quantum technologies. The exciton can form complexes with the resident (equilibrium) electrons, holes, donor atoms, or even other excitons. The excitonic complexes are subject to great interest because of their unique properties such as selection rules, the ability of optical access to the resident electron, or the ability to emit entangled photons as biexciton can [Bay19]. Modern semiconductor technologies allow one to deterministically grow a nanostructure, where the excitons can have a certain spectral position and density, or be specifically charged. It makes the nanostructures a decent platform for modern quantum technologies.

A special interest deserves coherent control [Kim+11; Li+03] of the quantum state of the excitonic complexes or even storage of the quantum information [Kro+04; Lan+14]. The largest attention is paid to the epitaxially grown QDs [Bay19], which seem to be a perfect candidate for quantum technologies since their high density of states, well-defined optical selection rules, large oscillator strength, and long decoherence time limited by optical recombination [Bor+01; Pre+08]. The QDs can be initialized and controlled coherently on picosecond or even sub-picosecond timescales [Bon+98; Fli+04]. One can clearly see robust Rabi oscillations in the system of QDs [Pol+16; Zre+02; Ram+10; Suz+16; Wig+18], or adiabatic rapid passage [Wu+11; Sim+11]. On the single QD were implemented Ramsey fringes, showing a possibility of the optical phase manipulation [Stu+06; Vas+10].

Photon echoes (PE) are a powerful technique, allowing one to perform coherent manipulation of the quantum states. Since its first observation in ruby in 1964 [Kur+64], it was studied in various systems as atom vapours [Mos+79], rare earth crystals [TS74] or semiconductors [Web+91; Nol+90; Sch+85]. The behaviour of the PE reflects numerous of the quantum system properties such as T_1, and T_2. For instance, the dependence of the PE amplitude with respect to the polarization of incident pulses allows the revealing of the level structure [Pol+19]. It enables one to determine if the coherent response originates from neutral or negatively charged exciton. Special attention deserves spin-

dependent PE, which involves the spin degrees of freedom of the excitonic complexes. It allows to see anisotropy of the g-factors [Pol+20b; Tri+21], spin dynamics of the resident electron[Lan+14; Sal+17b].

The PE technique allows one direct access to the coherent dynamics of the system in spite of the inhomogeneous broadening of optical transitions. This is the main feature of PE. In semiconductors, especially in QDs, the inhomogeneous broadening is very large. Therefore, we use PE technique in the current work.

The *work is dedicated* to the study of the ultrafast dynamics of the excitonic complexes localized in the nanostructures. In Chapter 4, we study the behaviour of the inhomogeneously broadened ensemble of QDs, and the method to inhibit its dephasing by an action of the resonantly tuned 2π-pulse. In Chapter 5 we considered the microscopic dynamics of the resident electrons using a combination of the long-lived three-pulse photon echo and time-resolved Kerr rotation. The technique has allowed us to measure the localization time i.e. the time the resident electron spends on the site between hops. In Chapter 6 we demonstrated long-lived 3PE in charged QDs, which is manifested in a significant extension of the time of coherent response by one order of magnitude from 0.5 to 4 ns.

Even though a single quantum dot can be used for many purposes, many experiments were performed on the single quantum dot in order to avoid inhomogeneities, e.g. for the resonant frequency of optical transition and charge state. Nevertheless, usage of the ensembles is advantageous for the efficient coupling of the excitons with the light [Lvo+09; Tit+10]. The biggest drawback of the ensembles of QD is an unavoidable inhomogeneous broadening originating from their self-organization growth method [SK37]. It results in a rapid dephasing, which vanishes the macroscopic polarization. Nevertheless, the coherence of each particular QD preserves for sufficiently long times reaching nanosecond timescale [Bor+01].

Thus, control of the dephasing or rephasing in inhomogeneously broadened ensembles is important for modern quantum technologies. The Chapter 4 of the current work is dedicated to a method of the dephasing (rephasing) control. We show how the coherent 2π-pulse or multiple numbers of 2π leads to an inhibition of dephasing (rephasing) during the pulse action. We used the two-pulse photon echo technique to detect modification of the phase evolution since it forms after alternating dephasing and rephasing of the inhomogeneously broadened ensemble. We have experimentally observed the effect, described it by a model, and reproduced the observed signal by numerical simulation. The considered method is universal and can be applied to any inhomogeneous ensemble which can be coherently driven with a Rabi frequency exceeding the broadening of the ensemble.

Despite all the advantages of the excitonic complexes for manipulation and storage of quantum information, they are always limited by the optical recombination time i.e. below 1 ns [Sal+17a]. Usually, spin relaxation times are sufficiently bigger than the optical recombination times and reach units of nanoseconds [Lan+14]. It makes the resident electrons (equilibrium, not photoexcited) rather attractive objects to store the quantum information in. When the optically addressed state has orbital or/and spin angular momentum, the splitting of these states in the applied magnetic field gives an additional degree of freedom that can be involved to store the quantum information [Ale+83; Rub+04; Lan+12]. A good instance is a negatively charged quantum dot, where the elementary optical excitation is trion. Its ground state is a single electron having a spin of $1/2$ and the excited one is a trion having a total angular momentum of $3/2$. It is possible to make a transfer of the optical coherence into the spin system as was shown for instance in work [Lan+12] using the photon echo technique. In the work [Lan+14], the optical coherence was stored into the spin of the resident electron using the three-pulse photon echo technique, and afterwards successfully retrieved and formed the photon echo which was detected on the timescale significantly longer than the lifetime of the trion.

Nevertheless, the transfer of the coherence to the resident electrons requires an understanding of its microscopic dynamics. On the other hand, when the optical coherence is transferred to the resident electron spin, the loss of coherence will be already driven by the spin relaxation mechanisms. The spin relaxation rate and even certain mechanisms depend on the electron localization time, i.e. the time it spends on the certain localization site between the hopping events. The parameter is rather complicated to measure since access to the electron dynamics on the sub-μm scale remained challenging for many years.

In Chapter 5, we have developed a new approach revealing the microscopic dynamics of the resident electrons. Combined application of the widely-used time-resolved Kerr rotation (KR) and a novel long-lived three-pulse photon echo (3PE) techniques allowed us to get access to the microscopic dynamics of the resident electron. We have measured the dynamics of the spin polarization in the magnetic field and found that the spin relaxation times we observe by KR and 3PE are differently affected by the hopping of the resident electrons. The analytical model of the microscopic dynamics allowed us to estimate the resident electron localization time from the difference in the spin relaxation times we observed by KR and 3PE. We have observed different localization times on the potentials of different depths and at different temperatures. We found, that the main spin relaxation mechanism in the particular sample occurs due to a hyperfine interaction of the spin with the nuclei. The mechanism is rather sensitive to

spin localization time. Thus, we have developed an all-optical method to observe the resident electron microscopic dynamics and estimate the resident electron localization time, which impacts spin relaxation. In particular, the rise of the temperature led to a reduction of the localization time and double the spin relaxation we observed via KR time from 4 to 8 ns. The method of resident electron localization time measurement can be used in many systems where the photon echo can be observed.

The considered transfer of the optical coherence to the resident electron spin was so far done in the QWs [Lan+14; Sal+17b; Kos+19], which are sufficiently less suitable for the quantum technologies because of higher excitation-induced dephasing and sufficiently lower decoherence times. Due to a very high inhomogeneous broadening, the spectral density of QDs at certain energies is quite low, which results in low signal amplitudes from them. So the experiment was not possible unless the specially designed sample of InGaAs QDs was grown. The QDs were embedded into the cavity, which increased their interaction with the light. Annealing not only allowed to tune of the optical resonance of QDs to the cavity but also increased their spectral density. The QDs were charged by closely deposited δ-layers of Si, such doping resulted in the majority of the singly charged QDs which are essential for the long-lived 3PE formation. That has ensured a sufficient increase of the photon echo signal allowing us to perform the study described in Chapter 6.

A description of the three-pulse photon echo on the magnetic field was done in the work [Lan+14], where the signal was observed from the CdTe QW where the g-factor of the heavy hole was an order of magnitude smaller than the electron g-factor. In order to simplify the description, the Zeeman splitting of the heavy hole was neglected to be an order of magnitude weaker than the splitting of the electron. Meanwhile, in QDs g-factors of the electron and heavy hole have the same order of magnitude [Tri+21]. Therefore, the existing model was not satisfactory for a description of the observed signal. The extended model has included the heavy hole contribution and now has successfully described the observed signal.

Thus, in the thesis, we considered the optical control of the optical and spin states of the negatively charged excitons using the photon echo technique.

Chapter 2

Physical background

The *first chapter* is split into two parts, the first one dedicates to the overview of basic concepts of semiconductor physics which will be used in the following chapters, and the second dedicates to ultrafast and coherent laser spectroscopy. The second part of this chapter is more specific and covers the photon echo technique and its variations, which are interesting for the fundamental science itself and can be used as a tool to study the properties of semiconductors. Thus, in the chapter, we consider mostly the physical processes, while the technical features of the experimental setup and the samples are given in Chapter 3.

2.1 Semiconductors

Semiconductors were known for a long time, the first time the word "semiconductor" was mentioned by Alessandro Volta in 1782 [Vol82]. Indeed huge attention was attracted to the class of materials when semiconductor devices could first compete with the vacuum tube in the 30th of the 20th century. Nevertheless, the semiconductors could not replace them totally because of difficulties in production and poor reproducibility. The fundamental understanding of the semiconductor's properties and their internal processes was not possible without the solid state theory, which was established only after the creation of quantum mechanics in its modern form in the early 30th [PB55].

The semiconductor research at the time of 40th was focused on the production of devices, but also filled some gaps in the understanding of fundamentals. Afterwards, the well-equipped laboratories remained but shifted their focus from applied to fundamental research. The intensive research of semiconductor science and particularly the implementation of such devices as a transistor resulted in the Nobel prize in 1956

[Sho56]. Semiconductors gave new opportunities to the electronic industry and it has got tend to downscale, which would be impossible with vacuum tube transistors. In the middle 60th Gordon Moore noticed that the density of transistors in integrated circuits grows exponentially, roughly doubling every two years [Moo+65].

Modern semiconductor technologies allow one to design the potential for the charge carriers on the scales about nanometers, which may be achieved by the layer-by-layer growth varying the film compound, self-organization processes, high-resolution masking, and the following etching. That gives the opportunity to create such devices as integrated circuits, or artificial atoms (quantum dots) [Bay19], or high mobility transistors [MG19; He+21].

2.1.1 Energy bands in solids

Firstly the semiconductors were distinguished from the metals by the unusual temperature dependence of the conductivity. The increase in the temperature drops the conductivity of the metal, while the conductivity of semiconductors rises. The dependence takes place due to different conditions of the conduction electrons in the materials. Electrons in semiconductors can only have energies within certain bands, which are separated by the *bandgap* E_g. Nowadays, semiconductor materials are defined primarily by the E_g value, which is in a range from units of tenths up to a few eV.

The existence of band gaps is a key feature of semiconductors. Their origination might be described using two approaches: *tight-binding* and *nearly free electron* approximation. The tight-binding model is the most illustrative since it shows how the bands are formed from the s and p orbitals of the atoms forming the crystal. The semiconductor consists of numerous atoms, and its typical molar concentration has an order of about 10^{22} cm^{-3}. The interatomic spacing is about the orbital size, and therefore the atoms are interacting. That lifts the degeneracy, which is schematically shown in Fig. 2.1(a). Reduction of the interatomic distance transforms to a set of independent s orbitals into *conduction band*, the p orbitals into the *valence band*. It is fair for the mainstream materials as Si, A_3B_5, and A_2B_6, but can differ, for example in lead halide perovskites [Kir+22]. The width of the band is proportional to the overlap of the neighbouring in the crystal atoms' wavefunctions. In the approach, the band gap is a reasonable heritage of the inter-level energy spacing [Gru10].

The electrons fill the system up to the Fermi level, which is usually placed within the bandgap in the undoped semiconductors. So the valence band is filled by electrons while the conduction band is empty, the sharpness of the borderline depends on the temperature. The doping or impurities can vary the Fermi level position. If the Fremi level lowers the holes appear in the valence band, and if it is higher the electrons

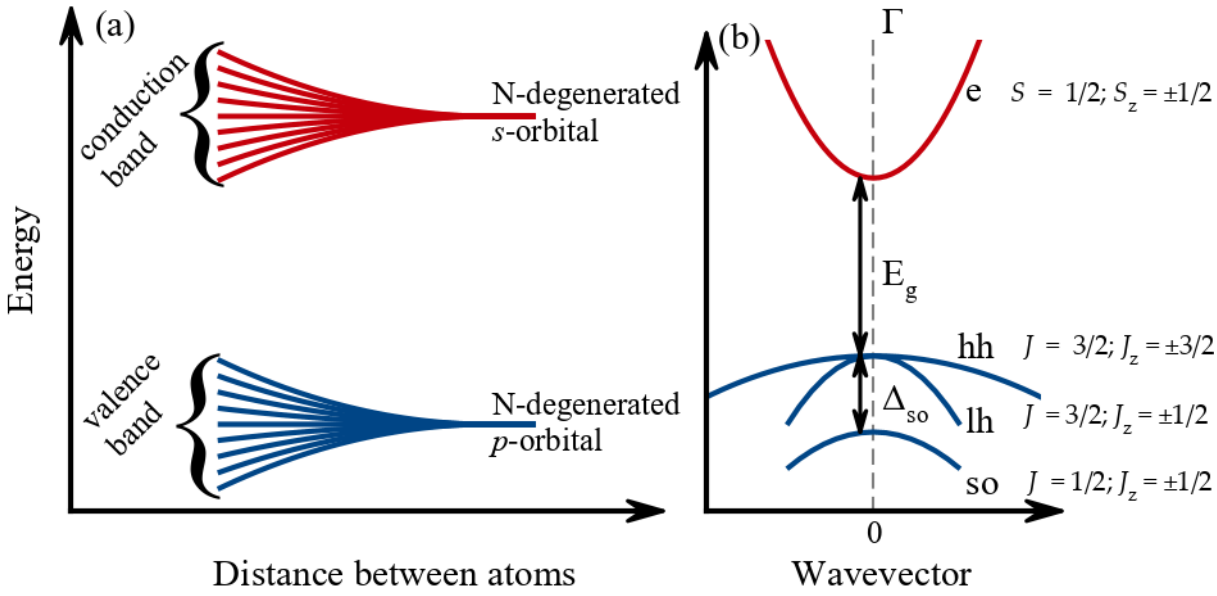

Figure 2.1: *(a) Formation of the bands due to the lift of the degeneracy of the discrete atomic levels with atom convergence in the tight-binding approximation. (b) Band structure of the direct bandgap semiconductors with a zinc blend structure on the example of GaAs around the* Γ *point.*

appear in the conduction band.

Despite the atoms in the crystal being in the sp^3 hybridized states, the consideration in terms of s and p is quite valid since it describes well the level structure in the semiconductors. The s and p orbitals have different angular momentum $\vec{l}$, 0 and 1 respectively. The electron has spin $\vec{S} = 1/2$. Due to the spin-orbit interaction the total angular momentum of the state $\vec{J} = \vec{l} + \vec{S}$. The possible configurations correspond to the conduction and valence band:

- conduction band $\vec{l} = 0, \vec{S} = 1/2$: here $\vec{J} = \vec{S}$, and $\vec{J}$ is a good quantum number i.e. preserves in time.
- valence band: $\vec{l} = 1, \vec{S} = 1/2$: here the total spin is $\vec{J} = 3/2$ and $\vec{J} = 1/2$, here the total spin is a good quantum number

Thus, from that we obtain the four states, which have different sets of quantum numbers:

- conduction band $S_z = \pm 1/2$
- heavy hole band: $J = 3/2, J_z = \pm 3/2$

- light hole band: $J = 3/2, J_z = \pm 1/2$
- split-off band: $J = 1/2, J_z = \pm 1/2$.

The main difference between the bands is their dispersion relations $E(\mathbf{k})$ defined by the effective masses m^* and their energy split. The $E(\vec{k})$ of the four sub-bands are depicted in Fig. 2.1(b), where we show them in the vicinity of the Γ point i.e. a centre of the Brillouin zone having wavevectors close to zero. Here the energy dependencies on the wavevector are parabolic:

$$E(\mathbf{k}) = \frac{\hbar^2 \mathbf{k}^2}{2m^*} \tag{2.1}$$

Since $\hbar\mathbf{k} = \mathbf{p}$, the expression reminds the classical motion of the free particle. The example in Fig. 2.1(b) corresponds to the GaAs parameters, which we show below as an instance. The highest effective mass has a heavy hole, which is the closest to the free electron, that $m_{\mathrm{hh}} = 0.51 m_0$, where m_0 is a free electron mass. At the Γ point the energies of the heavy hole and the light hole are the same, but due to the smaller effective masses, $m_{\mathrm{lh}} = 0.082 m_0$ the curvature of the light hole is steeper. The light hole effective mass in zinc blende structures is usually close to the electron effective mass, which is in our case $m_{\mathrm{e}} = 0.063 m_0$. The GaAs has a direct band gap, which means that the minimal value of E_{g} is at the Γ point. Numerous materials such as AlAs or Si have an indirect band gap, where the minimal band gap is between the hole in the Γ point and the electron in the X point. At the GaAs Γ point the split-off band has lower energy, and the offset value $\Delta_{\mathrm{so}} = 0.34$ eV depends on the spin-orbit coupling parameter. The effective mass in the split-off band $m_{\mathrm{so}} = 0.15 m_0$. Certain values differ from one to another material, but the ratio between them is roughly the same in mainstream A_3B_5 and A_2B_6 alloys.

The most comprehensive description of the bands might be done by the 8-band or 12-band $k \cdot p$ model, but the mentioned above effective mass approximation covers most of the possible applications when the $\mathbf{k}$ is close to the Γ-point. According to the Kane model [Kan57], the effective masses are defined via the E_{g}, Δ_{so} parameters. Simply the effective masses may be estimated as:

$$\begin{aligned} m_e &\approx m_{lh} \approx m_0 \frac{E_g}{E_{\mathrm{P}}}, \\ m_{hh} &\approx m_0 \frac{3E_g}{2E_{\mathrm{P}}}, \\ m_{so} &\approx m_0 \frac{3}{E_{\mathrm{P}}}(E_g + \Delta_{so}) \end{aligned} \tag{2.2}$$

where E_{P} is an energetic parameter having values in range of $20 - 25$ eV in A_3B_5.

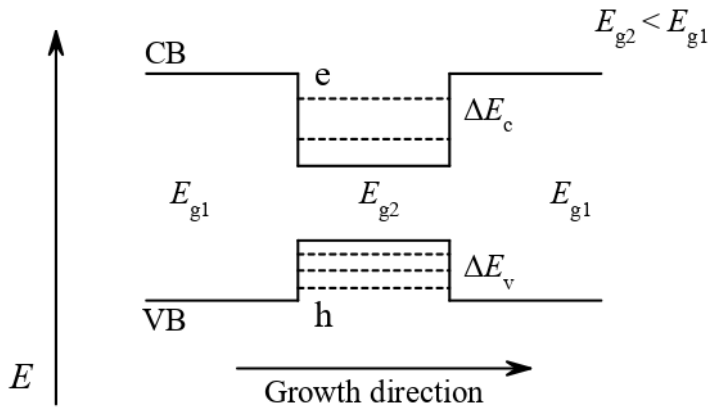

Figure 2.2: *The conduction band (CB) and valence band (VB) potentials along the growth direction of the double heterojunction. An example of nanoheterostructure.*

2.1.2 Heterostructures and nanostructures

The merging of two semiconductors with a different E_g forms a heterostructure. It allows one to engineer the potentials for the electrons and holes [Cap87; Alf98]. The possible hetero couples might be found for example in work [FS04]. The heterostructures form such devices as diodes, and their modifications with varying (I-V) properties, transistors and etc. [Cap87]. The mismatch of the bandgaps is shared between the conduction band (CB) and the valence band (VB) according to the *band offset* ΔE_c for the CB and ΔE_v for the VB.

Sandwiching one semiconductor between others forms a double heterostructure. For us, the most interesting case is when the narrow band gap semiconductor is surrounded by the wide band gap since the carriers in the narrow band gap semiconductor are in the potential well. We consider here the only heterostructure of the first type, where the potential of the electrons and holes is always lower and correspondingly higher in the narrow band gap material as shown in Fig 2.2. The double heterostructure of the first type may already be used as an effective light emitter. Application of the electron and hole current from the different sides creates an inversion of the population within the thin film making it a bright light emitter.

If the well is narrow enough to be comparable to the electron-hole pair Bohr radius, dimensional quantization starts to modify the properties of the heterostructure and it can be already treated as a quantum well. The carriers are restricted in motion in one direction and have only two degrees of freedom. When the dimensional quantization energy exceeds the coulomb interaction between the electron and hole, we can consider the electrons and holes separately. They form a set of quantum states as shown in Fig. 2.2 by dashed lines.

The nanostructure usually implies the engineering of the material properties on a size of about 100 nm and below. Heterostructures of such size are sometimes called nanoheterostructure. Modification of the compound layer by layer allows us to vary the E_g on the scales far below the Bohr radii of the carriers and therefore allows one to control the energy of the dimensional quantization. Moreover, the properties of the same material in the bulk and thin film in heterostructure sufficiently differ because of strain, piezoelectricity-driven electrostatic fields, and subsequent changes in the band structure. Such changes can be strong, but predictable and can be properly calculated for engineering the quantizing potentials [[Gru+95; KC21]].

The number of carriers with a certain energy in the semiconductor is limited by the $DOS(E)$. When the motion of the carrier in some direction is restricted by dimensional quantization, the system can be called *low-dimensional system* or a system of reduced dimension. A considerable advantage of nanostructures is an ability to reduce dimensions, that accompanied by a rise of the density of states $DOS(E)$ value.The limitation originates from the volume in the phase space the system takes [Dat97; Gru02]. An increase of the $DOS(E)$ due to the dimensional quantization in nanostructures is one of the most significant advantages since it rises the maximum possible number of the electron-hole pairs emitting light and therefore can increase the performance of the light-emitting devices [Alf01].

The density of state functions of the bulk and reduced dimension materials are shown in Fig. 2.3. The blue line corresponds to the DOS in the bulk material (3D), and its value rises as a square root $DOS^{3D}(E) \propto \sqrt{(E)}$ stepping away from the edge of the bandgap [Kit05]. The very low density of states on the band edge is a huge disadvan-

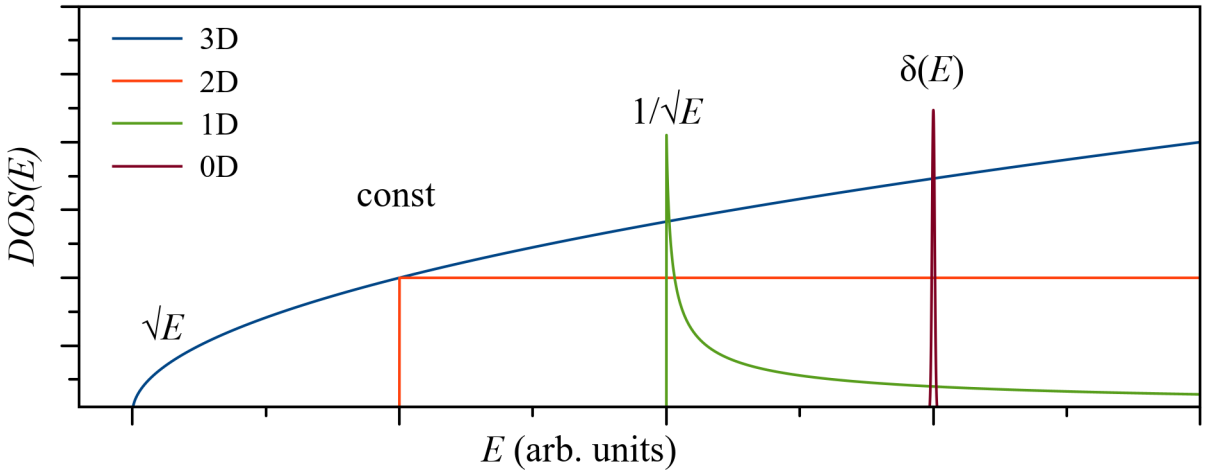

Figure 2.3: *Schematic representation of the density of states $DOS(E)$ in the bulk material, and the reduced dimension materials.*

tage of the bulk material for the applications. The 2D material i.e the quantum well (QW), has a constant density of states independent of the energy $DOS^{2D}(E) \propto const$. Since the constant density appears step-like, at the band edge density rises sufficiently sharper in comparison to the bulk. We show the density functions here with the offset, to highlight the dimensional quantization energy. The 1D system is a quantum wire, that has an extremely high density of states at the band edge since $DOS^{1D}(E) \propto 1/\sqrt{(E)}$ has a singularity here. The 0D case is called a quantum dot since the carriers are quantized here along all three directions and have no degrees of freedom. Its density of state $DOS^{0D}(E) \propto \delta(E)$, which is usually considered as its significant advantage.

Despite the formally infinite DOS value in QD, it can not, unfortunately, be reached. First of all, the finit lifetime of the state makes the line spectrally broadened. Moreover, in ensembles DOS is limited by a number of QDs and caused by QDs size distribution inhomogeneous broadening. The broadening is usually considered the most sufficient drawback of the QD ensemble usage. The spectral width of the distribution may reach 40 meV [Kos+19], which is significantly larger than a single QD linewidth being about 3 μeV [BF02].

The broadening can be reduced by post-growth annealing. The temperature must be high enough to activate interatomic diffusion processes around the QDs [Hei+98]. The diffusion leads to the QD shape change, which results in the narrowing of their size distribution and blue shift of the optical spectra [Pet+07]. Thus, annealing is a method of fine-tuning the QD optical transition frequency and also raising their spectral density.

The carriers strongly localized in such nanostructures as QDs are decoupled from the bands of the bulk, which increases their decoherence time and makes them attractive to quantum technologies. In particular, in the works [Kos+20; Kos+22; Moo+11; Bor+01] was shown, that in the QDs systems decoherence time is limited by the radiative decay, while in the QWs other mechanisms contribute as well [Lan+14; Kos+19].

Another advantage of the nanostructured material is flexibility in the quantizing potential engineering. Variation of the compound in such materials as $In_xGa_{1-x}As$, $Al_xGa_{1-x}As$ or Si_xGe_{1-x} allows one to obtain the needed value of the bandgap and obtain its spatial profile.

The QDs and QWs can be grown with a precision of up to 1 monolayer and have good reproducibility by industrial technologies such as molecular-beam epitaxy (MBE) and metalorganic chemical vapour deposition. The nanostructure grows on the monocrystalline wafer substrate. The growth is based on the slow layer-by-layer deposition of atoms on the surface of the crystal, so they are placed in the continuation of the atomic

planes. The planar *growth regime* is known as *Frank-Van der Merve growth mode*, which takes place when the lattice constants of the substrate and the growing film are close enough. Any mismatch between the substrate and film limits the maximal film width, the limit might be found by the Matthews-Blakeslee formula [MB74].

The QDs may be formed by either *Vollmer-Weber* or *Stranski-Krastanow* growth mode. The former is based on the deposition of a material, which is not wetting the substrate and gathers as droplets on the surface. Usually, it requires a giant lattice mismatch exceeding 10 %. The Stranski-Krastanow mechanism [SK37] is widely used since the mainstream InGaAs/GaAs QDs are usually grown by this growth mode. In this mode, the first couple of layers grow planar, but the following layers form small islands i.e. QDs. Variations of the temperature, atom fluxes, or delay between layers allow one to obtain the QDs with the required parameters [Ser+12].

2.1.3 Exitonic complexes in semiconductors

An electron in a semiconductor can belong to one of the bands as shown in Fig. 2.1(b). Absorption of the light drives a transition of the electron between the bands, here the photon energy must correspond to the energy between the bands, and photon polarization must fulfill the optical selection rules.

A vacant place in the valence band is usually considered as a quasiparticle – *hole*. Despite the hole being a complicated concept describing the behaviour of the many electrons in the valence band, the association of the quasiparticle to the phenomena is valid and is widely used. Hence, a positive electric charge, lifetime, spin relaxation time, mobility, and other parameters might be associated with the hole. The valence band comprises of three sub-band comprising of *heavy hole*, *light hole* and *split-off hole*. Since the hole is a many-electron effect belonging to the *p*-like band, its parameters as effective mass m^* and the *g*-factor are sufficiently more anisotropic in comparison to the CB electrons. Below we consider only the heavy hole since it has the lowest energy in QD and QW we focus on.

The exciton

Samely to the hydrogen atom, the Wannier-Mott *exciton* is formed by the Coulomb interacting positively charged hole and negatively charged electron in the crystal. Because of the big dielectric permittivity and the small effective mass, the Rydberg value sufficiently reduces and the Bohr radius rises with respect to atomic one. The transfer of an electron from the top of VB to the bottom of CV forms a hole in the VB, that action can be considered as a creation of the exciton supposing electron and hole to be electrostatically bound. The electrostatic binding makes the exciton transition energy E_X lower than the band gap E_g by the binding energy as shown in Fig. 2.4(a&b). The

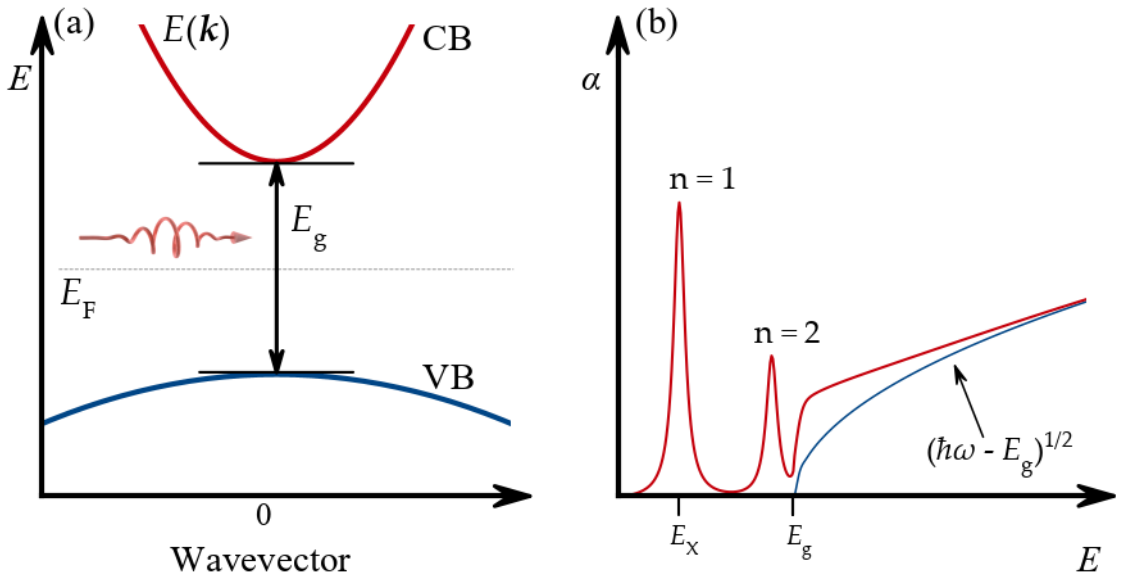

Figure 2.4: *The exciton resonance in the interband transitions. (a) The photon transfers an electron from the VB to the CB; (b) edge of the fundamental absorption band blue line – in absence of the exciton, red line – the edge is modified by the excitons.*

binding energy depends on the electron and hole wave function spatial overlap and electric permittivity of the media. Its value is typically higher in the nanostructures and is in a range from units to tens of meV. If the binding energy is lower than the thermal energy $k_B T$, the exciton rapidly dissociates, here k_B is The Boltzmann constant and T – is the temperature. Nevertheless, in some materials, the binding energy is high enough to see the excitonic effects even at room temperatures [Bol+17].

Treatment of the exciton in nanostructures depends on the relation of Bohr radii of the electron and hole, which may be estimated as $a_B = \hbar^2 \epsilon / m^* e^2$ and the minimal dimension of the nanostructure [EE82]. Here ϵ is a dielectric permittivity and e is the electron charge. In case when the nanostructure is bigger than the a_B, the quantization energies of the electron and hole are lower than the exciton binding energy, and therefore the exciton must be quantized as a whole. The opposite option is applicable when the nanostructure minimal size is smaller than the respective a_B radii, now the quantization energies are bigger than the binding one. It brings us to the consideration of the exciton as electrostatically interacting separately dimensionally quantized the electron and hole. The two mentioned extreme cases as well as intermediate ones are discussed in the work [Eki+85].

The exciton-related resonances are well seen in the optical density or PL spectra at low temperatures. It modifies the band edge by a set of narrow peaks with the cen-

tral energies below E_g as schematically shown in Fig. 2.4(c). The blue line shows the exciton-free interband absorption, while the red line shows the shape of the exciton-modified spectra. One can distinguish here a couple of peaks corresponding to the different principal quantum numbers. The peak has a Lorentzian shape when the system is homogeneous. Thus, we can consider the light-driven interband transition of the electron from the valence band to the conduction band as a creation of the excitons.

In the exciton, the four electron and heavy hole spin projections are possible (see Fig. 2.5(d)). The two states of the antiparallelly oriented S_z and J_z of the electron and heavy hole respectively form the exciton with the total angular momentum ± 1, which are accessible by the light and therefore called *bright exciton*. The parallelly directed S_z and J_z form the exciton with the total angular momentum of ± 2, it is inaccessible by the light and called *dark exciton*. There is also a doubly excited state - *biexciton*, it has total angular momentum of 0. We omit the dark exciton and biexciton in the following consideration since we do not deal with the quasiparticles in the work.

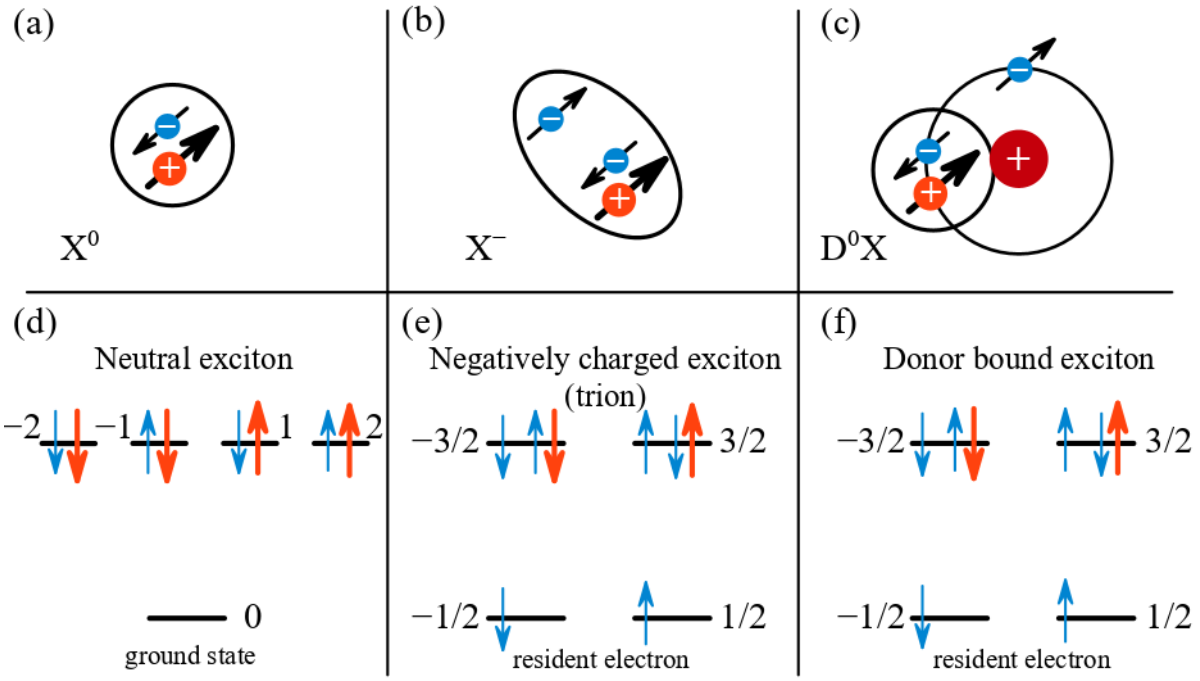

Figure 2.5: *(a-c) Excitonic complexes in solids (d-f) and the corresponding energetical schemes. Here small blue arrows represent the electron and its spin projection $\pm 1/2$. The red thick arrow represents the heavy hole projections of its angular momentum being $\pm 3/2$.*

The exciton can be bound by a charged particle and form *excitonic complex*. We consider here only the free-standing exciton X^0, negatively charged exciton (trion) X^-, and donor-bound exciton D^0X, which are shown in Fig. 2.5(a-c). The X^- is a complex of

the neutral exciton and an extra electron see Fig. 2.5(b). The extra electron is supposed to be thermally equilibrium and is called *resident electron* to delimit it from photoexcited electrons. The X^- can be built only in a system with reduced dimensions where its binding energy is high enough to form the complex.

The ground state of the X^- is a resident electron, which may have two possible spin projections i.e. $S_z = \pm 1/2$. The circularly polarized photon brings the angular momentum of 1, which creates the electron-hole pair, so the projection of the total angular momentum $J_z = \pm 3/2$. According to the Pauli exclusion principle, two electrons of X^- are in singlet state and therefore must differ by at least one of the quantum numbers i.e. spin projection S_z, so the J_z is defined by the hole's spin. There are also triplet states in QDs. But they have higher energy because one of the electrons should be promoted into the higher energy level, i.e. hot trion. See e.g. [**akimov2005electron**]. The donor-bound exciton D^0X, where the resident electron belongs to the donor atom, is structurally the same as the X^-, but its binding energy is slightly higher due to the Coulomb interaction with the donor as we see for example in work [Kos+19].

2.1.4 Optical orientation

Interband transitions

In the bulk A_3B_5 we discussed above, there are four bands of different quantum numbers near the Γ-point as it is shown in Fig. 2.1(b). We remind that the electrons forming CB have angular momentum $l = 0$, and the corresponding wavefunction has the *s*-like symmetry. On the other hand, the electrons forming VB have $L = 1$ and the *p*-like symmetry. To describe the interband transition we assign *hh* to the heavy hole band, *lh* to the light hole band, *so* to the split-off band hole, and *c* to the conduction band, so the *hh-c* is the transition between the heavy hole band and the conduction band and so on [DK11].

Each transition between the states $|A\rangle$ and $|B\rangle$ driven by the light may be associated with the classic dipole $\mathbf{d}$, which is defined by the matrix element of the transition: $\mathbf{D}_{AB} = \langle A| \hat{\mathbf{D}} |B\rangle$, where $\hat{\mathbf{D}}$ is the dipole moment operator. The dipole defines the polarization of the emitted light and its decay time. Calculation of the dipole moments of the interband transitions shows, that the only non-zero components have the following matrix elements: $\langle s| D_X |p_x\rangle = \langle s| D_y |p_y\rangle = \langle s| D_z |p_z\rangle$, they correspond to the transitions between the conduction band and the subbands of the valence band [MZ84]. The light carries the angular momentum of 1 and can drive the only transitions fulfilling the angular momentum conservation.

The transitions between *hh-c*, *lh-c*, and *so-c* are schematically shown in Fig. 2.6 by double-sided arrows. Corresponding dipoles and the relative intensities of the transi-

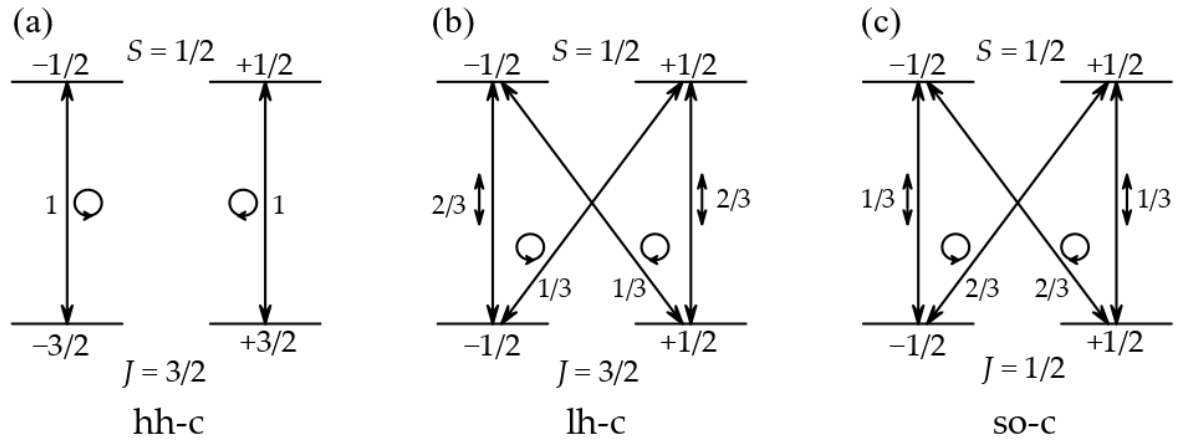

Figure 2.6: *Various dipole-allowed interband transitions and the corresponding dipoles. The numbers near dipole signs correspond to the relative intensity of the transition. Ring arrow corresponds to circular polarization, while vertical arrows to linear polarization. Transitions between (a) heavy hole and conduction bands; (b) light hole and conduction bands; (c) split-off hole and conduction bands. Adopted from [MZ84]*

tions are indicated near each transition. The *hh-c* transitions are formed by these two dipoles, which rotate clockwise and counterclockwise in the plane perpendicular to the wavevector of the light **k**, which is perpendicular to the sample's plane. The transitions *lh-c* are formed by a couple of dipoles oscillating along the **k** direction and the two dipoles rotating in the plane perpendicular to the **k**. The transitions *so-c* have a similar structure to *lh-c*, but the relative amplitudes differ. Here we considered the system in the basis, where the projections of the angular momentum were done on the quazipulse [MZ84].

Optical spin orientation

In absence of the magnetic field, the carriers of the same band with different projections of the angular momenta have the same energy and therefore are equally populated. Let's only consider *hh-c* transition shown in Fig. 2.6(a). In the equilibrium, the electrons are equally distributed in the VB between the $|3/2\rangle$ and $|-3/2\rangle$ states, while the CB is empty. The circularly polarized light σ^+ drives only one of the two possible transitions, it populates the state $|-1/2\rangle$ and depletes $|-3/2\rangle$. The eventual polarization of the electrons in the CB considering *hh-c* transition under σ^+ light is estimated as:

$$S_0 = \frac{N_{-1/2} - N_{+1/2}}{N_{-1/2} + N_{+1/2}} = 100\%. \tag{2.3}$$

where N_i - is a population of the corresponding level.

In the bulk materials, the *hh* and *lh* bands near Γ point are usually degenerate. Here the transitions *c-hh*, and *c-lh* can be driven simultaneously, as shown in Fig. 2.7. The

circular polarization σ^+ drives the only two transitions of the possible: $|-3/2\rangle \rightarrow |-1/2\rangle$ and $|-1/2\rangle \rightarrow |+1/2\rangle$. Since their intensities differ, the state $|-1/2\rangle$ is three times more populated than $|+1/2\rangle$, which results in a polarization of 50%.

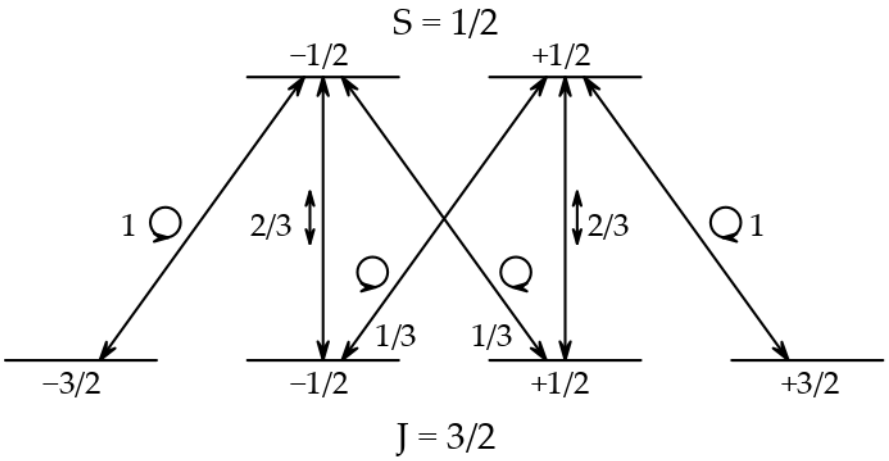

Figure 2.7: *Selectrion rules, dipole orientations and the relative intensities of the transitions between the CB and two subbands of the VB. Ring arrow corresponds to circular polarization, while vertical arrows to linear polarization.*

The spin polarization may be detected by various techniques. The two most known ways to study it are the time-resolved *Kerr rotation* (or *Faraday rotation*) and the *Hanle effect*, which represent the time-resolved and stationary techniques. The Kerr rotation implies analysis of the reflected or transmitted light's polarization, which changes due to the spin polarization. Nevertheless, a certain value or spin polarization is not easy to extract from the Kerr signal. The technique is advantageous to track the complex dynamics of the multiple sub-ensembles or see some dynamical effects as spin mode-locking [Gre+06a; Kir+23]. The Hanle effect [Han24; Par69] is based on the analysis of photoluminescence (PL) depolarization in the transverse magnetic field. It requires however the precise knowledge of the g-factor and the carrier type for which depolarization takes place. Both techniques can be used to study the spin relaxation processes.

2.1.5 Spin relaxation mechanisms

Spin relaxation is a decay of the non-equlibrium spin polarization. It originates from microscopic processes when the electron loses its spin direction. In the model we consider thde spin relaxation takes place under an action of the fluctuating magnetic fields. The field is "effective" and can be formed by different mechanisms. The field can be defined by its amplitude and its correlation time τ_c i.e. the time direction of the fluctuating field remains the same. The common approach is to consider the rooted mean

square value of the spin precession frequency $\sqrt{\langle\omega^2\rangle}$ instead of the amplitude of the field. Thus, spin precession around the randomly directed magnetic field with a Larmor frequency $\sqrt{\langle\omega^2\rangle}$ during the τ_c, afterwards the direction changes randomly and the process repeats. In a while, the initial direction of the spin is completely lost. The intensity of the process may be characterized by the parameter $\sqrt{\langle\omega^2\rangle}\tau_c$, which brings us to the two contrast regimes.

When $\sqrt{\langle\omega^2\rangle}\tau_c \ll 1$, the angle of the rotation that occurs on each step is small, the spin has a slow angular diffusion. In this case, the homogeneous spin relaxation time is defined as $1/\tau_s \propto \langle\omega^2\rangle\tau_c$, where the τ_s is sufficiently longer than the fluctuation correlation time i.e. $\tau_s \gg \tau_c$.

When $\sqrt{\langle\omega^2\rangle}\tau_c \gg 1$, during the τ_c, the spin makes multiple turns around the randomly directed magnetic field. Therefore during $1/\sqrt{\langle\omega^2\rangle}$, the only spin's projection on the random field conserves, while its transverse component destroys. When the magnetic field changes its direction in τ_c, the initial spin polarization disappears. Thus, we see the two-step decay, first stage occurs on the timescale of $1/\sqrt{\langle\omega^2\rangle}$, the second stage on the timescale of τ_c. It results in the ratio $\tau_s \propto \tau_c$.

There are a few mechanisms creating the fluctuating magnetic field. Here we summarize them, but the comprehensive description can be found in work [DK08].

The *Elliott-Yafet Mechanism* [Ell54; Yaf63] is based on the electrical fields occurring due to the lattice vibrations or the field of the charged impurities. The spin-orbit interaction transforms them into an effective magnetic field. The phonons have the correlation time on the order of their inversed frequency. The magnetic field direction and value during the scattering of the impurity depends on a certain collision condition. The correlation time τ_c here is not applicable, since the field exists only during the collision event. With each collision, the electron spin rotates by some small angle ϕ. Assuming the τ_p as a time between collisions, the resulting $1/\tau_s \propto \langle\phi^2\rangle/\tau_p$. The spin relaxation rate is proportional to the impurity or phonon concentration.

The *Dyakonov-Perel Mechamism* [DP54; DP72] determined by the spin-orbit splitting of the conduction band in non-centrosymmetric semiconductors such as GaAs. The effect was first noticed by Dresselhaus in bulk semiconductors [Dre55]. In contrast to the Eliott-Yafet mechanism, the spin rotates in the fluctuating field not during the collisions, but between them. It brings us to the expression $1/\tau_s \propto \langle\phi^2\rangle\tau_p$. Here the spin relaxation rate is inversely proportional to the impurity density.

The *Bir-Aronov-Pikus mechanism* [Bir+75] is based on the exchange interaction between the non-equilibrium electron and hole spins in *p*-type semiconductor by exchange interaction. The spin relaxation rate is proportional to the doping concentration density and dominates in heavily doped semiconductors.

The *relaxation via Hyperfine Interaction with the Nuclear Spins* occurs when the nuclei play the role of the fluctuating fields via hyperfine interaction. Its intensity is usually not high for free carriers, but is important for localized ones.

2.1.6 Lognitudinal and transverse spin relaxation time

In presence of the magnetic field, one usually distinguishes the spin relaxation of the component S_x directed along the magnetic field (longitudinal) and the perpendicular one (transverse) S_{yz}. The former corresponds to the diagonal elements of the density matrix, while the latter to the non-diagonal ones. Therefore one distinguishes the longitudinal spin relaxation time $T_{1,e}$ and the transverse spin relaxation time $T_{2,e}$, the notation comes from nuclear magnetic resonance. The transverse relaxation time is sometimes called spin dephasing time since it impacts the phase of oscillations of the spin in the magnetic field. We add subscript e to delimit with the optical times that will be introduced below.

It is obvious, that if $B = 0$ the system is symmetric and therefore $T_{1,e} = T_{2,e}$. In the magnetic field, the difference is clear since the decay of the transverse component is related to elastic processes, but the longitudinal one to the inelastic. When the splitting $\hbar\omega_L$ of the states in the magnetic field exceeds the thermal energy, the longitudinal relaxation can contribute to the transverse samely to Eq. 2.11.

2.1.7 Impact of inhomogeneity of ensemble

The inhomogeneity sufficiently contributes to the spin relaxation in the ensemble of spins. The inhomogeneously broadened ensemble has a distribution of the Larmor frequencies, so their spectral distribution is broader than the rate of the homogeneous spin relaxation $1/T_{2,e}$. The variation of the Larmor frequencies $\delta\omega$ can originate from the fluctuation of the magnetic field, or variation of the g-factor. If the $\delta\omega$ does not depend on the magnetic field, the inhomogeneity impact can be considered in terms of the g-factor dispersion Δg. In the inhomogeneously broadened ensembles the spin polarization decays with $T^*_{2,e}(B)$, which is defined as:

$$\frac{1}{T^*_{2,e}(B)} = \frac{1}{T_{2,e}} + \Delta g_e \mu_B B/\hbar, \tag{2.4}$$

where B is a magnetic field amplitude, μ_B is a Bohr magneton, and $1/T_{2,e}$ is a (homogeneous) spin relaxation time defined by relaxation processes of the individual spins.

2.1.8 Hanle effect and the spin dynamics in the magnetic field

The Hanle effect is a well-developed stationary technique, it allows obtaining both the spin relaxation time and electron lifetime by measuring the dependence of the PL polarization degree on the transverse magnetic field. The effect originates from the precession of the electron spin in the magnetic field. Under continuous excitation, precession reduces the average projection of the electron spin in the direction of the observation, which defines the PL polarization degree. The dependence of the polarization degree of the PL in the external magnetic field has the shape of a Lorentzian, in which half width on the half maximum is defined by the electron g-factor g_e, the electron lifetime τ, and the spin relaxation time τ_s. If the g-factor is known, one can extract the relaxation times or vice versa.

Despite the maximal possible polarization S_0, the observed polarization of the PL has usually a lower polarization degree due to the spin relaxation, which depends on the ratio of the lifetime and the spin relaxation. If the $\tau_\mathrm{s} \gg \tau$ the spin preserves during the electron lifetime, and therefore the PL polarization degree must be close to the S_0. The opposite case when $\tau \gg \tau_\mathrm{s}$ implies a total spin relaxation before its radiative recombination, so the PL is now completely depolarized. The exact degree of PL polarisation in the absence of the magnetic field can be expressed as:

$$P_\mathrm{PL}(0) = \frac{S_0}{1 + \tau/\tau_\mathrm{s}}. \tag{2.5}$$

The dependence on the magnetic field has the following shape:

$$P_\mathrm{PL}(B) = \frac{P_\mathrm{PL}(0)}{1 + (B/B_{1/2})^2}. \tag{2.6}$$

The dependence has a Lorentzian shape, the parameter $B_{1/2} = \hbar/g_e\mu_\mathrm{B}T_\mathrm{s}$ represents the magnetic field where the polarization of the PL double drops relatively to the zero field. Here we introduced the new parameter T_s - the spin lifetime, which is defined as $1/T_\mathrm{s} = 1/\tau + 1/\tau_\mathrm{s}$ i.e. spin relaxation via radiative and nonradiative channels.

Thus, from the Hanle depolarization curve, one can extract two of the three parameters (g_e, τ_s, τ), if one of them is known, and also S_0. The method is widely used since it gives parameters of the dynamics by a stationary measurement technique, which does not require a pulsed laser. Formulas 2.5 and 2.6 are the solutions of the spin dynamics master equation:

$$\frac{d\vec{S}}{dt} = \vec{\omega} \times \vec{S} - \frac{\vec{S}}{\tau_\mathrm{s}} - \frac{\vec{S} - \vec{S_0}}{\tau}, \tag{2.7}$$

where the $\vec{\omega} = \hbar \mu_B g_e \vec{B}$ is a vector of the Larmor precession, $\vec{S_0}$ is an equilibrium spin state. Here the g-factor is actually a 2^{nd}-rank tensor but may be treated as a scalar when the system is isotropic. In nanostructures, crystalline anisotropy as well as dimensional quantization often brings anisotropy so we consider g-factor as tensor [Pol+20b; Tri+21].

2.2 Dynamics of the quantum state and the Bloch sphere

2.2.1 Two-level system and its description using different formalisms

The optical transition can be considered as two-level system (TLS), which has the ground state $|0\rangle$ with the energy E_0 and the excited state $|1\rangle$ with the energy E_1. The energy gap between them corresponds to the energy of the emitted light $\hbar\Omega_0 = E_1 - E_0$. In such an approach the wavefunction of the TLS is a linear combination of the ground and excited states:

$$|\Psi(t)\rangle = a(t)\,|0\rangle + b(t)\,|1\rangle\,. \tag{2.8}$$

Here $a(t)$ and $b(t)$ represent the probability amplitude of the state. Thus a probability to find the system in the state $|0\rangle$ is $|a|^2$, and in the state $|1\rangle$ is $|b|^2$. $|a|^2$ and $|b|^2$ can be also called *population* of the corresponding state.

Elimination of the time-dependent oscillating component $\exp(-i\Omega_0 t)$ simplifies the consideration. The approach is called *rotating wave approximation* (RWA), so the time dependence remains only in the amplitudes $a(t)$ and $\mathrm{b}(t)$, which comprehensively describe the quantum state. Their squared modules define the population of the levels. The complex phase between $a(t)$ and $\mathrm{b}(t)$ usually called *quantum phase* φ or *coherence*, it can be associated with the phase of the oscillating dipole responsible for the optical transition.

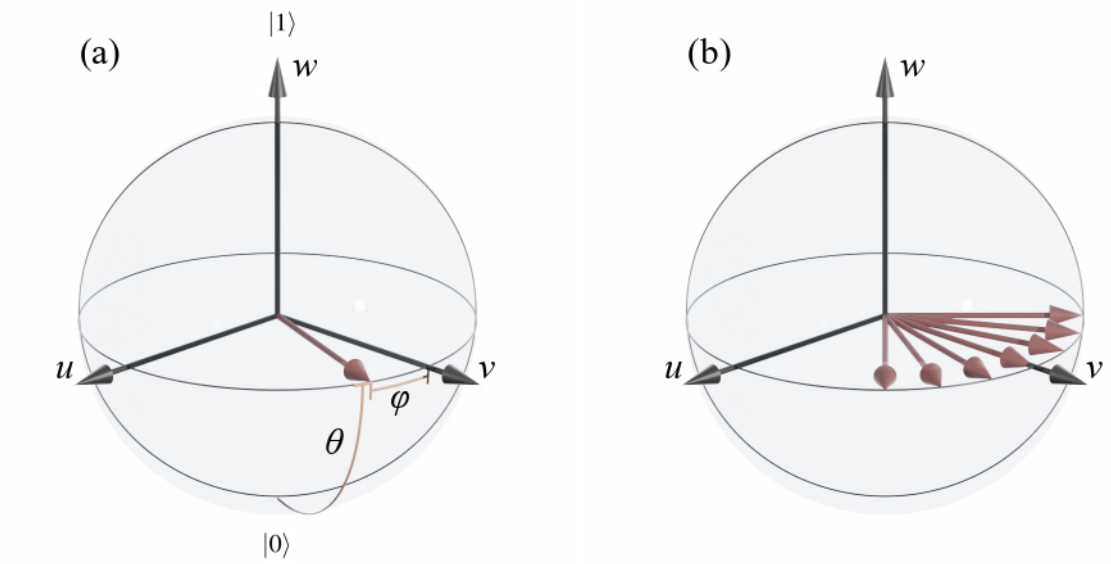

Figure 2.8: *(a) The Bloch vector on the Bloch sphere, definition of the θ and φ; (b) ensemble of the Bloch vectors*

The most illustrative representation of the TLS's population and phase is an association of the state to a vector on the Bloch sphere, which is shown in Fig. 2.8(a) and usually called *Bloch vector*. The vector represents the state of the TLS and is defined by θ and ϕ, while its length is constant due to $\langle\Psi|\Psi\rangle = 1$. In the (u, v, w) coordinates its position is set as $(\sin\theta\sin\varphi, \sin\theta\cos\varphi, -cos\theta)$, where coaltitude θ corresponds to the population, and the longitude ϕ to the quantum phase. When $\theta = 0$ the TLS is in the state $|0\rangle$, when $\theta = \pi$ TLS is in the state $|1\rangle$. The representation of the TLS state as a vector on the Bloch sphere is equivalent to the density matrix formalism, their interconnection is shown in Eq. 2.9.

$$\rho = \begin{bmatrix} |a(t)|^2 & a(t)b^*(t) \\ a^*(t)b(t) & |b(t)|^2 \end{bmatrix} = \begin{bmatrix} (1+w)/2 & v+iu \\ v-iu & (1-w)/2 \end{bmatrix} = \begin{bmatrix} \cos\theta/2 & e^{i\phi} \\ e^{-i\phi} & \sin\theta/2 \end{bmatrix} \tag{2.9}$$

The diagonal elements of the density matrix ρ correspond to the population, on the Bloch sphere it is represented by the w-axis. The off-diagonal elements of the density matrix correspond to the coherence between states, its equivalent on the Bloch sphere is ϕ i.e. an angle between the vector and v-axis in the uv-plane. The density matrix formalism is more general since it can easily support the description of an arbitrary multi-level system, while the Bloch sphere is more suitable for TLS being more illustrative. The Bloch sphere is advantageous for the visualization of the ensemble's behaviour as shown in Fig. 2.8(b).

Phases of the quantum emitters can be associated with the phases of the corresponding dipoles. When the vectors are samely directed the dipoles are in phase and create the macroscopic polarization. We will first illustratively describe the evolution of the quantum state on the Bloch sphere and afterwards summarize it by the density matrix formalism.

2.2.2 Dynamics of the state of two-level system

Interaction of the TLS with the light

The field of the electromagnetic wave rotates the Bloch vector of the TLS around the $(\Omega_R, 0, 0)$, supposing the frequency of the wave fulfilling the resonance conditions of the TLS. Here Ω_R is the Rabi frequency, which is defined as $\Omega_R \propto \mathbf{dE}$, where $\mathbf{d}$ - dipole of the optical transition, $\mathbf{E}$ is an electric field of the electromagnetic wave. The action of the pulse of a certain duration leads to a rotation by a certain angle θ so-called *area of the pulse*. The pulses can be called accordingly to their areas, for instance, $\pi/2$-pulse or 2π-pulse. The certain value of the θ-increment depends on the envelop function of

the electromagnetic wave as follows:

$$\theta = \frac{2}{\hbar} \int |\mathbf{d}\mathbf{E}(t)| dt, \tag{2.10}$$

If the pulse is detuned from the resonancce by Δ, so $E_1 - E_0 = \hbar\Omega_0 + \Delta$, the vector rotates around $(\Omega_\mathrm{R}, 0, \Delta)$ with the *generalized Rabi frequency* $\tilde{\Omega} = \sqrt{\Omega_R^2 + \Delta^2}$.

A noticeable case of TLS driving by light is the *Rabi oscillations* (or sometimes Rabi flops). The vector on the Bloch sphere under the resonant electromagnetic field rotates around $(\Omega_\mathrm{R}, 0, 0)$. Supposing the initial state $(0, 0, -1)$ the population of the excited state oscillates as $\sin(\theta/2)$, which is the key point of the Rabi oscillations. They can be observed by various techniques such as photoluminescence [Hto+02] or photon echo [Pol+16]

Free evolution

The ensembles of TLS which exhibit different transition frequencies when the dispersion among ensemble exceeds an individual linewidth is called *inhomogeneously broadened*. We assign the detuning from the mean frequency Ω of the ensemble as Δ_i. During the free evolution, the detuned TLSs continuously increase their phase on the Bloch sphere as $\varphi_\mathrm{i} = \Delta_\mathrm{i} t$, on the Bloch sphere it corresponds to rotation around the $(0, 0, \Delta_\mathrm{i})$. Such evolution plays a role in the inhomogeneously broadened ensembles of TLS, it results in the redistribution of the vectors among the uv plane even if they are initially set in the same state, what we call *dephasing*. Thus, in the inhomogeneously broadened ensembles, the macroscopic polarization always disappears because of dephasing.

Relaxation

Since the Bloch sphere was first used to describe behaviour of the magnetic momentum in the magnetic field, the terms remain. The relaxation can be characterized by longitudinal relaxation time T_2 responsible for the phase relaxation and transverse relaxation time T_1 responsible for the population relaxation. Since the population relaxation is a spontaneous process, it also contributes to the phase relaxation as:

$$\frac{1}{T_2} = \frac{1}{2T_1} + \frac{1}{\tau_\mathrm{p}} \tag{2.11}$$

where the τ_p is a pure dephasing due to scattering, manifested in the phase jumps. The factor of 2 at the T_1 originates from the conversion of the polarization (as an electric field) to the population (as intensity) since $I \propto |\mathbf{E}|^2$.

Inhomogeneous ensemble

The phase ϕ of the TLS can be associated with the phase of the dipole of the transi-

tion, such a point of view is beneficial for consideration of the effects in an ensemble of TLS. On the Bloch sphere ensemble of TLS can be represented by a set of Bloch vectors as it is shown in Fig. 2.8(b), and each of them shows a behaviour of the individual TLS. When the Bloch vectors (and the dipoles) are samely directed i.e. have the same phase, the macroscopic polarization occurs. We associate it with coherent light emission.

If the inhomogeneously broadened ensemble has a macroscopic polarization at some moment, dispersion of the resonant frequencies of the individual TLS and subsequent phase evolution $\varphi_\mathrm{i} = \Delta_\mathrm{i} t$ leads to loose of the macroscopic polarization. Its decay time $T^* \propto 1/\Delta$, where Δ is a dispersion of the ensemble.

Temporal evolution

Summarizing the written above, the dynamics of the vectors on the Bloch sphere consists of two parts: (i) rotation around the vector $(\Omega_R, 0, \Delta_\mathrm{i})$, which in absence of light is reduced to $(0, 0, \Delta_\mathrm{i})$, and (ii) damping of the vector, which consists of the population relaxation and the coherence loss. The most comprehensive description of the vector dynamics on the Bloch sphere may be done by the optical Bloch equation solution:

$$\frac{d}{dt}\begin{pmatrix} u \\ v \\ w \end{pmatrix} = \begin{pmatrix} u \\ v \\ w \end{pmatrix} \times \begin{pmatrix} \Omega_R(t) \\ 0 \\ \Delta \end{pmatrix} - \begin{pmatrix} u/T_2 \\ v/T_2 \\ w/T_1 \end{pmatrix}, \tag{2.12}$$

The current equation matches Eq. 2.7. The same result can be reached using the Lindblad equation, governing the density matrix evolution we consider below.

2.2.3 Density matrix formalism

The n-level system's density matrix has a size of $n \times n$. The diagonal elements correspond to the population, while the off-diagonal represents the coherence between the states. The temporal evolution of the density matrix is defined by the Lindblad equation:

$$\frac{d}{dt}\rho = \frac{i}{\hbar}\left[\hat{H}, \rho\right] + \Gamma(\rho), \tag{2.13}$$

where $\hat{H}$ - is a Hamiltonian of the system, Γ - relaxation time matrix.

The Hamiltonian defines the configuration of the system. It can be decomposed in a sum of different components as the unperturbed system Hamiltonian $\hat{H}_0$, magnetic field related $\hat{H}_\mathrm{B}$ and interaction with the light $\hat{V}$, which supposed to be time-dependent $\hat{\mathrm{V}} = \hat{\mathrm{V}}(t)$ in order to represent the optical pulses. Thus, the Hamiltonian of the system we study must be expressed as:

$$\hat{\mathrm{H}} = \hat{\mathrm{H}}_0 + \hat{\mathrm{H}}_\mathrm{B} + \hat{\mathrm{V}}, \tag{2.14}$$

Their representation in the basis $|S=-1/2\rangle$, $|S=1/2\rangle$, $|J=-3/2\rangle$, and $|J=3/2\rangle$ for the D^0X and X^- having the four-level is the following:

$$\hat{\mathrm{H}}_0 = \begin{bmatrix} 0 & 0 & 0 & 0 \\ 0 & 0 & 0 & 0 \\ 0 & 0 & \hbar\Omega & 0 \\ 0 & 0 & 0 & \hbar\Omega \end{bmatrix}, \quad \mathrm{H_B} = \frac{\hbar}{2} \begin{bmatrix} 0 & \omega_\mathrm{e} & 0 & 0 \\ \omega_\mathrm{e} & 0 & 0 & 0 \\ 0 & 0 & 0 & \omega_\mathrm{hh} \\ 0 & 0 & \omega_\mathrm{hh} & 0 \end{bmatrix} \tag{2.15}$$

Here the $\hbar\Omega_0$ corresponds to the energy of the optical transition. The off-diagonal elements of the $\mathrm{H_B}$ consist of the four elements, which correspond to the Larmor precession of the electrons and heavy holes between the states spin up and down with the $\omega_\mathrm{e} = g_\mathrm{e}\mu_\mathrm{B}B/\hbar$ and $\omega_\mathrm{hh} = g_\mathrm{hh}\mu_\mathrm{B}B/\hbar$. The magnetic field is applied perpendicular to the light propagation direction. The $\hat{\mathrm{V}}$ term is responsible for the interaction with the light:

$$\hat{\mathrm{V}}(\mathrm{t}) = \begin{bmatrix} 0 & 0 & f_+^*(t)e^{i\Omega_0 t} & 0 \\ 0 & 0 & 0 & f_-^*(t)e^{i\Omega_0 t} \\ f_+(t)e^{-i\Omega_0 t} & 0 & 0 & 0 \\ 0 & f_-(t)e^{-i\Omega_0 t} & 0 & 0 \end{bmatrix}, \tag{2.16}$$

where the $f_\pm(t)$ are defined as:

$$f_\pm(t) = -\frac{2e^{i\omega t}}{\hbar} \int d_\pm(r) E_{\sigma^\pm}(r,t) d^3r, \tag{2.17}$$

The dipole originates from the quantum transition matrix element we define as $d_\pm(r) = \langle 1/2|\, \hat{d}_+(r)\, |3/2\rangle = \langle -1/2|\, \hat{d}_-(r)\, |-3/2\rangle$, and the $E_{\sigma^\pm}(r,t)$ is a circular component of the electric field, so $E_{\sigma^\pm} = (E_x \pm iE_y)/\sqrt{2}$.

The relaxation component of the Lindblad equation is Γ. Not all processes should be accounted for each particular task. The most comprehensive representation of the Γ includes the optical coherence and population decays, and spin coherence and population decay represented by the following matrix:

$$\begin{bmatrix} -\frac{\rho_{11}-\rho_{22}}{2T_{2,\mathrm{e}}} + \frac{\rho_{33}}{\tau_r} & -\frac{\rho_{12}+\rho_{21}}{2T_{1,\mathrm{e}}} - \frac{\rho_{12}-\rho_{21}}{2T_{2,\mathrm{e}}} & -\frac{\rho_{13}}{T_2} & -\frac{\rho_{14}}{T_2} \\ -\frac{\rho_{12}+\rho_{21}}{2T_{1,\mathrm{e}}} + \frac{\rho_{12}-\rho_{21}}{2T_{2,\mathrm{e}}} & -\frac{\rho_{22}-\rho_{11}}{2T_{2,\mathrm{e}}} + \frac{\rho_{44}}{\tau_r} & -\frac{\rho_{23}}{T_2} & -\frac{\rho_{24}}{T_2} \\ -\frac{\rho_{31}}{T_2} & -\frac{\rho_{32}}{T_2} & -\frac{\rho_{33}-\rho_{44}}{2T_{2,\mathrm{h}}} - \frac{\rho_{33}}{\tau_r} & -\frac{\rho_{34}+\rho_{43}}{2T_{1,\mathrm{h}}} - \frac{\rho_{34}-\rho_{43}}{2T_{2,\mathrm{h}}} - \frac{\rho_{34}}{\tau_r} \\ -\frac{\rho_{41}}{T_2} & -\frac{\rho_{42}}{T_2} & -\frac{\rho_{34}+\rho_{43}}{2T_{1,\mathrm{h}}} + \frac{\rho_{34}-\rho_{43}}{2T_{2,\mathrm{h}}} - \frac{\rho_{43}}{\tau_r} & -\frac{\rho_{44}-\rho_{33}}{2T_{2,\mathrm{h}}} - \frac{\rho_{44}}{\tau_r} \end{bmatrix}. \tag{2.18}$$

Here the elements Γ_{13}, Γ_{14}, Γ_{23}, Γ_{43} and conjugated represent the decoherence of the optical transitions, the elements represent Γ_{21}, Γ_{43} and conjugated correspond to the spin decoherence. The diagonal elements are responsible for the population relaxation

as well as for the spin decoherence between the electron states and trion states.

2.3 Ultrafast optical techniques

The mode-locked lasers are known since 1965 and open the possibility to obtain pulses with duration down to picosecond [MC65], while the previous technology – the quality factor modulation had a limit of nanoseconds. First, the active media of the mode-locked lasers was based on dyes but afterwards was replaced by the solid crystals as titanium-sapphire. Since the late 70th, such lasers become commercially available creating a base for ultrafast spectroscopy, which has begun establishing at those times [Sha+79; Jof+88; Sha+87]. Nowadays mode-locked lasers became as compact as desktop PC having a solid-state base pumped by semiconductor diode lasers. The availability of pulsed lasers has accelerated ultrafast measurement techniques such as pump-probe, allowing us to resolve optically the ultrafast fast processes in solids with a temporal resolution of about tens of femtoseconds [Spi+16].

2.3.1 Time-resolved pump-probe spectroscopy

The pump-probe is a well-established bunch of experimental techniques, which are nowadays widely used in semiconductor science. The first pulse is *pump*, it drives the system into a non-equilibrium state. Its state can be read out by the second pulse so-called *probe*. Since the pulses are short enough compared to the system's evolution speed, the probe does a snapshot of the system's state at a certain moment. The delay between pump and probe is variable so that one can study in the dynamics the impact introduced by the first pulse and the way the system goes to the equilibrium state. The pump-probe technique might imply various parameters we observe and various perturbations we introduce, which depend on the certain task of the experiment. For instance, one can induce and track the change in transmission [Pri+22], initiate an acoustic wave, and afterwards, track its dynamics [Tho+86; Kob+22]. The pump pulse may create a bunch of perturbations in magnetically ordered systems with a following probe of the magnetization [Kal+15; Pas+18].

If the wavelength of the pump and probe are the same, it is called the *degenerate* pump-probe otherwise *non-degenerate*. In the latter case, one of the pulses is usually emitted by another laser being synchronised to the first one, and modified by a nonlinear crystal (second harmonic generator), or optical parametric amplifier. The non-degenerate pump-probe allows, in particular, to make a perturbation of one optical resonance and observe the response of another one.

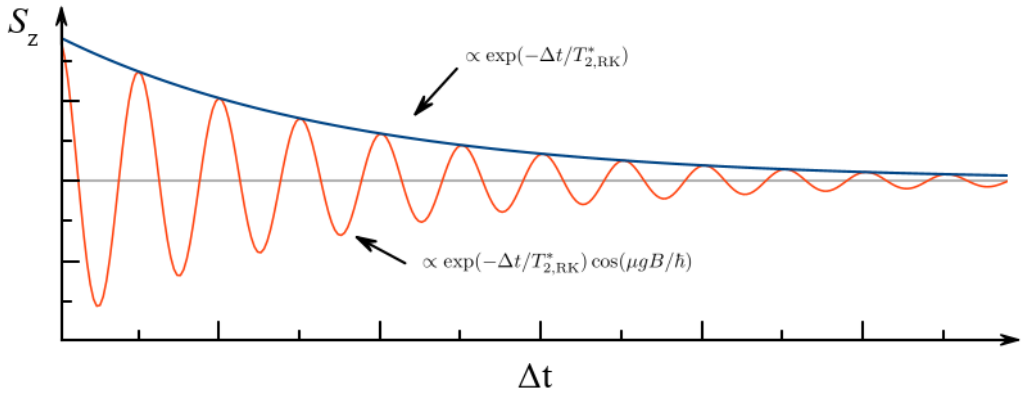

Figure 2.9: *An schamatic example of typically observed temporal evolution of the Kerr rotation signal in tranverse magnetic field (red curve), and without the magnetic field.*

2.3.2 Time-resolved spin dynamics using pump-probe technique

In this work we apply the pump-probe technique to observe dynamic of the magnetization. An absorption of a strong circularly poarlized light pulse (pump) leads to the spin orientation of charge carriers and their complexes. A delayed linearly polarized light of a lower power (probe) arrives at the same spot of the sample. Nonequilibrium spin polarization created by the first pulse makes the media optically active. Polarization plane of the poribe pulse rotates in the transmission geometry, which is called megnetooptical or spin Faraday effect. Rotation of the polarization plane in the reflection geometry is called spin Kerr effect. Moreover, the probe pulse passed through or reflected from such media obtains a circular polarization i.e. becomes elliptically polarized, which is sometimes called *magnetic circular dichroism*. Angle of the polarization plane rotation as well as the ellipticity degree are proportional to the spin polarization of the system. Angle of the polarization plane and the ellipticity degree can be sensed analyzing the orthogonally polarized light components I_H and I_V or I_{σ^+} and I_{σ^-}.

If the magnetic field is directed in the plane perpendicular to the pump and probe pulses **k**-vectors the spins of electrons, holes and their complecess precess in the external magnetic field. Experiment in such configuration is called *Voight geometry*, while the magnetic field is collinear with the pump and probe pulses **k**-vectors configuration os called *Faraday geometry*. In the Voight geometry the spins of the electrons, holes and their complexes precess around the external magnetic field. In this case intensity of the magnetic circular dichroism, Faraday and Kerr rotation as a function of the delay between pump and probe pulses reflects spin precession as shown in Fig. 2.9.

When the circularly polarized pump pulse hits the sample almost perpendicularly to its plane and creates the magnetization along light's **k**-vector. In absence of the

magnetic field, it remains the samely directed, but its amplitude decays. When the magnetic field is applied, the spins rotate in the magnetic field with Larmor frequency and decay with $T^*_{2,e}$. These two cases are shown in Fig. 2.9 by blue and red lines correspondingly. The spin relaxation time can depend on the magnetic field value according to Eq. 2.4. The temporal evolution of the magnetization S_z can be described as:

$$S_z \propto (I_{\sigma^+} - I_{\sigma^-}) \text{ or } (I_\mathrm{H} - I_\mathrm{V}) \propto \exp(-\Delta t / T^*_{2,e}) \cos(\Delta t \omega_L), \tag{2.19}$$

which represents the spin oscillations with a Larmor frequency $\omega_L = \mu_\mathrm{B} g B/\hbar$ and spin relaxation with $T^*_{2,e}$. Such measurements are valid only when the spin relaxation time is shorter than the laser repetition rate, otherwise, the accumulation effect can contribute.

Certain mechanisms responsible for the macroscopic spin polarization of the resident electron by the circularly polarized light are discussed in Ref. [Gla12], here we briefly summarize the so-called trion mechanism. Initially, spins of the resident electrons in the ensemble are evenly distributed between the $S_z = 1/2$ and $-1/2$ as it is shown in Fig. 2.10(a). The circularly polarized light σ^+ drives one the transition $|+1/2\rangle \rightarrow |+3/2\rangle$, it deplets the $|+1/2\rangle$ while population of $|-1/2\rangle$ remains. That results in polarization of the electron state. The electron and heavy hole polarizations rotate with the different Larmor frequencies Fig. 2.10(b). The trion spin relaxation time is usually shorter than the one of the electrons, so when the heavy hole spin and trion population relaxes, the resident electron spin typically remains as shown in Fig. 2.10(c&d).

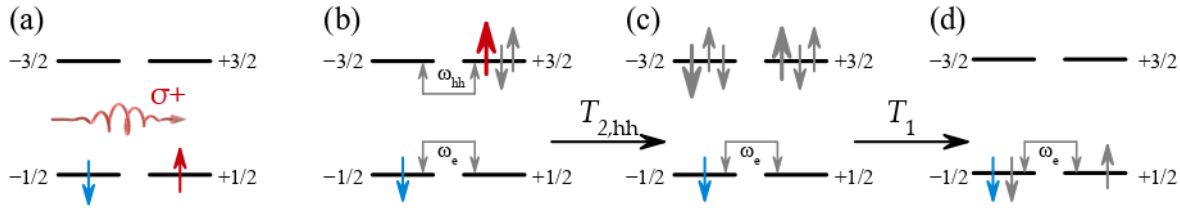

Figure 2.10: *Mechanism of the resident electron spin orientation via the resonant X^- excitation. (a) selective absorption of the σ^+ light; (b) creation of the spin-polarized electrons and X^-s, and their oscillations in the transverse magnetic field; (c) rapid depolarization of the X^- defined by the heavy hole depolarization; (d) the X^- are recombined, while the resident electrons remain their spin polarization*

Resonant spin amplification (RSA) is a variation of the time-resolved Kerr rotation experiment, which is possible when at the moment of the next pump pulse arrival the S_z component introduced by a previous pulse remains [KA98; GI08] i.e. $T_\mathrm{R} \leq T^*_{2,e}$, where T_R is laser repetition time . When the Larmor frequency fulfills $\omega_\mathrm{L} = m/2\pi T_\mathrm{R}$, where m is an integer number and T_R is laser pulse repetition rate, the pulses am-

plify the spin polarization, establishing the resonances. It is schematically shown in Fig. 2.11(a). In the RSA experiment, the probe pulse is set at a small delay before the pump arrival. The resonances are well seen when one sweeps the magnetic field value as shown in Fig. 2.11(b). The sequence of the Lorentzian peaks is defined by the different numbers of rotations the spins did. The interspacing between the peaks depends on the g-factor and the laser repetition rate as $h/|g|\mu_B T_R$, its half width at the half maximum $B_{1/2} = \hbar/|g|\mu_B T^*_{2,e}$ representing the $T^*_{2,e}$ value. The biggest advantage in comparison to dynamics observation is an ability to measure the $T^*_{2,e}$ having an order of T_R and bigger, which cannot be securely extracted from the dynamics.

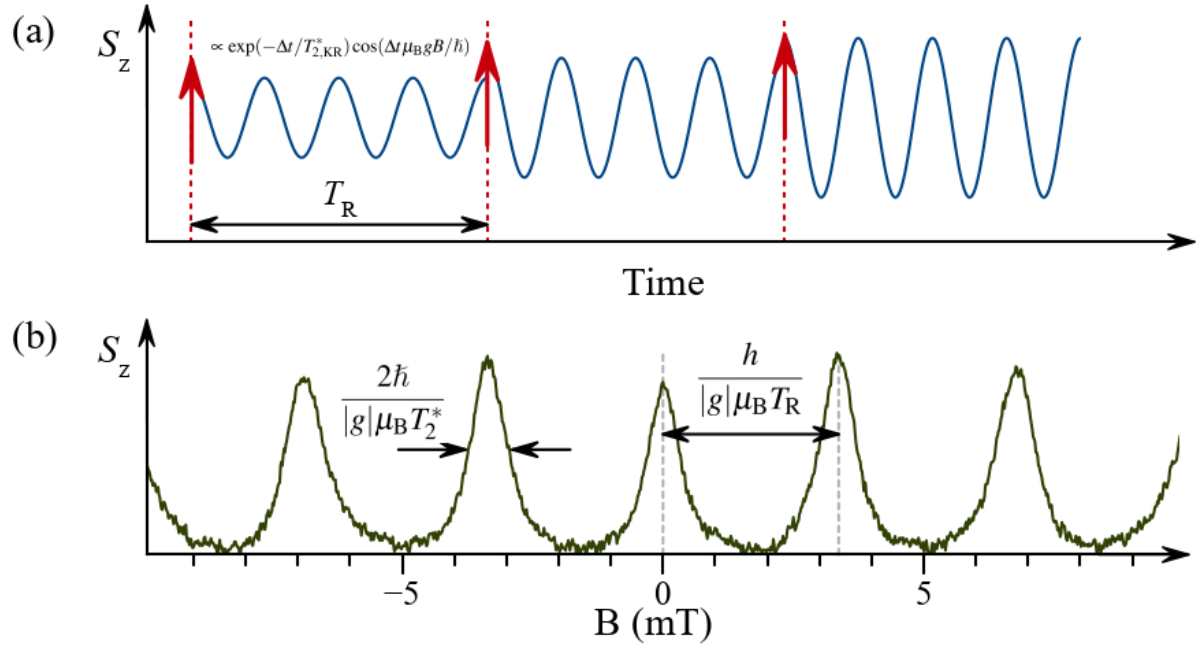

Figure 2.11: *(a) RSA signal formation mechanism. Train of pulses matches the spin precession in phase and therefore resonantly amplifies it. (b) RSA signal example and its dependence on $T^*_{2,e}$ and g-factor. The picture is same to [Zhu+06]*

Despite the approximation of the signal as a set of Lorentzian peaks is well, such a description is not comprehensive. One can clearly see even in Fig. 2.11(b), that the peaks around ± 7 mT are slightly asymmetric at their base. The more detailed model is discussed in work [GI08], where the certain shape of the RSA curve was described by an analytical expression. The introduction of other parameters of the system makes the curve even less looking like a set of the same Lorentzians. For instance, the anisotropy of the spin relaxation times, or the ensemble inhomogeneity can lead to some dependence of the peak height on the magnetic field value. Nevertheless, the approximation by a set of Lorentzian peaks is valid for many cases and allows one simply extract the

spin relaxation time and the g-factor value.

2.3.3 Four-wave mixing

Four-wave mixing (FWM) is a non-linear effect when fields of a few waves create a new one. The polarization induced by a few electromagnetic waves forms a new wave, while their electric fields are related by the high orders of the permittivity χ keeping in mind that the polarization $\mathbf{P}$ is a power series of the incident fields:

$$\mathbf{P} \propto \chi^{(1)}\mathbf{E}_1 + \chi^{(2)}\mathbf{E}_1\mathbf{E}_2 + \chi^{(3)}\mathbf{E}_1\mathbf{E}_2\mathbf{E}_3 + \dots \tag{2.20}$$

The FWM is based on third order permittivity $\chi^{(3)}$, which establishes the relation between the fields as:

$$\mathbf{E}_{\mathrm{FWM}} \propto \chi^{(3)}\mathbf{E}_1\mathbf{E}_2\mathbf{E}_3. \tag{2.21}$$

The $\chi^{(3)}$ can originate from the optical transition of the TLS. Keeping in mind the Eq. 2.21 one can obtain the conditions for the FWM generation setting here the fields of the plane waves:

$$\mathbf{E}(\mathbf{r},t)_i = \mathbf{E}_{\mathrm{i}}(t)e^{i(\mathbf{kr}-\omega_i t)} + c.c., \tag{2.22}$$

which are basically defined by their $\mathbf{k}_{\mathrm{i}}$, ω_{i}. Their phases are omitted here for simplicity, but they obey the same relations as frequency and wavevectors. All the frequencies are supposed be within the optical resonance providing $\chi^{(3)}$.

The Eqs. 2.22 and 2.21 bring us to the relations of the ω, $\mathbf{k}$ between the initial three waves and the new one. We are interested in only two possible field combinations: $\mathbf{E}_1\mathbf{E}_2^*\mathbf{E}_3^*$ and $\mathbf{E}_1^*\mathbf{E}_2\mathbf{E}_3$, which can be used for the photon echo (PE) formation. We consider the only first one since it corresponds to the PE in the transmission geometry. The degenerate FWM takes place when the second field acts also as the third one, so $\mathbf{E}_2 = \mathbf{E}_3$, which sufficiently simplifies the approach. Such degenerate FWM in reflection and transmission geometries as shown in Fig. 2.12. Corresponding relations between the fields of the incident and generated waves are following:

$$\begin{aligned} \mathbf{E}_{\mathrm{FWM}} &\propto \chi^{(3)}\mathbf{E}_1^*\mathbf{E}_2^2 \\ \omega_{\mathrm{FWM}} &= 2\omega_2 - \omega_1 \\ \mathbf{k}_{\mathrm{FWM}} &= 2\mathbf{k}_2 - \mathbf{k}_1 \end{aligned} \tag{2.23}$$

We point out, that when the wavevectors of the two incident waves differ, the FWM propagates in the direction not matching with the initial waves. Since the $\chi^{(3)}$ is small

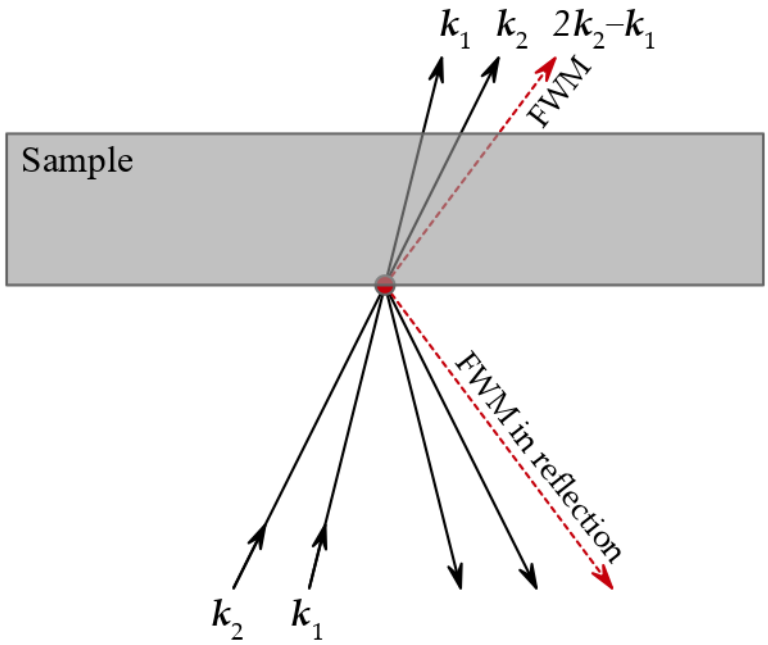

Figure 2.12: *Formation of the four-wave mixing signal by the two pulses in reflection and transmission geometries. The FWM direction fulfills Eq. 2.23*

enough FWM amplitude is usually weak, so spatial separation of the FWM from other beams is essential for its detection as it is demonstrated in Fig. 2.12. One can also slightly differ the frequencies of the waves in order to additionally separate the FWM from the incident fields. The overview of the methods is described in Sec. 3.2.

Coherent spectroscopy

Consideration in terms of the population is essentially non-coherent since it does not involve the quantum phase or coherence between the states. Coherent spectroscopy exploits the light phase sensitive optical phenomena. The macroscopic polarization in such an approach is associated with the coherent light emission, that happens when the TLSs of the ensemble have the same phase.

Coherent spectroscopy was introduced as a method to study optical properties, which cannot be obtained from linear methods such as reflection or absorption spectroscopy. For instance, it gives access to the homogeneous linewidth in inhomogeneously broadened ensembles [Sha99]. The approach is advantageous since the nonlinear effects are well-pronounced near the excitonic resonance.

In order to delimit the homogeneous and inhomogeneous ensembles, we have to introduce the two characteristic values: Δ_{nh} – the dispersion of the resonant frequencies over the ensemble and γ – the homogeneous linewidth, which is limited by the decoherence time of the state T_2.

When the linewidth of the individual TLS is broader than the dispersion among

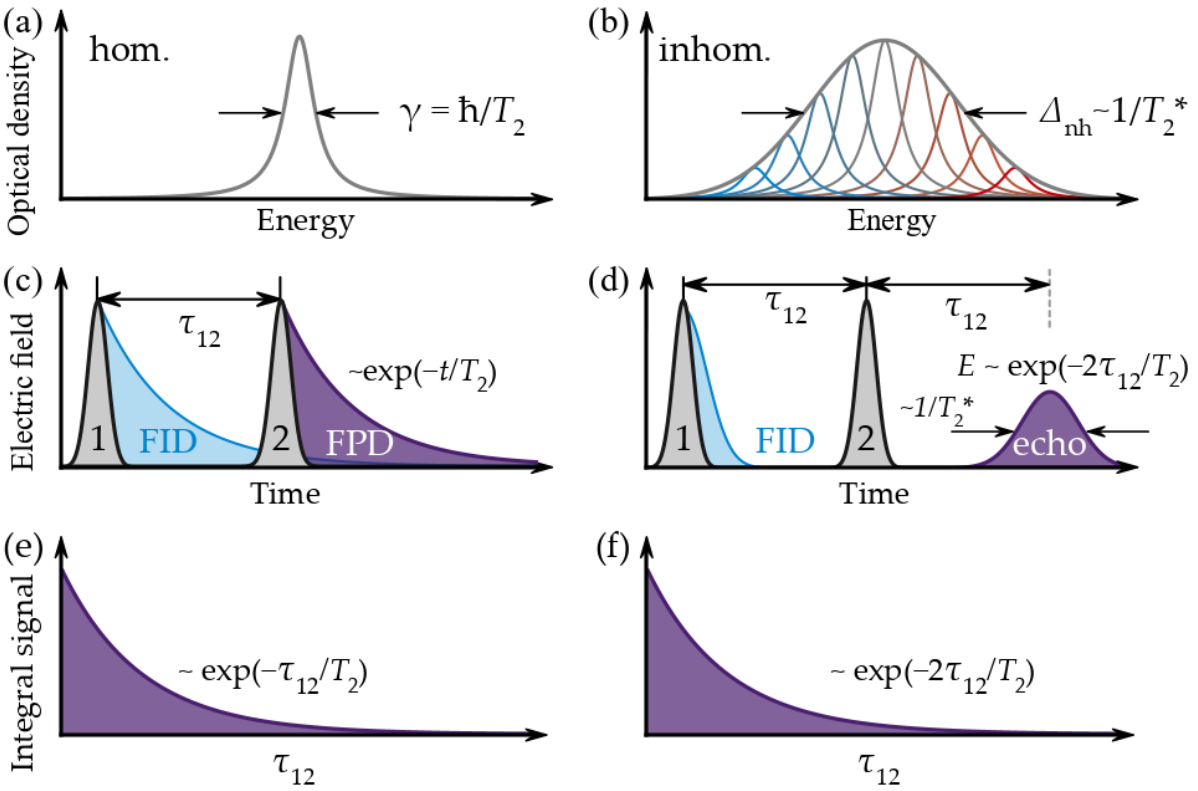

Figure 2.13: *Spectral density of the homogeneous (a) and inhomogeneous (b) ensemble; (c&d) represent their coherent response on the two resonant pulses and formation of free polarization and free induction signals; (e&f) show the dependence of the integral intensity of the FWM signal on the delay between the two pulses* τ_{12}

the ensemble i.e. $\gamma \gg \Delta_{nh}$ the ensemble is broadened *homogeneously*. An instance of the homogeneously broadened ensemble is sketched in Fig. 2.13(a), it has a Lorentzian line shape with the FWHM $\gamma = 2\hbar/T_2$. When the dispersion in resonant frequencies of the TLS in the ensemble is bigger than its homogeneous linewidth i.e. $\gamma \leq \Delta_{nh}$, the ensemble is *inhomogeneously* broadened. It is schematically shown in Fig. 2.13(b), it can have an arbitrary shape, but the inhomogeneity is usually associated with the Gaussian distribution and we consider that very case. The homogeneous linewidth is completely hidden under the broadening.

The short resonant pulse initiates the dipoles corresponding to the optical transition setting them in the same phase and therefore creating macroscopic polarization. In the homogeneous ensemble, the macroscopic polarization remains during the T_2 and leads to the coherent emission of the free induction signal. The effect is called *free induction decay* (FID), and its emission is schematically shown in Fig. 2.13(c). The signal decays exponentially with the time T_2, being the Fourier transform of the optical

spectrum. Since $\gamma \gg \Delta$ the individual TLSs remain in phase unless the microscopic polarization is not completely vanished. If we samely initialize the inhomogeneous ensemble the macroscopic polarization decays with a characteristic time $T_2^* \propto \hbar/\Delta_{\text{nh}}$, and its decay has a Gaussian-like shape. The FID is a linear response of the system, since its linear nature, it does not allow one to access the homogeneous linewidth in the inhomogeneous ensembles.

If the homogeneous ensemble is impacted by the second pulse when the free induction remains it forms the free polarization. The *free-polarization decay* (FPD) is exponentially decaying with the T_2, being a variety of FWM. The FPD is shown in Fig. 2.13(c), its integral value decays exponentially with the delay between the two pulses τ_{12} since its proportional to the remaining free-induction of the first pulse at the moment of the second pulse arriving. Actually, one can perform the same with the inhomogeneous ensembles, but a typically $T_2 \gg T_2^*$, so free induction vanishes right after the first pulse. Thus, such an experiment does not give sufficient advantage in comparison to the echo technique will be overviewed below.

Even though the macroscopic polarization in the inhomogeneous ensembles vanishes rapidly with a typical time T_2^* due to dephasing, each particular TLS keeps its phase sufficiently longer during T_2. The action of the second pulse reverses the phase evolution of all the TLS in the ensemble and initiates the rephasing. We assign the delay between two pulses as τ_{12}. At the τ_{12} after the second pulse action the *echo* appears, which is shown in Fig 2.13(d). It has a Gaussian shape, with width representing the system inhomogeneity Δ_{nh}. Its amplitude as well as integral area decays as $E_{\text{FWM}} \propto exp(-2\tau_{12}/T_2)$ since the TLS decoherence during that time. That very dependence allows one to access the homogeneous linewidth ($\gamma = 2\hbar/T_2$) of the inhomogeneously broadened ensemble. The PE itself is the main experimental technique of the current work, so we will consider the phenomena more comprehensively.

2.3.4 Two-pulse photon echo (2PE)

The echo phenomena in the inhomogeneously broadened ensembles were first observed in the ensemble of spins in 1950 by Erwin Hahn [Hah50]. The spins in the magnetic field were controlled by the radio frequency pulses. The photon echo was first seen in 1964 in the research group of Hartman [Kur+64]. They used the optical transition in ruby crystal, which was excited by the Q-switched pulse laser.

The 2PE may be formed in the inhomogeneously broadened ensemble of TLS. All the TLS are supposed to be initially in the ground state, and all the corresponding Bloch vectors are directed downwards, their $\theta = 0$, and therefore angle in uv-plane is not defined. Application of the $\pi/2$-pulse initializes the system, the vectors on the

Bloch sphere rotate as a whole around the axis $(\Omega_R, 0, \Delta_\text{i})$, which is close to u-axis (see 2.14(a)), supposing ($\Omega_R \gg \Delta_\text{nh}$). Here Δ_i is a detuning of the individual vector, and Δ_nh is a dispersion of the whole ensemble. As a result, the system has a state when all the vectors are directed along the v-axis. During the subsequent free evolution, the vectors rotate around their individual $(\Omega_R, 0, \Delta_\text{i})$ as it is shown in Fig. 2.14(b) distributing within uv-plane and loos the macroscopic polarization. Each oscillator gains a phase $\varphi_\text{i} = \Delta_\text{i} t$ proportionally to its detuning Δ_i. The corresponding phase evolution is shown in Fig. 2.14(e), in the interval from 0 to τ_{12}. It is called *dephasing*.

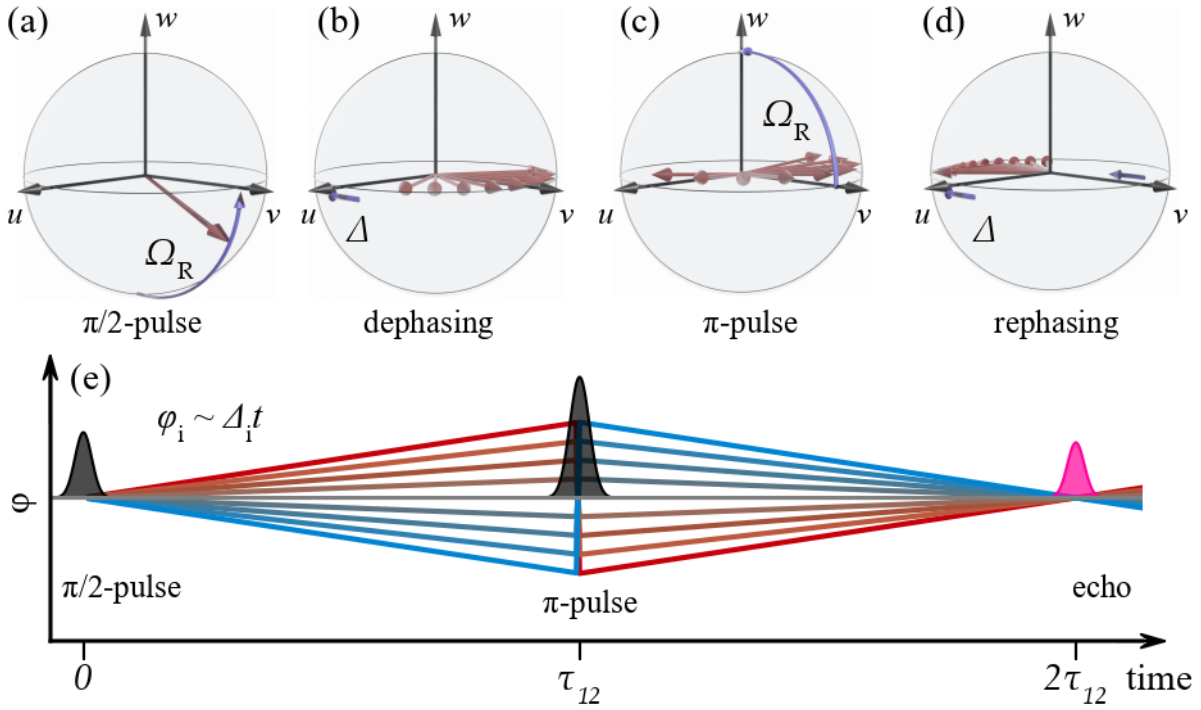

Figure 2.14: *Two-pulse photon echo formation process on the Bloch sphere and corresponding phase behaviour: (a) Initialization of the ensemble by the $\pi/2$-pulse, (b) dephasing of the ensemble; (c) inversion of the phases by the π-pulse; (d) rephasing of and the echo formation; (e) phase behaviour of TLSs in the ensemble.*

The second pulse with an area π reverses the phases and initiates the 2PE formation. The Bloch vectors do a half turn around the vector $(\Omega_R, 0, \Delta_\text{i})$, and eventually return to the uv-plane with the inverted phases as shown in Fig. 2.14(c& d). It is seen in Fig 2.14(e), that the phase inversion reverses the system evolution in the temporal interval from τ_{12} to $2\tau_{12}$. The process ongoing after the second pulse is called *rephasing* and shown in Fig. 2.14(d). Since the system has spent the τ_{12} for dephasing it requires exactly the same time to rephase back. Thus, $2\tau_{12}$ after the first pulse action the vectors gather and recover the macroscopic polarization, which results in the 2PE formation.

The amplitude of the 2PE depends on the areas of the pulses as $E_{2PE} \propto \sin\theta_1 \sin^2\theta_2/2$. The dependence on polarization of the pulses will be discussed below. During the time interval $2\tau_{12}$ some of the oscillators lose their phase and therefore can not contribute to the 2PE anymore, which defines the dependence $E_{2PE}(\tau_{12}) \propto \exp(-2\tau_{12}/T_2)$.

2PE is a powerful tool for the coherent study energy structure and coherent dynamics of exciton complexes in semiconductors. For instance, variation of the pulse polarization allows one to excite selectively the 2PE from the spectrally overlapped subensembles [Pol+19]. The Rabi oscillations allow us to estimate the transition dipole moment [Pol+17]. 2PE behaviour in the magnetic field allows one to see the electron and hole rotations in the magnetic field, particularly estimate g-factor anisotropic shape [Pol+20b; Tri+21]. The corresponding methods will be overviewed below.

2.3.5 Three-pulse photon echo (3PE)

The 3PE is actually the non-degenerate version of the 2PE, where the second and the third fields are represented by the different pulses, so $\mathbf{E}_2 \neq \mathbf{E}_3$. We will consider the case, where they are separated in time, but wavevectors and frequencies remain. The 3PE formation noticeably differs from the 2PE, it involves an intermediate state – population. It gives an opportunity to measure the population dynamics by a coherent technique, which can noticeably differ from dynamics seen by such non-coherent techniques as photoluminescence [Sal+17a].

To be illustrative we show the 3PE formation on the Bloch vector dynamics, which is shown in Fig. 2.15. Initially, all the vectors are supposed to be directed downwards ($\theta = 0$, φ is not defined). The first pulse optimally has an area of $\pi/2$, it rotates the vectors along $(\Omega_R, 0, \Delta_i)$, where each the vector has its individual Δ_i. Supposing $\Delta \ll \Omega_R$, the vectors afterwards are placed along the v-axis. During the following free evolutions, the vectors became distributed within uv plane due to rotation around $(0, 0, \Delta_i)$ that takes place during τ_{12} until the second pulse arrival.

The second pulse optimally has an area $\pi/2$. In contrast to 2PE, it does not invert phases but transfers projection on the v-axis to a projection on the w-axis i.e. population. During the following evolution, the uv-components will rapidly dephase with the T_2^*, but the w-component of the vector decays with T_1. The third pulse optimally has an area of $\pi/2$ and turns the vectors back into uv-plane. The projections on the w-axis are now again transferred to $-v$, so the phase is inverted and therefore it starts rephasing. The echo occurs τ_{12} after the third pulse action. The 3PE formation on the Bloch sphere can be considered as the 2PE with the split π-pulse into two $\pi/2$ separated by τ_{23}.

The biggest advantage of the 3PE is an access to the both T_1 either T_2, since field of 3PE $E_{3PE}(\tau_{23}) \propto exp(-\tau_{23}/T_1)exp(-2\tau_{12}/T_2)$. The T_1 measured by the 3PE can differ

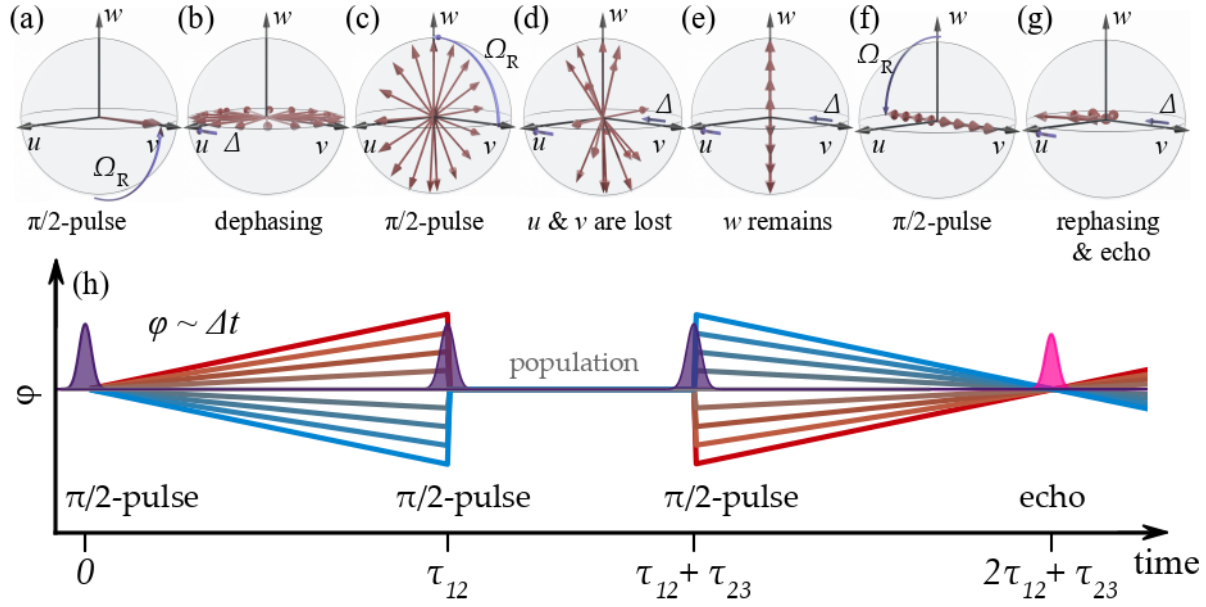

Figure 2.15: *The three-pulse photon echo formation process described on the Bloch spheres (a-g) and the phase diagram (h). (a) initialization of the ensemble by $\pi/2$-pulse; (b) dephasing of the ensemble; (c) transfer of the coherence to the population by $\pi/2$-pulse; (d) washing out the uv components of the vectors; (e) in a while the only w component remains; (f) transfer the phases stored into w component back into the population by $\pi/2$-pulse; (g) rephasing and the echo formation; (h) phase diagram corresponding to the 3PE formation*

since the times observed by, for example, time-resolved photoluminescence.

Thus, we have considered the 2PE and 3PE formation mechanisms. The effects are variations of the four-wave mixing. They allow one directly measure T_2 and T_1 of the TLS. In the following section, we will overview the more advanced techniques, based on the 2PE and 3PE allowing one to investigate such properties of the TLS as level structure, dipole moment, g-factor value, and anisotropy, resident electron $T_{2,e}$ and $T_{1,e}$.

2D Fourier spectroscopy

Measurement of the $E_{3PE}(\tau_{12}, \tau_{23})$ dependence allows us to step towards a more complex technique known as two-dimensional Fourier spectroscopy. The technique for simplicity can be considered as a variation of 3PE, it usually implies the spectrally broad pulses covering one or a few spectral features and the phase control of all the pulses [Bri+09; CM13].

One does a 2D Fourier transform, which gives us the 2D plot representing the resonances that were impacted by the laser pulse, their T_2, T_2^*, and cross-talk between the resonances. Interpretation of such dependencies can be found in the work [Sie+10]. The design of the setup deserves special attention and can be found in the work [Bri+09].

2.4 Photon echo-based techniques

2.4.1 Photon echo polarimetry

Up to now, we did not take into account the polarization of the light implying the fulfilment of the selection rules. That is fair for the TLS, but the level structure of X^0, D^0X and X^- make the 2PE sensitive to the pulse polarizations. The FWM allows one to get a coherent response from the certain excitation using a specific *polarization protocol*, which we assign by a set of letters as HVH or HVVH (in some works HV→H). Here the last letter corresponds to the detecting polarization, while the first letters correspond to the polarization of the applied pulses forming PE. Here H – horizontal polarization, V – vertical, D – diagonal, A – anti-diagonal (perpendicular to the D), $\sigma^{\pm}$ – circular with the different chirality.

Usage of the certain polarization protocols allows one to see the PE from a certain subensemble when they are spectrally overlapped. In the work [Pol+19] was shown, that using the HHH protocol one can see the 2PE from any system we can interact with. HVH protocol gives us the signal only from the four-level system (in our case it can be D^0X or X^-), HDH and HAH give the double reduced signal from the only three-level system (in our case it is X^0). The system can be characterized by its polarization

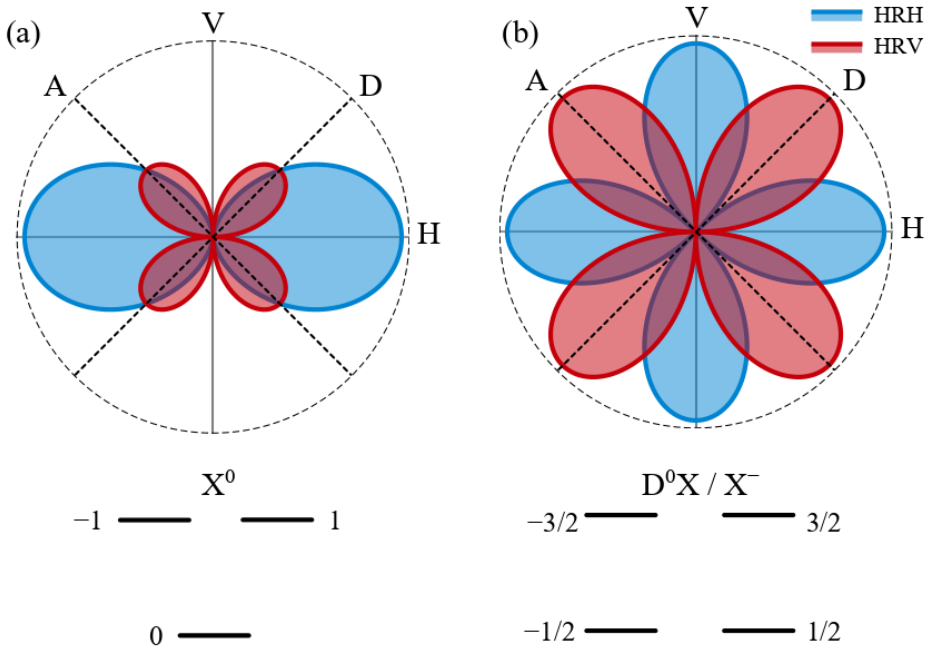

Figure 2.16: *Polarizational dependence of the 2PE in the HRH and HRV polarization protocols corresponding to (a) the three-level system as X^0 and (b) four-level system as D^0X or X^-*

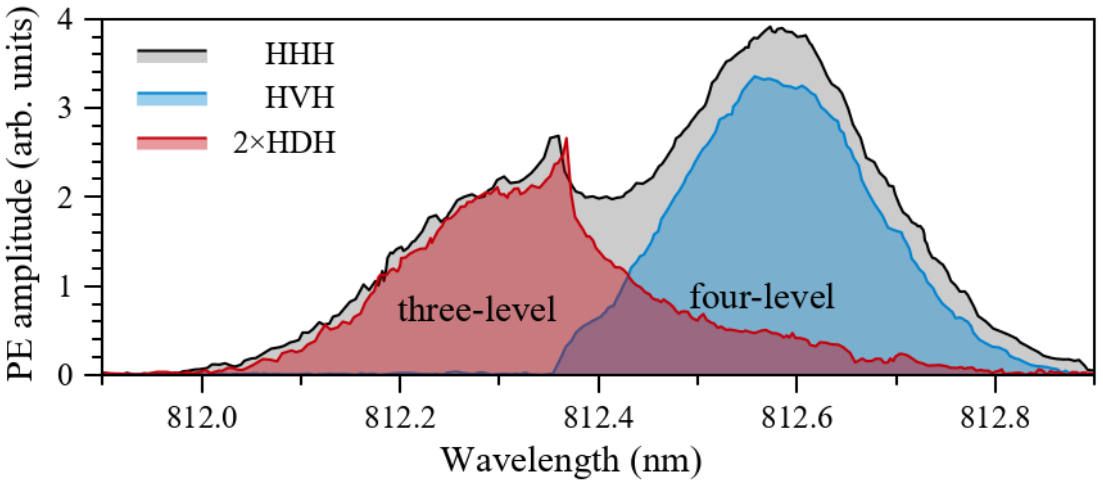

Figure 2.17: *Spectrum of the 2PE from the GaAs QW measured by different polarization protocols: HHH, HVH and HDH at the same $\tau_{12} \ll T_2$, $T = 2$ K.*

dependence when the polarization of the first pulse and the detection are constant, and the polarization of the second pulse rotates (R). The corresponding protocols are called HRH or HRV. Fig. 2.16(a) shows the polarization dependencies of the three-level system. The HRH has two lobes, with the maximum at HHH, and zero at HVH. The HDH and HAH have an amplitude double lower than HHH. The polarization dependencies of the four-level system are shown in Fig. 2.16(b). It has equal maxima at the HVH and HDH, and zero at the HDH and HAH. The HRV dependencies are similar in both cases, but the amplitude in the three-level case is doubly lower.

We consider the dependencies relative to the ϕ_{12} – angle between the first and second pulse linear polarizations. The corresponding analytical expressions are the following:

$$\begin{aligned} &\mathrm{HRH}^{4-\mathrm{level}}(\phi_{12}) \propto \mid \cos 2\phi_{12} \mid, \\ &\mathrm{HRV}^{4-\mathrm{level}}(\phi_{12}) \propto \mid \sin 2\phi_{12} \mid, \\ &\mathrm{HRH}^{3-\mathrm{level}}(\phi_{12}) \propto \cos^2 \phi_{12}, \\ &\mathrm{HRV}^{3-\mathrm{level}}(\phi_{12}) \propto \mid \sin 2\phi_{12} \mid /2, \end{aligned} \tag{2.24}$$

Measurement of the 2PE spectrum in different polarization protocols i.e. scan of the wavelength at the constant τ_{12} and other parameters, allows decomposing the spectrum into contributions of different excitations. An example of such decomposition is given in Fig. 2.17. The HHH signal consists of the two merged bell curves, so we can not attribute any of them to the three and four-level system and found a border-

line between them. Nevertheless, usage of the HVH and HDH polarization protocols allows one to decompose the spectrum to the three and four-level subsystem contributions. Thus, polarization protocols of 2PE give selective access to spectrally overlapped resonances. The effect is quite general and may be seen in a whole bunch of FWM techniques. The polarization selectivity is secured by the Hamiltonian structure.

Thus, such an approach allows one to identify the type of excitonic complex in the semiconductor nanostructure. It is helpful in ensembles of quantum dots where the spectral separation of the different excitonic complexes is restricted. It allows one not only to identify but observe a coherent response from a dedicated excitonic complex. We utilized the technique in the ensemble of QDs to address only charged QDs [[Kos+20]].

2.4.2 Coherent control of the two-level system

An important step towards quantum information processing is the ability to control the state of the TLS, which can be used as *qbit*. The full control of an electron spin in a QD was shown by [Kop+06; Tok+06] using the resonant radio pulses. A drawback of such an approach is a relatively low operating frequency since the manipulation takes place on the timescale of many periods of spin precession. However, the control of the spin states by the optical pulses allows performing a manipulation on the picosecond or even femtosecond timescale, i.e. faster than the spin precession period [Gup+01; Gre+06a; Car+06].

The control of the TLS state can be performed by resonant or slightly detuned pulses, as it was shown in the previous chapter [Pre+08; DG+13] in accord with the Sec. 2.2. The two most prominent effects that can be established using coherent control are the Rabi oscillations and Ramsey fringes. The Rabi oscillations are actually oscillations of the TLS between the ground and excited states under the action of the light, i.e. rotation of the Bloch vector around the $(\Omega_R, 0, 0)$. Taking into account, that the pulse area is an integral of the **Ed** over time, it is possible to see the Rabi oscillations depending on the pulse power (field amplitude) or in time. It can be observed via, for instance, the absorption and transmission [Sti+01], luminescence [Kur+07] or photocurrent [Zre+02].

The Ramsey fringes protocol is based on the two $\pi/2$-pulse actions on the detuned TLS. We suppose the Bloch vector is initialized from the ground state (0,0,1) by $\pi/2$-pulse into the state (0,1,0). Afterwards, it rotates around the $(0, 0, \Delta)$. Depending on the certain position of the vector in the Bloch sphere the second pulse action transfers it to the excited state, ground state or does not impact on. For instance $(0, 1, 0) + \pi/2 \rightarrow (0, 0, 1)$, and $(0, -1, 0) + \pi/2 \rightarrow (0, 0, -1)$, but $(\pm 1, 0, 0) + \pi/2 \rightarrow (\pm 1, 0, 0)$

remain. Variation of the delay between the pulses implies a different position of the Bloch vector at the moment of the second pulse arrival, and therefore rotation of the vector on the Bloch sphere results in the oscillations of the population. That periodic dependence establishes the Ramsey fringes.

PE driven Rabi oscillations

The four-wave mixing is an excellent playground for the investigation of coherent phenomena. The QDs secure good exciton localization and reduce exciton-exciton interaction [CS01], which results in long T_2 times. In order to increase the interaction with the light, one typically uses the ensembles of the QDs having a sufficient inhomogeneous broadening. PE is a good way to perform coherent control avoiding the inhomogeneity impact since the PE formation implies consequent dephasing and rephasing of the system.

The amplitude of the 2PE depends on the amplitudes of incident light pulse areas as $E_{2PE} \propto \sin(\theta_1)\sin^2(\theta_2/2)$ in the case of 2PE and $E_{3PE} \propto \sin(\theta_1)\sin(\theta_2)\sin(\theta_3)$ for the 3PE. Here θ_i are defined by Eq. 2.10. In the low fields, we see the linear response in the $\chi^{(3)}$ regime, but the pulse areas comparable with $\pi/2$ or higher bring us into a nonlinear regime, which is represented by the Rabi oscillations.

Despite the fact, that at the first glance, PE is insensitive to inhomogeneity when Δ_{nh} is comparable to the Ω_R, it still can impact echo timing [AE75]. In that case, we can not consider the pulse actions as infinitely short. Here the dephasing takes already place on the timescale of the pulse action. The effect was seen for example in the ruby [Sam+78], the InGaAs QDs [Pol+16] or CdTe QW [Pol+17].

The examples are shown in Fig. 2.18, where the initialization of the system is shown on the Bloch sphere. (a) and (b) correspond to the cases, when $\Delta_{nr}/\Omega_R \ll 1$ and $\Delta_{nr}/\Omega_R \sim 1$. The effect is described in Ref. [Pol+16].

The Rabi oscillations of the single TLS are usually well pronounced, meanwhile, ensembles of them have usually a damping due to the inhomogeneous excitation. A sufficient source of the broadening is an inhomogeneous excitation. The beam of the laser has often a profile close to 2D Gaussian distribution, which leads to a dispersion of the Rabi frequencies within ensemble. At the same time, the TLS in the centre of the laser beam and on its side gets the different areas of the pulse, which makes observed Rabi oscillations less pronounced. The mechanism was considered in the work [Pol+17].

The problem can be overcome by a beam shaper making the flattop beam. Usage of the flattop second pulse makes the Rabi oscillations on the 2PE sufficiently better pronounced, but nevertheless, they do not follow the predicted $\sin(\theta_2)$. It was found, that at the pulse areas, over π the efficient interaction with the acoustic phonons damps

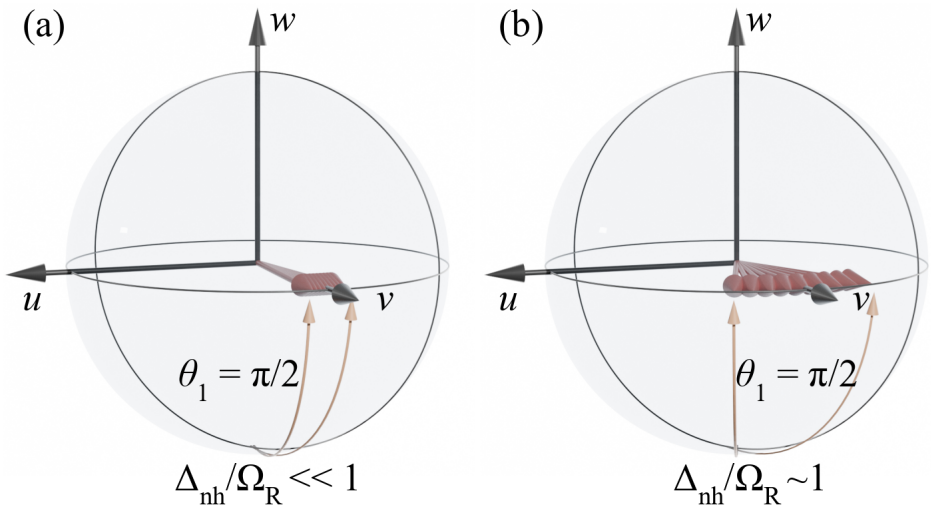

Figure 2.18: *The different dephasing impact during the initialization of the PE by the first $\pi/2$ pulse: (a) $\Omega_R/\Delta_{\mathrm{nh}} \ll 1$ and (b) $\Omega_R/\Delta_{\mathrm{nh}} \sim 1$*

the Rabi oscillations [Gri+22].

2.4.3 Spin-dependent two-pulse photon echo

Sequence of the light pulses with of a certain polarizations allow to acces spin states of the excitonic compleces. A noticeable feature of the D^0X and X^- is the ability to store the optical coherentce into the resident electron spin subsystem, where its lifetime is limited by the spin relaxation times which are sufficiently exceeding the optical ones ($T^*_{2,\mathrm{e}} \gg T_2$), that is discussed in work [Lan+12].

We consider now X^- in the magnetic field in the Voight geometry ($\mathbf{B} \perp \mathbf{k}$), on which we do the projection of the angular momentum i.e. J_{x}. The states are called accordingly, they are shown in Fig. 2.19. The Larmor precession provides a mixing between the electron states $|\pm 1/2\rangle$, or trion states $|\pm 3/2\rangle$. Because of the lower g-factor and shorter spin relaxation time, we neglect the intermixing of the X^- in the following explanations, and it will be considered only in Chapter 6.

As a reference, we consider a case with no mixing when $B = 0$. When we act by a σ^+-polarized pulse on the four-level system, it creates coherence between the states $|+1/2\rangle$ and $|+3/2\rangle$. The following σ^+ starts the rephasing of the system and it results in the σ^+-polarized echo.

When the magnetic field is on at the same conditions, the coherence created by the first σ^+-pulse oscillates between $|+3/2\rangle$ & $|+1/2\rangle$ and $|+3/2\rangle$ & $|-1/2\rangle$ with the Larmor frequency ω_{L} (see Fig. 2.19(a)). Now, if the second σ^+-pulse arrives at $\tau_{12} = 2\pi/\omega_e$, the coherence is between the states $|+3/2\rangle$ & $|+1/2\rangle$ and it repeats the trivial

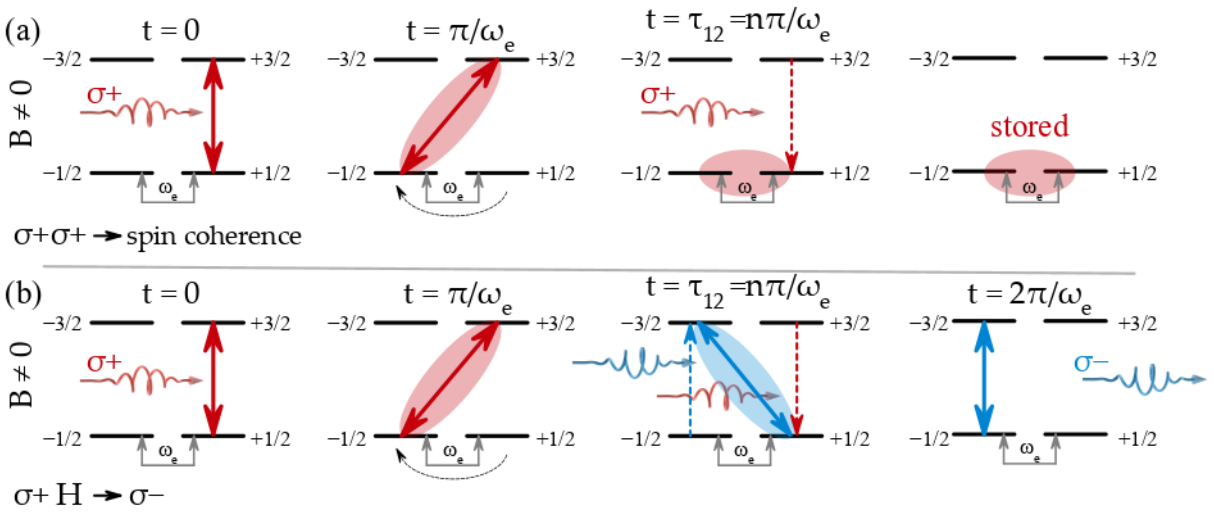

Figure 2.19: *Coherent manipulation optical coherence in the magnetic field: (a) its storage into the resident electron spin states; (b) inversion of the PE polarization in the magnetic field.*

case without the magnetic field. Nevertheless, if the second pulse arrives when $\tau_{12} = n\pi/\omega_e$ the coherence will be transferred to the spin states $|+1/2\rangle$ & $|-1/2\rangle$. Here it can remain for a longer time since $T^*_{2,e} \gg T_2$.

Another interesting scenario can be implemented at this setting when the second pulse is linear, i.e. consists of both σ^+ and σ^-. If it arrives at $\tau_{12} = n\pi/\omega_e$ it simultaneously transfers the coherence from the states $|+3/2\rangle$ & $|-1/2\rangle$ to $|-3/2\rangle$ & $|+1/2\rangle$. It is schematically shown in Fig. 2.19(b), the effect was comprehensively studied in the work [Pol+20a].

The g-factor in the crystal anisotropy can sufficiently impact the 2PE amplitude, modifying $E_{2PE}(\tau_{12}, B)$ [Tri+21; Pol+20b]. Thus, the PE technique gives us access to the anisotropic properties of the electron and heavy hole in-plane g-factor components.

2.4.4 Spin-dependent long-lived three-pulse photon echo

The optical coherence stored in the spin states $|+1/2\rangle$ & $|-1/2\rangle$ by two pulses as shown in 2.19 can be retrieved by the third pulse in the frame of the 3PE protocol. We will illustrate the process by $\sigma^+\sigma^+\sigma^+\sigma^+$ 3PE protocol, here as above ($\mathbf{B} \perp \mathbf{k}$).

The protocol is schematically shown in Fig. 2.20. As before, the first pulse creates an optical coherence between the state $|+3/2\rangle$ & $|+1/2\rangle$. In presence of the magnetic field, it oscillates between the states $|+3/2\rangle$ & $|+1/2\rangle$ and $|+3/2\rangle$ & $|-1/2\rangle$ with the electron Larmor frequency ω_e. If the second pulse arrives at the moment $n\pi/\omega_e$ (where $n \in \mathbb{N}$), the coherence transfers to the $|+1/2\rangle$ & $|-1/2\rangle$, i.e. is stored in the electron's

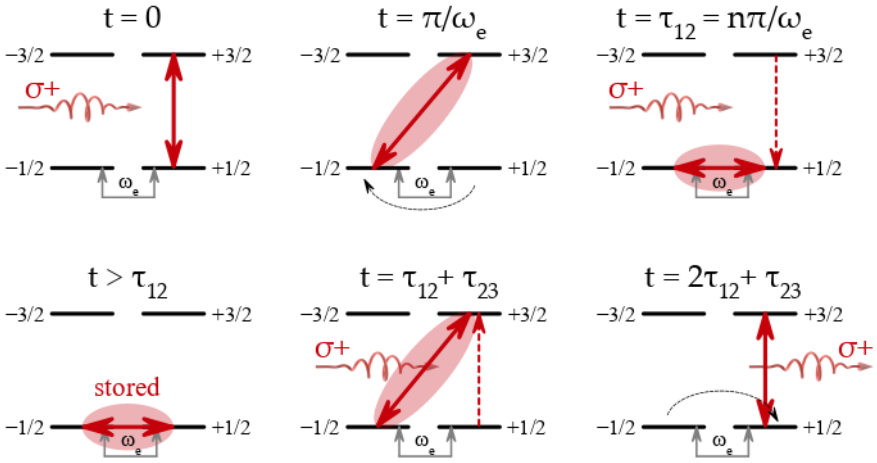

Figure 2.20: *Schematic representation of the processes responsible for the long-lived 3PE, which involves storage of the coherence into the resident electron spin*

spin. The third pulse transfers the coherence back to the states $|+3/2\rangle$ & $|-1/2\rangle$ and starts the rephasing. That results in a PE formation τ_{12} after the third pulse action when the coherence is between the states $|+3/2\rangle$ & $|+1/2\rangle$. The maximal 3PE amplitude is reached when all three pulses have an area of $\pi/2$ as usual 3PE. In such an approach, the range τ_{23} the signal decays with $T^*_{2,e}$, not T_1. We point out the fact, that here coherence is stored in the resident electron spin states. Surely, that can be driven either using $\sigma^-\sigma^-\sigma^-\sigma^-$ protocol apart and simultaneously. We describe only one of them since the second one is completely mirroring the first.

For the bigger efficiency, the protocol should be done using linear polarization of pulses. Taking into account H = $(\sigma^+ + \sigma^-)/\sqrt{2}$ and iV = $(\sigma^+ - \sigma^-)/\sqrt{2}$, the protocol can be done in the linear polarization protocol HVVH. From the formulas, one sees that the cross-polarized sequence impacts on the system similarly to the circular light. The temporal evolution of the signal can be simply described as:

$$E_{\mathrm{HVVH}} \propto cos[\omega_e(\tau_{12}+\tau_{23})]\exp(-\frac{\tau_{23}}{T_{2,e}})\exp(-\frac{2\tau_{12}}{T_2}), \tag{2.25}$$

in accord to the work. [Lan+14]. Here τ_{ij} is a time interval between the i-th and j-th pulse, and $T_{2,e}$ is a transverse spin relaxation time.

The effect can be also considered in terms of spin physics, so the sequence of the cross-polarized pulses creates the grating in the ensemble of spins as:

$$S^0_y - iS^0_z \propto i\exp(i\omega_e\tau_{12}/2)\cos(\Omega_0\tau_{12} + \mathbf{k}_{2,\parallel}\mathbf{r} - \mathbf{k}_{1,\parallel}\mathbf{r}), \tag{2.26}$$

where ω_e is the electron Larmor frequency, Ω_0 is a freqency of the optical transition, and $\mathbf{k}_{i,\|}$ are in-plane components of the wavevectors. The grating gives a coherent response to the third pulse action. The decay of the grating is represented by the decay of the signal. The oscillations of the signal are defined by the rotation of the grating in the magnetic field. The signal is proportional to the projection of the current spin grating on its initial state $(S_y(0) - iS_z(0)) \cdot (S_y(t) - iS_z(t))$.

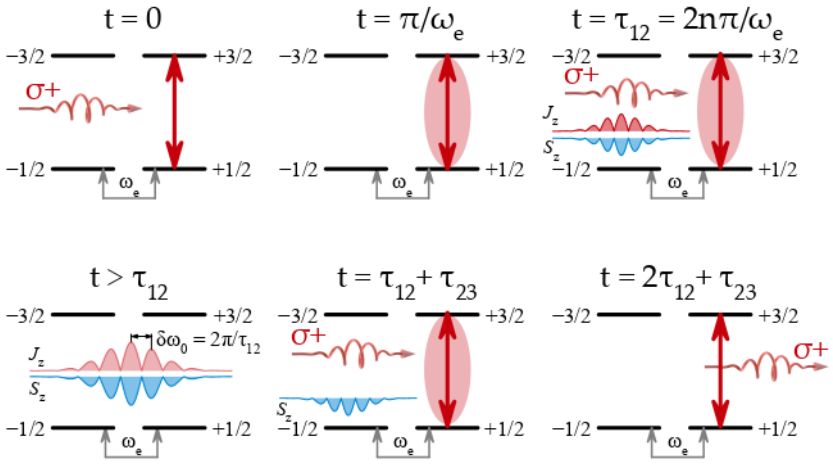

Figure 2.21: *Schematic representation of the processes responsible for the long-lived 3PE with a coherence storage into the spin population fringes*

Another way to involve the spin degrees of freedom is a storage of the coherence to the population fringes of the spin states, which also have a long relaxation time corresponding to the $T_{1,e}$. It may be done using HHHH polarization protocol, which is schematically shown in Fig. 2.21. A couple of co-polarized pulses create a spectral fringe in the population of the spin subsystem. The period is defined as $2\pi/\tau_{12}$. The fringe has the highest contrast when the second pulse arrives after an integer number of the spin rotations i.e. $\tau_{12} = 2n\pi/\omega_e$, where n is an integer number. The resident electron spin grating S_z has a sufficiently larger lifetime than X^- related J_z. As above, the spin grating gives a coherent response after the action of the third pulse. The temporal evolution of the long-lived 3PE in HVVH polarization protocol is defined as:

$$E_{HHHH} \propto sin^2(\frac{\omega_e \tau_{12}}{2}) exp(-\frac{\tau_{23}}{T_{1,e}}) \exp(-\frac{2\tau_{12}}{T_2}), \tag{2.27}$$

where $T_{1,e}$ is a spin transverse spin relaxation time.

Chapter 3

Description of the samples and experimental techniques

3.1 The samples

In the work, we used three samples, which suit best for the respective experiments. Since the work dedicates to the physical phenomena observation and new experimental approaches, we do not use unique samples or growth technologies. The samples were grown by molecular beam epitaxy (MBE), and their high crystalline structure is proven by the bright photoluminescence and limited by T_1 values of T_2.

Sample with [InGaAs quantum dots in the cavity with Q-factor of 200] was used in Chapter 4, where we studied the dephasing and rephasing of the ensemble of TLS and controlled it by the Rabi oscillations. The QDs were chosen since their T_2 is large reaching about half of a nanosecond and in addition, it weakly depends on the applied laser power. The cavity is needed to increase the interaction of the QDs with the light. It results in an increase in the PE amplitude, and also in a reduction of the amount of the applied power needed to reach a certain pulse area.

Sample with [CdTe quantum well] was used in Chapter 5 to study the coherence storage in the resident electron subsystem. Background impurities create resident electrons in the QW, which are localized on the potential roughness or donor atoms and can be accessed optically via X^- and D^0X respectively. The differing localization depth and therefore resident election localization time allow us to study the microscopic dynamics of electron hopping.

Sample with [4 layers of InGaAs quantum dots in the cavity with Q-factor of 1000] was used in Chapter 6. The Q-factor of 1000 sufficiently rises their interaction with the light and still does not impact the pulse duration. The δ-layer of Si was used to supply the electrons to charge the QDs needed for X^- formation. The high amplitude of the PE from the sample allowed us to see the long-lived 3PE from the QDs.

3.1.1 InGaAs quantum dots in the cavity with Q-factor of 200

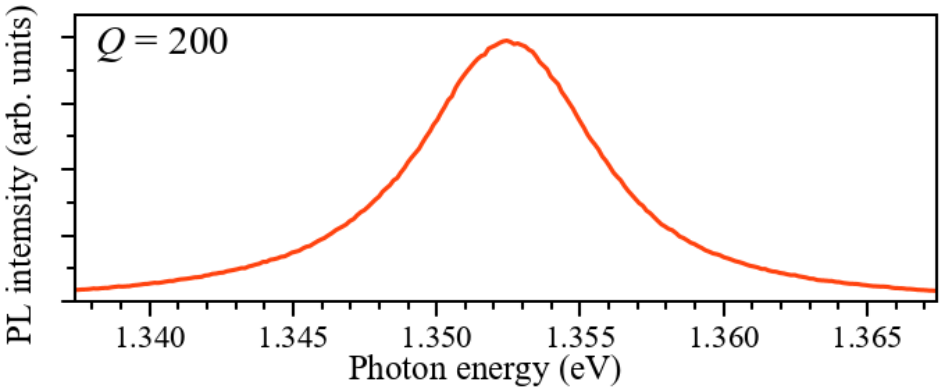

Figure 3.1: *PL spectrum of the sample with a single layer of QDs in the cavity with the Q-factor of 200. Measured at $T \approx 10$ K*

The sample (C3297) consists of a single layer of InGaAs QDs, surrounded by a λ-microcavity consisting of two AlGaAs Bragg mirrors. The QD density is about 2×10^9 cm^{-2}. A δ-layer of Si is placed 10 nm below the QDs in the matrix material, it plays the role of electron donor in GaAs and provides the electrons to charge QDs. The doping provides a donor density of 8×10^9cm^{-2}. The resident electrons provided by the doping layer charge the QDs, which allows one to form the X^- inside. The Bragg mirrors consist of alternating GaAs and AlAs layers with thicknesses of 68 nm and 82 nm, respectively. The top mirror has 5 pairs of them, while the bottom one has 18. It ensures the emission propagates in the top-side direction. The microcavity gives several advantages since it increases the intensity of the emitted PEs and also reduces the applied power needed to reach a certain pulse area [Pol+16; Wig+18].

The sample has a gradient of the cavity thickness along one axis. Thereby, the resonant energy varies in the spectral range of $1.343 - 1.362$ eV ($910 - 923$ nm) with a gradient of about 3.5 nm/mm. The investigated structure shows strong PL with the maximum centred at the photon energy of the photonic mode and a full-width at half

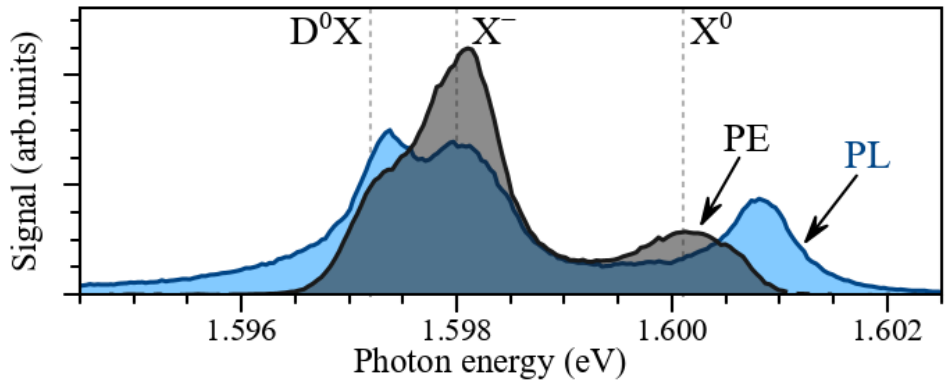

Figure 3.2: *Spectra of the PL and 2PE of the CdTe QW, both were measured at the temperature about 2 K. For the PE the $\tau_{12} \ll T_2$ of the X^0 i.e. about 10 ps.*

maximum (FWHM) of 7.4 meV, resulting in a quality factor of about 200. The sample was previously studied in Ref. [Pol+16].

3.1.2 CdTe quantum well

The sample (032112B) was used previously to study the spin-related phenomena by the PE [Sal+17b; Pol+17]. The structure consists of 20 nm-thick CdTe single QW placed between $Cd_{0.78}Mg_{0.22}Te$ barriers. The sample is grown on (100) GaAs substrate by MBE. The background of impurities creates resident electrons with the density of 10^{11} cm^{-2}, they are localized both at the potential fluctuations and on the donors [Sal+17b]. The blue line in Fig. 3.2 shows the PL spectrum measured at about 2 K. The PL peak with the highest energy is attributed to the neutral exciton X^0, which is centered at the energy 1.601 eV. The bell-like curve at the low energies clearly consists of two merged peaks, corresponding to the X^- seen at the energy of 1.598 eV and D^0X at the energy of 1.5974 eV. The D^0X has the lowest energy due to the stronger Coulomb interaction with the donor. In comparison to QDs the linewidth of excitations in QW is sufficiently narrower, which allows addressing the certain excitation spectrally.

The PE spectrum measured in the HHH polarization scheme is shown by the black line in Fig. 3.2, it represents the 2PE amplitude at the constant τ_{12}. It is qualitatively the same as the PL spectrum, the spectral features are seen at roughly the same energies in both techniques. The peaks corresponding to D^0X and X^- seen in PE are less separated than in PL. The spectrum can not be interpreted simply because of the spectral dependence of T_2, which makes the spectrum different at different τ_{12}. It is also important to keep in mind, that we see not the PE spectrum, but its convolution with the laser having a spectral width of about 0.5 meV. Nevertheless, we clearly see

three spectral features. The peak corresponding to X^0 has ≈1.5 meV lower energy compared to the one seen in PL. The energy shift occurs because of the short lifetimes of the high-energy excitons, which can be not localized and therefore lose their coherence rapidly. The features in the PE spectrum corresponding to X^- and D^0X fit well to the PL spectrum.

The previous research has revealed numerous sample properties, in particular in work [Pol+17] were determined the dipole moments having values of 73 D for X^- and 58 D for D^0X. In the work [Pol+19] the polarization dependences were used to define the trion and exciton contributions to the spectrum. A valuable breakthrough was done in the work [Lan+14], where the sample was studied using long-lived 3PE, where the optical coherence was stored in the resident electron spin, which allowed to estimate its properties, for instance: spin relaxation time $T_{2,e} \approx 5$ ns and g-factor absolute value $|g| \approx 1.52$. Anisotropy of the heavy hole g-factor was considered in the work [Pol+20b].

3.1.3 4 layers of InGaAs quantum dots in the cavity with Q-factor of 1000

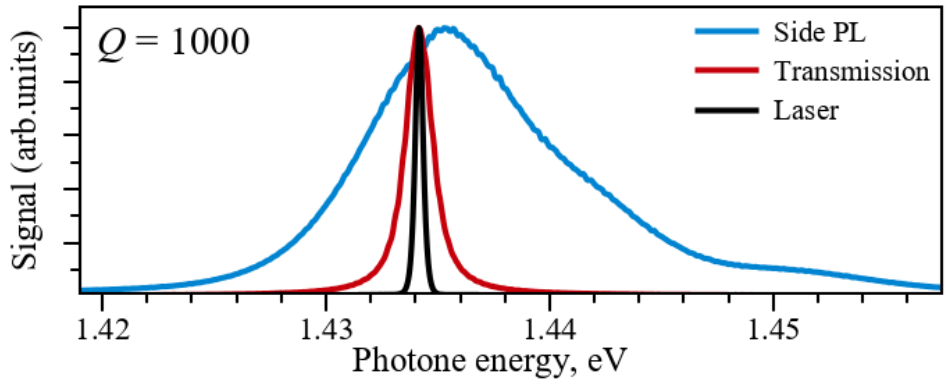

Figure 3.3: *PL spectrum of the sample, where 4 layers of QDs are placed in the cavity with the Q-factor of 1000*

The third sample we studied (#14833) has 4 layers of negatively-charged InGaAs QDs in the GaAs matrix. They are placed in the antinodes of the standing wave inside the microcavity, which consists of 11 and 14 pairs of AlAs/GaAs layers forming the Bragg reflectors. In order to adjust the resonant energy of the QDs to the microcavity and also reduce their spectral broadening, the sample was annealed at the temperature of 900 °C. The density of QDs in each layer is about 10^{10} cm^{-2}. The QDs were charged negatively by the Si δ-layer placed 64.5 nm below each layer of QD.

The cavity has a slight in-plane gradient of the resonant photon energy. We have chosen the spot with the resonant photon energy of 1.434 eV (864.6 nm) when the beam incidence was close to normal. The PL spectrum is presented in Fig. 3.3 by a blue line. The spectrum was measured from the sample's side to avoid the cavity impact. It has a bell-like shape with a weak shoulder at high energies. The maximum of the spectrum is at the energy of 1.435 eV, full width at the FWHM of 10 meV. The shoulder in the higher energies is seen at the energies above 1.45 eV, which is related to the excited states. The red curve shows a transmission spectrum, which has a Lorentzian shape. Its maximum is at 1.434 eV and FWHM is about 1.4 meV, consequently, Q-factor is about 1000. For a comparison the laser spectrum is shown here by the black line.

3.2 The experimental techniqes

In this section, we describe the experimental setups we have utilized. If some condition deviates from the chapter it will be mentioned in place.

3.2.1 Pulsed laser

The PEs were generated using the pulsed titanium-sapphire laser Mira-900 in the picosecond regime. The laser is tunable in the range of 700-1000 nm and has a repetition rate of 75.75 MHz. The pulsed laser was pumped by the Verdi-V10 continuous wave pump laser, emitting on the wavelength 532 nm with a power of about 10 W. The pulse duration and its intensity spectrum are shown in Fig. 3.4. The pulse duration is measured by autocorrelation using the heterodyne technique i.e. $G^{(1)}(t_1) \propto \int E_2^*(t)E_1(t-t_1)dt$, which is shown in Fig. 3.4(a). Its shape is close to a Gaussian with an FWHM of 5 ps, which corresponds to the electric field FWHM of 3.5 ps or intensity pulse duration of 2.5 ps. taking into account that both fields have the same Gaussian shape. The intensity spectrum is shown in Fig. 3.4(b), it can be well approximated by a Gaussian with the FWHM of 0.6 eV that corresponds to the pulse duration of about 3 ps. That value matches well the value we extract from the autocorrelation.

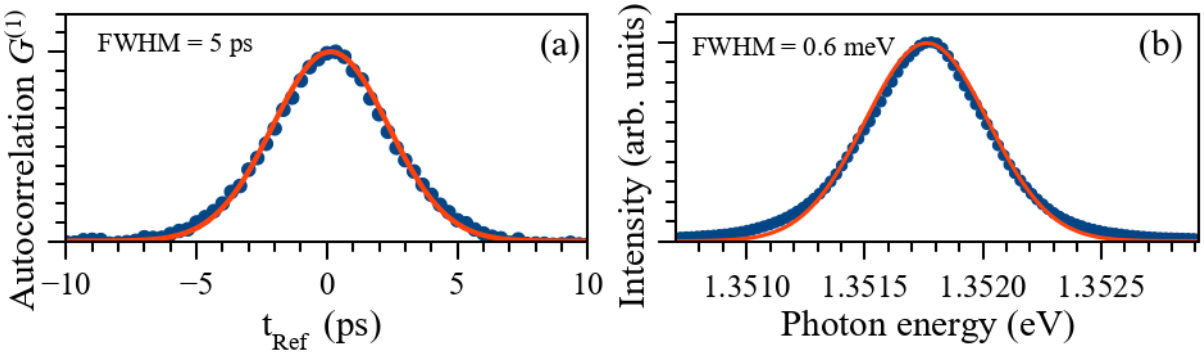

Figure 3.4: *Laser pulse properties: (a) envelop function of the pulse in the time domain, measured by an autocorrelation; (b) the intensity spectrum*

3.2.2 Cryostat

The sample was placed in the bath cryo, where it was immersed in liquid helium. The pressure was reduced to about 15 mbar, which turned the helium into a superfliud state with a temperature of about 2 K. At the low temperature, the amount of the non-equilibrium carriers reduces, which results in weaker scattering. On the other

hand, at low temperatures, localization of the charge carriers is possible on the more shallow potential fluctuations, and localization time on the potential fluctuations is longer. All that results in the prolongation of the T_2, which is limited in the case of low temperature by recombination, not temperature effects. Another advantage of the 2 K compared to the higher temperatures is not boiling liquid helium, which does not distort the laser beams passing through.

A temperature of 6 K and higher can be reached in the variable temperature insert (VTI) in the helium vapour, the certain temperature is set as a balance of the helium vapour flow and the heater power using the PID controller. We have used the special cryo with the split superconductive coils inside, which allowed us to create a homogeneous magnetic field up to 6 T in the sample. We used the Voigt geometry, i.e. the magnetic field is directed in the plane of the sample and almost perpendicular to the incident laser beam.

3.2.3 Photon echo: setup and detection

For the implementation of the 2PE and 3PE experiments, the laser beam was split into four beams using the beamsplitter cubes: three pulses hitting the sample and the reference pulse needed for the heterodyne detection. The first pulse was directly sent to the sample, so we count the time relative to the pulse. Meanwhile, the second, third, and reference pulses were passed through the individual delay lines, which are made out of mechanical one-dimensional high-precision translation stages with the triple-mirror hollow retroreflector mounted on top of them. In order to double the possible range of delays, the beams were sent via the delay lines twice. Afterwards, the second and third pulses were merged in order to hit the sample with the same wavevector, but with different delays. The same wave vectors of the second and third beam ensure the 2PE and 3PE generation with the same wavevector, which allows one quickly switch between the measurements. We count the time relative to its pulse arrival and assign time interval τ_{ij} as a delay between the i^{th} and j^{th} pulse.

The experimental condition corresponding to the 2PE formation is schematically shown in Fig. 3.5 and does not differ sufficiently from the 3PE. The pulses hit the sample with the angles about 3° and 4° for the $\vec{k}_1$ and $\vec{k}_2 = \vec{k}_3$ (for the 3PE) respectively. The laser beams passed through the spherical mirror with a focal length of 500 mm and were focused on the spot with a size of about 400 μm in diameter. Before the mirror, each beam passed through the Glan prism to ensure the linearity of the polarization and afterwards half waveplate to vary the angle of the linear polarization allowing us to implement the various polarization protocols. Optionally, one could set the second Glan prism, and then the rotation of the waveplate could control the power.

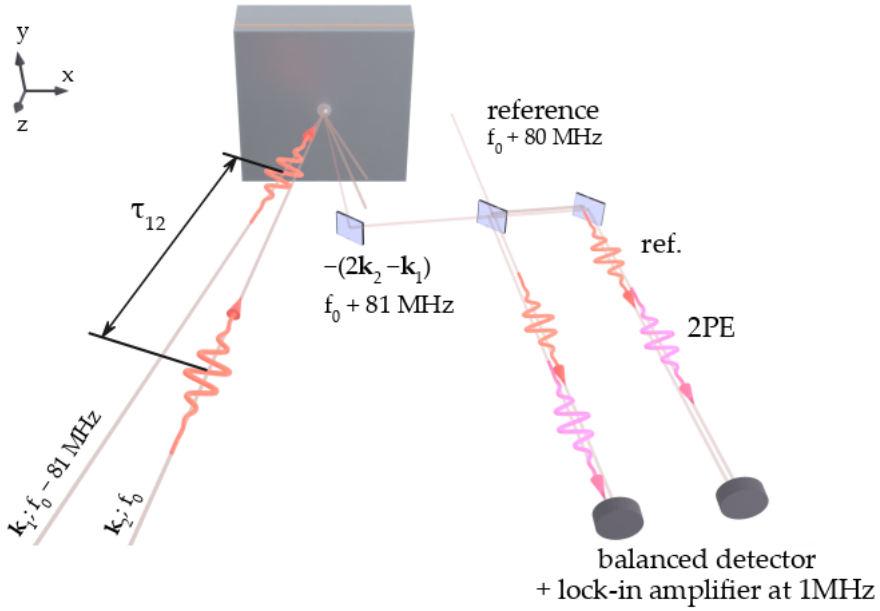

Figure 3.5: *The 2PE formation by a sequence of two pulses and its detection using a heterodyne technique.*

The generated FWM signal propagates with the wavevector $2\vec{k}_2 - \vec{k}_1$ in transmission geometry and therefore can be spatially separated since it has angle 5° in both 2PE and 3PE cases. The signal was collected by the spherical mirror and sent through the analyzing polarizer (Glan prism) to the balanced photodetector. Meanwhile, the reference pulse went directly to the photodetector avoiding the sample in order to see the interference between it and the PE signal. The beams were mixed at a beam splitter in such a way that their cross-sections and wave vectors coincided. The two resulting beams were sent to the balanced detector.

Since the FWM signal is rather weak and the spatial separation of the PE and other beams is not enough to separate the signal from the background, the heterodyning technique is applied. The two acoustooptic modulators (AOM) are shifting the optical frequency by -81 MHz and $+80$ MHz of the first and reference pulses respectively. Taking into account the frequency relation, the resulting frequency of the PE is $f_{FWM} = 2f_2 - f_1 = f_0 + 81$ MHz, where the f_0 is an original laser frequency. The reference pulse has a frequency of $f_{\text{Ref}} = f_0 + 80$ MHz, which makes the PE and reference beam beat on the differential frequency of $\Delta f = 1$ MHz. The DC component is canceled due to the balanced detection scheme, which also doubles the interference intensity. The signal was detected by the lock-in amplifier operating on the differential frequency Δf, which gave us $|E_{\text{FWM}} E_{\text{Ref}}|$ value. Since the power and therefore field of the reference pulse remained the same, the detected signal is proportional to the FWM amplitude.

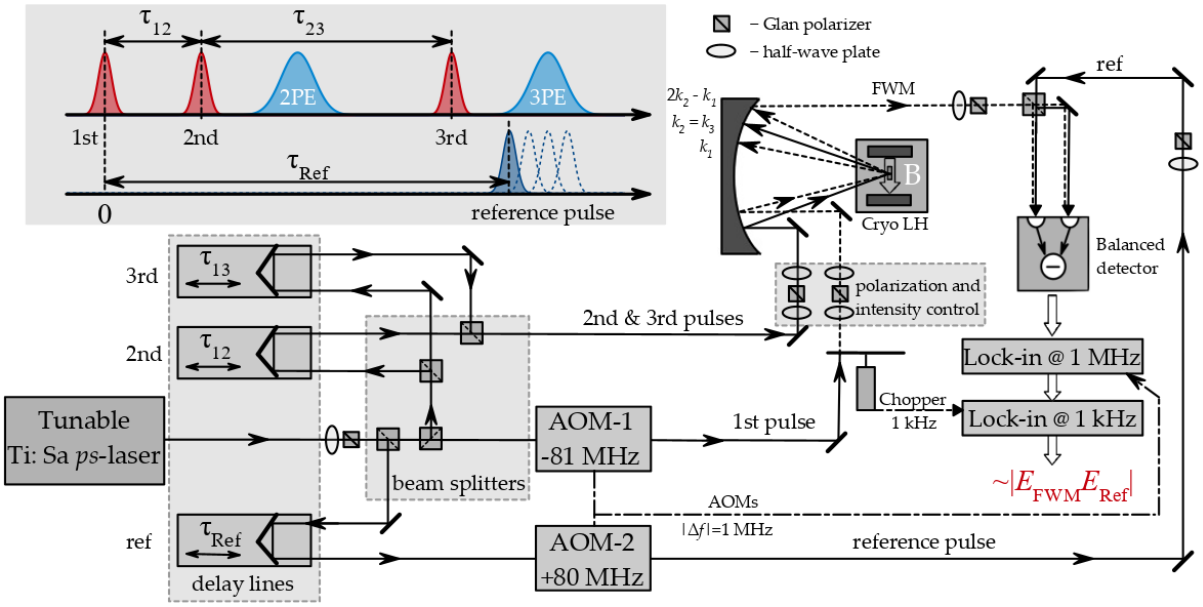

Figure 3.6: *Scheme of the experimental setup for the three-pulse photon echo formation and detection using a heterodyne technique with a double lock-in amplifier.*

Since we do not control the light's phases in the setup, we can only obtain the unsigned amplitude of the E_{FWM}. For a better signal-to-noise ratio, we used the second lock-in amplifier operating on a frequency of about 1 kHz. The first pulse was passed through a mechanical chopper wheel modulating it with the corresponding frequency.

The experimental setup is schematically shown in Fig. 3.6, where we show how each beam passes through the setup. First, we control the integral power coming to the setup from the laser by a set of the half-wave plate and the Glan polarizer. Then, with three beam splitters, we split the laser beam into four beams. Depending on the version of the setup we used non-polarizing beam splitters or polarizing combined with the half-wave plates in order to gradually vary the power between the beams. The third beam was passed through the neutral filter in order to vary its power relatively to the second one. All the beams except first go then to delay lines, where they pass through the hollow retroreflectors and return back. The latest setup revision consists of the two 1 m long delay lines for the second and ref pulses, while the third delay line is 0.4 m long. In order to extend the covered time range, the beams returned from the 1 m delay lines were redirected here again using extra retro-reflectors, so in total, they could pass 4 meters of the way covering 13.3 ns, while the laser's repetition period is 13.2 ns. Then the second and third beams were merged on the beam splitter in order to have the same wavevector arriving at the sample. The first and the reference beams passed through the AOMs after the delay lines, so their central frequencies have changed.

Before hitting the sample, the polarization and the intensity of the three beams were controlled by a sequence of the Glan polarizers and half-wave plates as highlighted in the module *polarization and intensity control*. The first pulse was modulated by a chopper introducing a frequency of 1 kHz. The intensity of the reference pulse was also controlled by the sequence of the half-wave plate and Glan polarizer. The set of the half waveplate and polarizer also was set in the detection of the FWM, it allowed us here to pick the certain polarization of the echo to analyze only its behaviour. The FWM signal and the reference pulse were mixed on the beam splitter and directed to the photoelements of the balanced photodetector. The signal went to both recievers of the photodetector with a different phase, which doubled the observed signal. We have also substracted the DC component and cut the frequencies far below 1 kHz and far above 1 MHz by the long and short-pass electric filters, in order to reduce the noise. The inset in Fig. 3.6 shows us the temporal diagram of the applied and observed pulses and the corresponding time intervals τ_{ij} between them. Here i&j correspond to a number of the pulse. For simplicity in the scheme we have omitted the telescope, periscope, and some other auxiliary optical elements.

3.2.4 Time-resolved Kerr rotation and resonant spin amplification

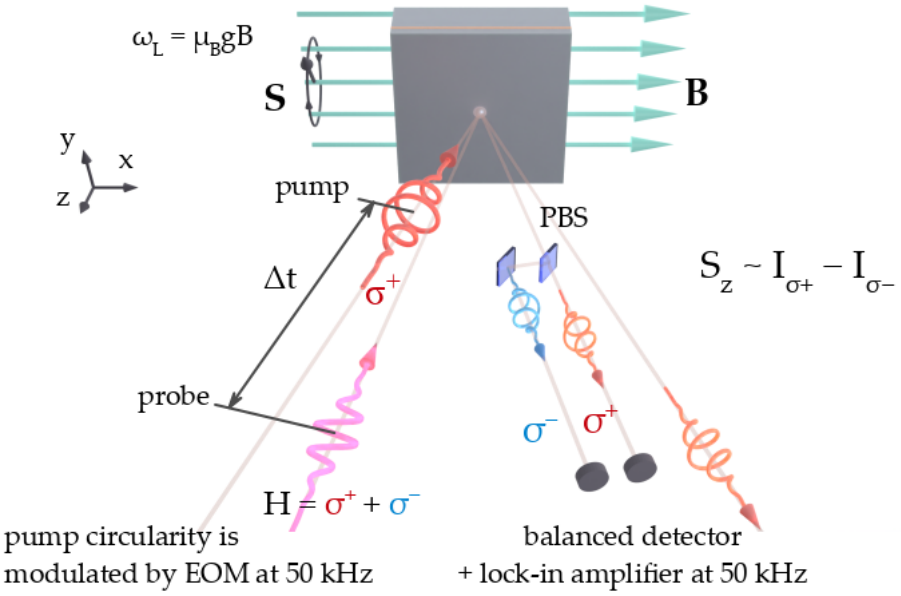

Figure 3.7: *Time-resolved Kerr rotation experimental technique. Formation of the spin polarization by a σ^+-pump pulse and the detection the ellipticity of the reflected light*

Implementation of the pump-probe spectroscopy in the form of time-resolved Kerr rotation requires a set of two pulses with a variable delay Δt between them, which

is schematically shown in Fig. 3.7. First, the circularly polarized pump pulse arrives and initializes the macroscopic spin polarization. Its polarization switches between σ^+ and σ^- by elastooptical modulator at the frequency of about 50 kHz, the device works as a rapidly switchable quarter waveplate. The corresponding timescale 20 μs is sufficiently bigger than the spin relaxation times of a few nanoseconds. Permanent modulation is needed to avoid nuclear polarization and related effects. The modulation frequency was used for the detection by the lock-in amplifier.

The probe pulse was always linearly polarized, but its reflection from the sample with a spin polarization gives some elliptically polarized compoment because of different absorption of the σ^+ and σ^- components. We passed the probe pulse through the quarter waveplate to transform the ellipticity to the angle of the linear polarization. In this case, the angle of the polarization is proportional to the S_z component. The probe pulse must be at least an order of magnitude less intense to be considered non-perturbative. A detailed description of the techniques can be found in the works [Zhu+07; Gla12].

The RSA was done using the same experimental setup, but the probe pulse arrived right before the pump. The magnetic cryostat allowed smoothly vary the magnetic field, which is needed to observe the RSA dependences. Further reading on the topic is Ref. [GI08] and references inside.

The experiment was done using the setup described in Fig. 3.6. We used the first pulse as a probe, and the third as a pump. In the scheme, the probe pulse remained static, while the temporal position of the pump pulse was varied during the experiment. The beam splitter in the detection scheme was replaced by the Wollaston prism.

Chapter 4

Coherent control of the dephasing and rephasing in the inhomogeneously broadened ensemble of quantum dots

Coherent control of the two-level systems or quantum emitters is advantageous for modern quantum technologies [SZ97] and especially for quantum information processing [Ima+99] or storage [Lvo+09; Lan+14]. The QD is a great candidate for the role of such TLS, because of their long decoherence times which weakly depends on the applied power of the resonantly tuned laser.

Nevertheless, in order to obtain efficient light-matter coupling, ensembles of QDs are required [Tit+10; Lvo+09]. Since most of the epitaxially-grown QDs are made by the self-organization mechanism of the Stranski-Krastanow their sizes within the ensemble vary. It results in the inhomogeneous broadening of their optical spectra and is a driving force of the dephasing. The dephasing can be strong enough to impact the system's temporal evolution even during the coherent drive by a laser pulse [Pol+16; Pol+17].

The chapter dedicates to the dephasing and rephasing control in the inhomogeneously broadened ensembles of QDs. Here we show a method of dephasing inhibition by coherent manipulation of the state. The 2PE technique was used as a tool for monitoring because of its high sensitivity to the dephasing and rephasing processes.

4.1 PE timing controlled via the freezing of dephasing or rephasing

The 2PE formation consists of the consequent dephasing and rephasing of the inhomogeneously broadened system of TLS, with a transition between them by the 2π-pulse. A detailed description of the mechanisms responsible for the 2PE formation can be found in Sec. 2.3.4. Hence, modification of the phase evolution during 2PE formation can make a significant impact on its temporal profile and position [AE75], which makes 2PE a great tool for the dephasing investigation.

The approaches to control the phase evolution in order to avoid the dephasing were developed in the methods of nuclear magnetic resonance and electron spin resonance, which are siblings of the PE [Sli13; AE75]. The most prominent methods of dephasing control are two variations of the dynamic decoupling (Carr-Purcell and Carr-Purcell-Meiboom-Gill sequences) [CP54; MG58]. They both are based on the π-pulse sequence, applied with a periodicity of $2\tau_{12}$ starting from the second pulse. In the approach, the individual TLS with detuning Δ_i cannot obtain the phase exceeding $\Delta_i\tau_{12}$. The procedure ensures a sequence of the dephasings and rephasings with a recovery of the macroscopic polarization at $2n\tau_{12}$ (where $n \in \mathbb{N}$), that makes up the Carr-Purcell method. The Carr-Purcell-Meiboom-Gill sequence is a modification of the Carr-Purcell sequence and implies certain phase relations among the applied pulses. Such phase control of the pulses can be naturally achieved in the radio range but is sufficiently problematic for the optical range of the electromagnetic waves. Another option to inhibit the dephasing is spin locking. Despite it implies continuous driving by an electromagnetic field, it also secures a periodic phase inversion as Carr-Purcell sequence does [HH62].

Some approaches were used for the atom ensembles using visible light, in the works [Sle+86; Yod+84; Car+84] inhibition of dephasing was demonstrated through locking of the macroscopic polarization and the PE shape. Control of the PE timing was recently applied to the rare-earth nanophotonic crystal using symmetrically detuned ac Stark pulses, which result in compression of the atomic frequency comb and a following delay of the emitted PE [Zho+17]. Nevertheless, the optical control of the PE timing by the resonant optical pulses was not yet considered. Such an approach was proposed in Ref. [Ros18], which has theoretically predicted a temporary slowing down or "freezing" of the dephasing under the action of the resonant 2π-pulse. The chapter dedicates to the experimental proof of the principle of the concept. The experimental data are accompanied by the corresponding modeling.

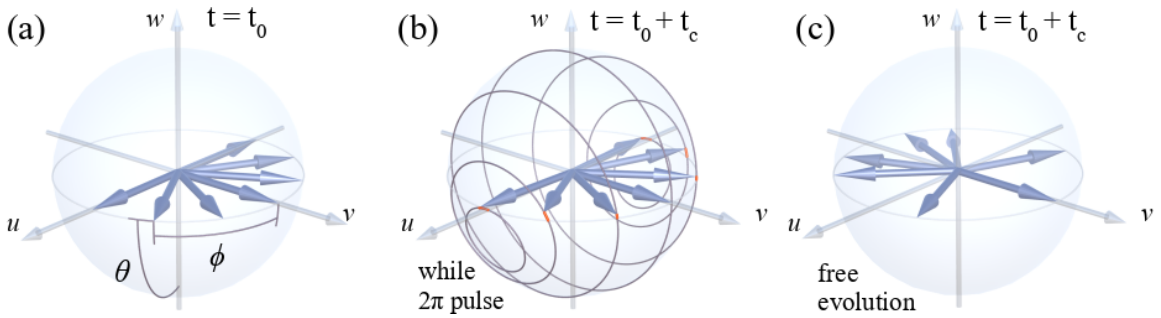

Figure 4.1: *Schematic illustration of coherent evolution of TLS ensemble on the Bloch sphere. Panel (a) shows a partial dephasing of excitons with different detunings at time t_0 after excitation with a $\pi/2$-pulse. Panel (b) shows nutation of excitons by the action of control pulse with a pulse area of 2π (solid grey lines) and weak deviations from pure 2π rotations due to detunings at time $t_0 + \tau_C$ with $\tau_C \approx \Delta^{-1}$, where Δ corresponds to maximum detuning of the inhomogeneous ensemble (red lines) (c) Distribution of Bloch vectors at the same time as in (b) but without the impact of the control pulse.*

4.2 Phase evolution and its control

Now we consider an inhomogeneously broadened ensemble i.e. homogeneous linewidth of individual transition γ is narrower than the dispersion of the ensemble Δ_{nh}. As we have shown in Sec. 2.2, the state of the TLS can be described by the vector in the Bloch sphere as:

$$(u, v, w) = (\sin\theta \sin\varphi, \sin\theta \cos\varphi, -\cos\theta), \tag{4.1}$$

its definition in the uvw-coordinates is shown in the Fig 4.1(a), where co-altitude θ corresponds to the population and the phase φ represents a phase of the TLS.

If we initialize the ensemble by $\pi/2$-pulse, it dephases rapidly and its macroscopic polarization washes out, which is shown in Fig. 4.1(a). The visualization was done using the Bloch Eqs. 2.12. During the dephasing, the vectors are increasing their phases as $\varphi_i = \Delta_i t$ respectively to their individual detuning Δ_i, which leads to the distribution of the vectors within uv-plane.

Now, in order to freeze the dephasing we apply the 2π-pulse with a control pulse duration of τ_C, which makes a complete turn of the vectors around v-axis as shown in Fig. 4.1(b). Assuming the Rabi freuqncy higher than the inversed inhomogeniety of the ensemble Δ, the 2π-pulse drives a system into the state close to initial. Meanwhile, the turn under 2π-pulse takes τ_C, during the time the system is effectively frozen. So, its dynamics is defined by the rotation around v-axis. During the control pulse action, the dephasing does not take place even though the vectors had quite complex dynamics on the Bloch sphere. Surely, the multiple turns bring us to the same result i.e. the freezing takes place when $\Omega_R \tau_C = 2\pi n$ (where $n \in \mathbb{N}$).

During the 2π-turn, the resonant TLS with $\Delta_i = 0$ make exactly a complete turn. Meanwhile, Rabi frequency of the detuned ($\Delta_i \neq 0$) TLS $\sqrt{\Omega_R^2 + \Delta^2} > \Omega_R$ is bigger than the resonant one has. Therefore, the TLS with a detuning do more than an exact turn and stops slightly above the uv-plane as shown in Fig. 4.1(b). The deviations are indicated by the small orange lines. When $\Omega_R \gg \Delta$, the generalized Rabi frequency might be represented as $\tilde{\Omega} \approx \Omega_R[1 + (\Delta/\Omega_R)^2/2]$, which allows one to estimate the path the system went. Moreover, the path exceeding the full turn mostly contributes to the θ increment rather than φ. There is no strict requirement for the pulse duration τ_C or shape, the freezing will also take place for $\tau_C\Delta > 1$. The requirements we assume are only $\Omega_R \gg \Delta$ and $(\Delta/\Omega_R)\tau_C\Delta \ll 1$.

So, when the system is shown Fig. 4.1(a) does a complete turn under 2π control pulse with a duration τ_C it results in the state shown in the Fig. 4.1(b). It is interesting to compare with a case of free evolution, which is shown in Fig 4.1(c). The phase increment sufficiently exceeds the case of the temporary frozen system, where the position of the vectors just slightly deviates from the initial one. Despite our illustrative example, where the system did not lose its macroscopic polarization, the effect can occur in any case since its action is microscopic and does not depend on the ensemble macroscopic polarization existence.

Application of π-pulse to the dephased ensemble of TLS as any of shown in Fig. 4.1 switches the dephasing to rephasing, which recovers a macroscopic polarization when the system spends the same time by dephasing and rephasing. When the pulses taking a part in initialization and switch between dephasing and rephasing fulfill the

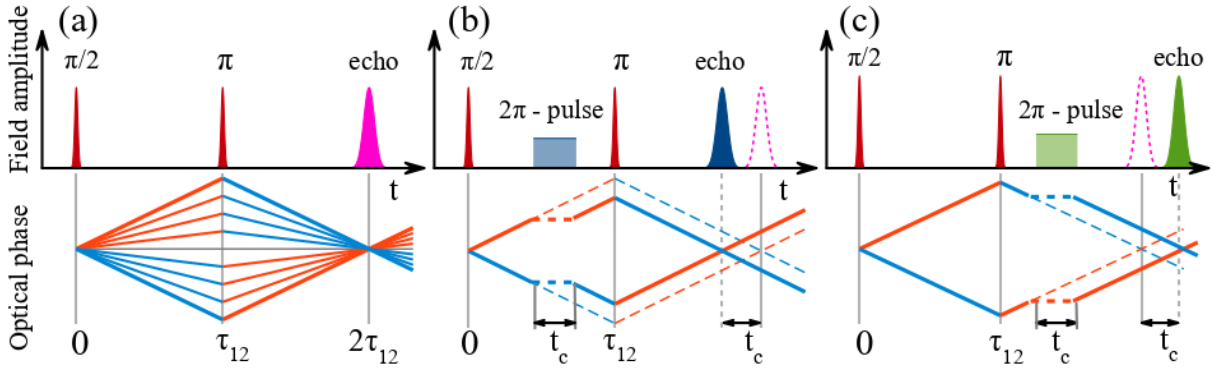

Figure 4.2: *(a) Phase evolution of TLS in a 2PE. Positive ($\Delta_i > 0$) and negative ($\Delta_i < 0$) detunings of the exciton resonances are shown by red and blue lines, respectively. First and second excitation pulses are shown in red and magenta peak corresponds to the primary 2PE. (b) and (c) 2PE in under impact of 2π pre-pulse (blue) or post-pulse (green) leading to an advanced and retarded 2PE peak. The evolution of optical phase in presence of the control pulse is shown by solid lines, while dashed lines indicate the evolution without the control pulse.*

FWM conditions, the macroscopic polarization formation manifests in the 2PE. The TLS phase bahaviour during the process is schematically shown in Fig. 4.2(a). We would like to highlight here the fact, since the system spends exactly the same time by dephasing and rephasing the 2PE appears exactly at the $2\tau_{12}$ after the first pulse action. If we now apply the 2π control pulse during the dephasing of the ensemble, it spends τ_C less time by dephasing and consequently requires less time to rephase back and form 2PE. The 2PE appears earlier, the shift corresponds to the control pulse duration τ_C, which is schematically shown in Fig. 4.2(b). Since the dephasing goes linearly, it is clear, that the effect does not depend on the certain moment of the control pulse application during the dephasing. The rephasing of the ensemble is based on actually the same phase evolution of the individual TLS as dephasing, so the 2π control pulse can actually freeze the dephasing samely, as shown in Fig. 4.2(c). When we freeze the rephasing, the system obviously needs more time to recover its macroscopic polarization and the 2PE forms later with a delay corresponding to the control pulse duration. Thus, we have shown how the effect of the dephasing or rephasing freezing can be observed using the photon echo technique. We call the control pulse applied in the time range $(0; \tau_{12})$ - pre-pulse, while in the time range $(\tau_{12}; 2\tau_{12})$ we call post-pulse.

The solution of the optical Bloch equations gives us a certain phase evolution, which is shown in Fig. 4.3(a). We assume that the first pulse always does a turn around the (100) axis on the Bloch sphere. The certain axis in uv-plane along which the second pulse does a rotation depends on its phase relation with the first pulse. The two limiting cases are possible: a rotation around the (100) or (010) axis. The only difference between them is in the phase of eventual echo. The former option leads to gathering the vectors after rephasing along $-v$, while the latter one is along the v-axis. In order to keep the phase diagram simple we show here the latter case.

Samely to the second pulse, the control pulse can make a turn along (100) or (010), the cases are shown in Fig. 4.3(b&c). The first we see here, is that both 2π control pulses lead to the same shift of 2PE, despite a different behaviour of the phases during the turn. That fact is important for the experimental data analysis since we do not control the phases of pulses and therefore it fluctuates within a train of pulses.

As a summary, we see how the control pulse with an area of 2π in particular or $2\pi n$ (where $n \in \mathbb{N}$) in a more general case freezes the phase evolution of the detuned TLS. In such a way one can freeze either dephasing or rephasing depending on the moment of the control pulse arrival. The freezing does not depend on the exact moment of the control pulse arrival within pre-pulse or post-pulse regimes. The freezing effect can be detected by 2PE timing, but the concept does not originate from PE and can be applied to any other inhomogeneously broadened ensemble of TLS.

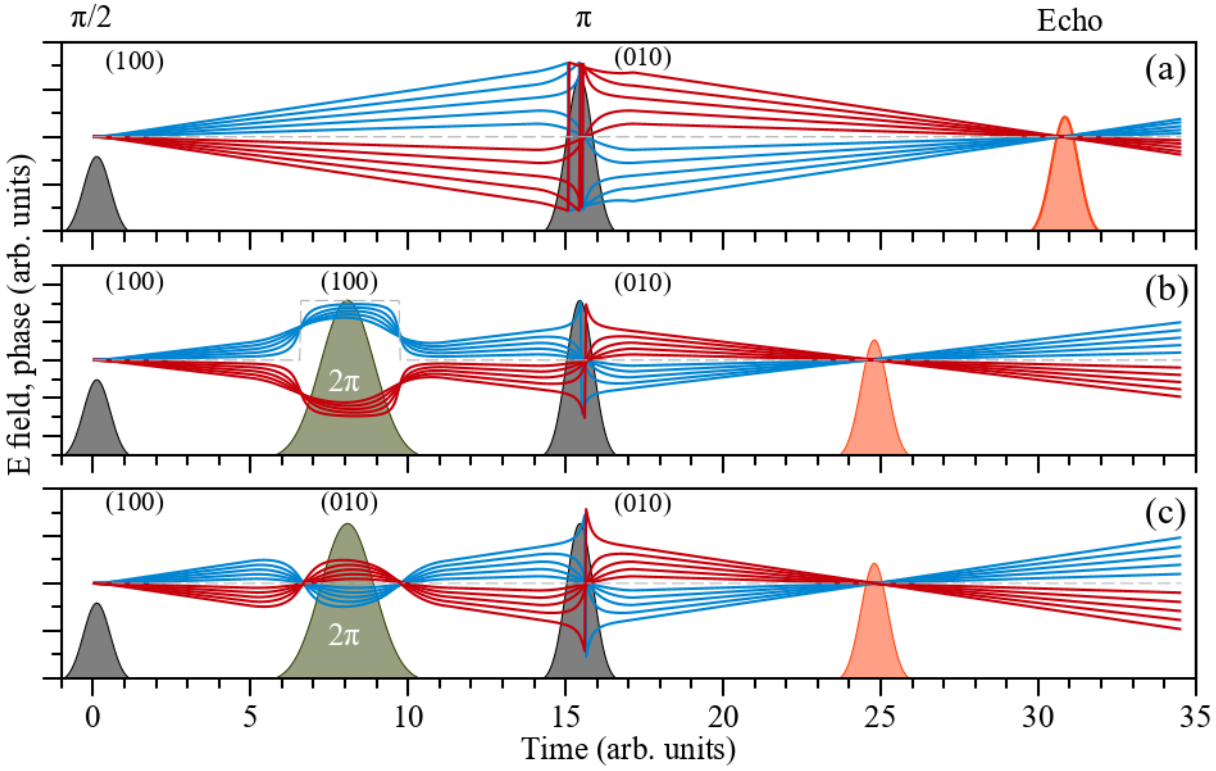

Figure 4.3: *Phase behaviour (a) during 2PE formation; (b&c) during the freezing by 2π turn around (100) and (010) axis correspondingly with a subsequent 2PE formation.*

In the following sections of the chapter, we show the experimental verification of the freezing, which is accompanied by the corresponding modelling using the optical Bloch equations as Eqs. 2.12. The effect will be demonstrated on the self-assembled InGaAs QDs placed into the cavity with Q-factor of 200, the sample is described in Sec. 3.1.1. The experimental technique is described in Sec. 3.2.3.

4.3 Experimental verification

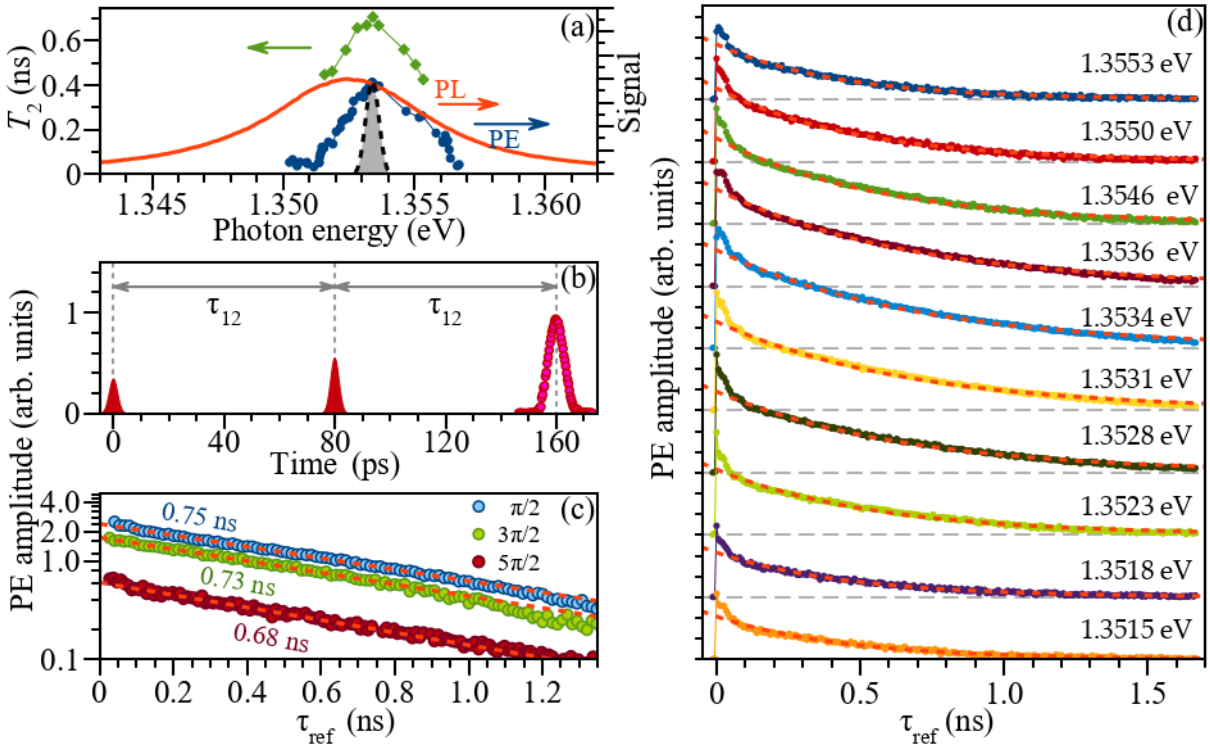

Figure 4.4: *Photon echo power and spectral dependences from the QDs in the cavity with Q-factor of 200. (a) spectral dependences of the T_2 (green), photoluminescence (red) and the 2PE amplitude (blue); (b) the 2PE temporal profile; (c) 2PE transients in respect to the first pulse area θ_1; (d) transients measured at the different laser photon energy. $T = 2$ K*

The PL spectrum of the InGaAs QDs embedded in the microcavity with the Q-factor of 200 is shown in Fig. 4.4(a) by the red solid curve. Its shape is close to Lorentzian with a maximum of around 1.3525 eV and FWHM of about 7.4 meV. That shape is defined by the microcavity properties, not QDs. The laser spectrum is shown here by the black dashed line, it is narrower than the cavity mode and has a width of about 0.5 meV and therefore it enters the microcavity without spectral or temporal distortions. A typical signal we measure is shown in Fig. 4.4(b). Two laser pulses represented by the red peaks are arriving to the sample with a delay $\tau_{12} = 80$ ps between them. The sequence initiates 2PE, which appears at the time $2\tau_{12}$. Its temporal profile is close to a Gaussian with an FWHM of about 6.5 ps. Since the temporal profile is a convolution of the 2PE and the reference pulse, we estimate the 2PE field duration as 4 ps. Now we are going to characterize the properties of 2PE from the sample to choose the optimal conditions for the freezing of the dephasing.

In order to estimate the power sustainability of the 2PE, we have measured 2PE(τ_{12})

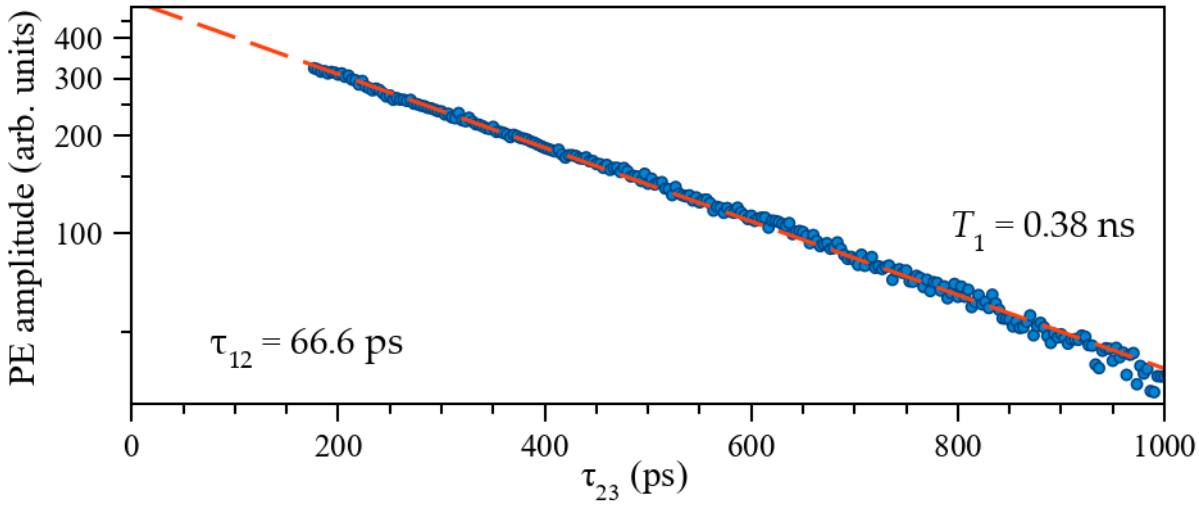

Figure 4.5: *3PE decay with τ_{23} from the QDs in the cavity with Q-factor of 200, measured at $T = 2$ K, using HHHH polarization protocol. Blue signs represent the experimental data, red dashed curve the single-exponential fit.*

at different first pulse power. The Fig. 4.4(c) shows us the three 2PE dependence on τ_{12} measured when we kept $\theta_2 = \pi$, but applied θ_1 of $\pi/2$, $3\pi/2$, or $5\pi/2$. The pulse energy has a quadratic dependence on the field and therefore $5\pi/2$ implies 25 times higher power than $\pi/2$. All three dependencies are exponential, and can be well described by $P_{\mathrm{PE}} \propto \exp(-2\tau_{12}/T_2)$. The higher pulse area corresponds to a lower signal amplitude. The effect has two known reasons: inhomogeneouls excitaion [Pol+17], and interaction with the phonons [Gri+22]. Despite a dramatic drop of the 2PE amplitude, the decay times T_2 remain roughly the same being 0.75, 0.73 and 0.68 ns for the $\theta_1 = \pi/2, 3\pi/2$, and $5\pi/2$ correspondingly.

In Fig. 4.5 we show 3PE decay, the blue dots represent the signal, the red dashed line represents a fit by a single exponential decay. From the 3PE we have extracted $T_1 = 0.38$ ns, which is twice shorter than the T_2 we observe under the low excitation. That clearly shows us that the T_2 is mostly defined by the radiative decay and EID is rather weak in the system, especially when the first pulse area is small compared to 2π. The property is essential for the observation of the robust Rabi oscillations [Pol+17].

Spectrally, the cavity mode is an order of magnitude wider than the laser. Fig. 4.4(d) shows the 2PE decays, which are measured at the different spectral points of the cavity. All of them decay exponentially with a fast component at the very beginning. The 2PE amplitudes are almost twice bigger at the centre of the spectral range than on its sides. The $T_2(\lambda)$ extracted from the curves is shown in Fig. 4.4(a) by green rhombuses. It reaches 0.75 ns at the centre and drops down to 0.4 ns at the sides of the range. We

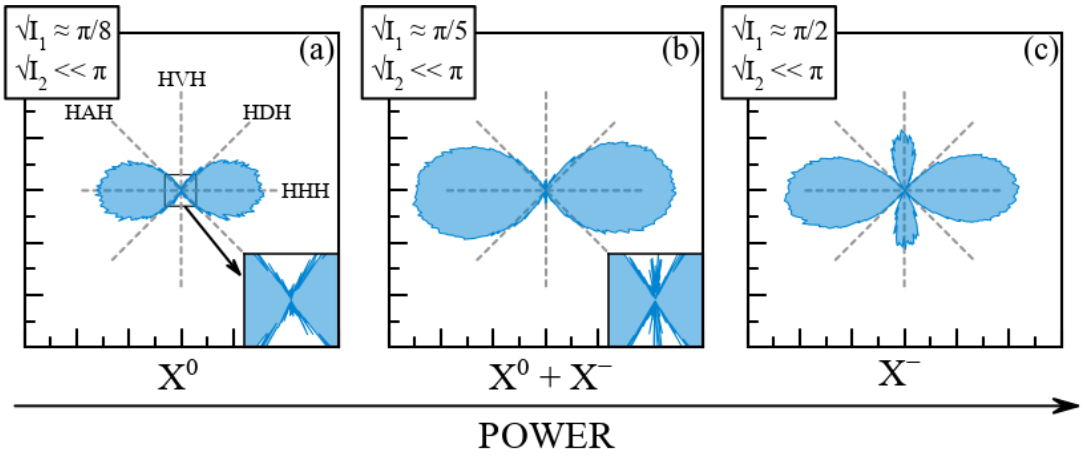

Figure 4.6: *Polarization dependence of the 2PE amplitude under different excitations. (a) excitionc behaviour at the low power; (b) a complex excitonic-trionic behaviour at the intermediate excitation ; (c) trionic behaviour at the moderate-high excitation.*

have additionally measured the spectral dependence of the 2PE amplitude, varying the laser's wavelength keeping $\tau_{12} \approx 10$ ps. It is shown by blue dots in Fig. 4.4(a). THE 2PE spectrum has an asymmetric bell shape with a maximum of roughly 1 meV higher than one of the PL spectrum, and an FWHM of about 4 meV. The T_2 and 2PE amplitude spectral dependences are correlated, the lower amplitude corresponds to a lower decay time. For the following operation, we have chosen the laser photon energy of 1.3534 eV ($\approx$ 916 nm) where the 2PE has the maximal amplitude and also the longest T_2.

We have applied the polarimetry technique to determine a type of excitation localized inside of QDs, the technique is described in Sec. 2.4.1 or work [Pol+19]. The polarization dependences HRH under different applied power are shown in Fig. 4.6. We clearly see, that under a low excitation i.e. $\theta_1 \approx \pi/8$, $\theta_2 \ll \pi$ the polarization dependence corresponds to the neutral exciton X^0 H component in the HRH polarization scheme follows $cos(\phi_{12})$, the signal in HVH is absent while clearly presents in HDH. Here ϕ_{12} is an angle between the first and second pulse linear polarizations. At the bigger areas of the first pulse $\theta_1 \approx \pi/5$, we already see a weak HVH signal, while the dependence itself remains clearly excitonic. The following rise of the first pulse area washes out the excitonic shape of the polarization dependence and makes it almost purely trionic following $cos^2(2\phi_{12})$. The HDH component sufficiently reduces relatively HHH and HVH. Thus, under the lower pulse areas, the 2PE has an excitonic polarization dependence, while when the first pulse area reaches $\pi/5$ or higher has a trionic dependence.

Variation of the pulse area results in the 2PE amplitude periodic modulation, they

depend on the pulse areas as $\sin(\theta_1)\sin^2(\theta_2/2)$ [BM11] and Sec. 2.2.2. Due to the inhomogeneity impact, the odd maximums in the dependence on θ_1 appear slightly advanced, the effect was studied in Ref. [Pol+16]. We have measured temporal profiles of 2PE at different $\sqrt{I_1} \propto \theta_1$ on the sample we study, they are represented in the two-dimensional (2D) plots in Fig. 4.7 where one axis corresponds to the temporal position of the reference pulse, and another to the area of a pulse. The (a) and (b) represent HHH and HVH polarization protocols. The delay between pulses $\tau_{12} = 40$ ps. Here the second pulse had an area of about π to keep the maximal 2PE amplitude. In accordance with the expectations, at the areas of the first pulse below $\pi/2$ ($\approx \sqrt{I_1} < 1 \cdot 10^{-4}$ J/cm) the echo appears around 80 ps $= 2\tau_{12}$. The higher first pulse area leads to the drop of the 2PE amplitude and even split the 2PE temporal profile into two smaller peaks when one becomes slightly retarded and the second one appears roughly 5 ps earlier. When the θ_1 reaches $3\pi/2$ the 2PE at $2\tau_{12}$ fully disappears, and the only 5 ps advanced one remains. Its amplitude is roughly doubly lower compared to the maximum at $\pi/2$, as we mentioned it happens due to inhomogeneous excitation and the interaction with phonons [Pol+17; Gri+22]. The following maximum at $\theta_1 = 5\pi/2$ appears around $2\tau_{12}$, its amplitude has dropped even more in comparison to the lower θ_1 areas. The following maximum at $\theta_1 = 7\pi/2$ is weak and badly pronounced. In Fig. 4.9(a)&(b) we observe up to two full Rabi oscillations (2π rotations) within the range of the applied power $\sqrt{I_1}$ we used.

The oscillations are qualitatively the same for both the polarization protocols HHH and HVH, but they are differently pronounced and damped. The Fig 4.7(c) shows the θ_1 dependencies of 2PE amplitude at the constant $\tau_{\text{Ref}} = 76$ and 81 ps, which correspond to $3\pi/2$, and $\pi/2$ maxima. In Fig. 4.7(a) and (b) they are indicated by the dashed lines. The θ_1 dependencies are normalized on the maximum at $\pi/2$. We clearly see that the HHH curve reaches the maximum at $\theta_1 = \pi/2$ at almost twice the lower field. The maximum at the $\theta_1 = 3\pi/2$ has about 80% of the amplitude of $\pi/2$ for the HVH polarization protocol, while the HHH has only about 45%. As for $\theta_1 = 5\pi/2$, the 2PE amplitude in the HVH protocol is about 30 % of $\theta_1 = \pi/2$, while for the HHH it reaches only 20 %.

The 2PE temporal profiles with respect to the different $\sqrt{I_2} \propto \theta_2$ are shown in Fig. 4.7(d) and (e). Here $\tau_{12} = 40$ ps as previously and $\theta_1 \approx \pi/2$ in order to have a maximal 2PE amplitude at τ_{12}. In both cases, the signal decays with $\sqrt{I_2}$ and is modulated by Rabi oscillations. The normalized dependencies are quite the same, but in HHH 2PE amplitude is almost 50 % bigger. Independently on the polarization protocol the signal reaches maximum $\sqrt{I_2} \approx 2 \cdot 10^{-4}$ J/cm, the second maximum occurs at the roughly twice bigger $\sqrt{I_2}$. Normalized dependencies of the 2PE amplitude at $2\tau_{12}$

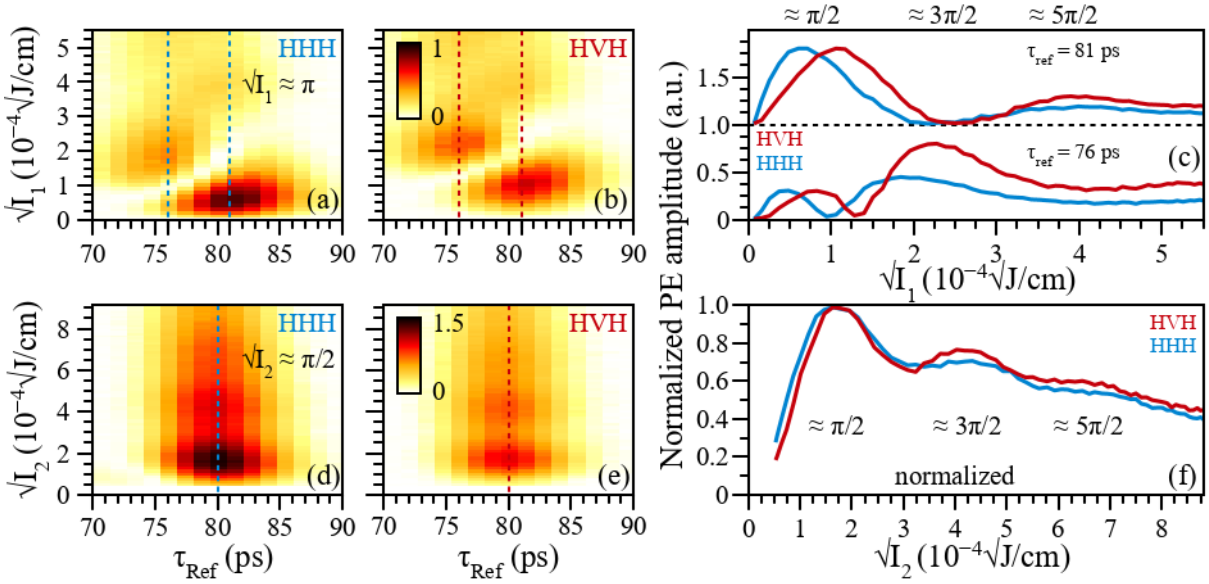

Figure 4.7: *Two-dimensional plots showing the dependence of the 2PE temporal profiles (x-axis) on the amplitude the first pulse: (a) $\sqrt{I_1}$ using HHH polarization protocol; (b) $\sqrt{I_1}$ using HVH polarization protocol; (c) the slices of $\sqrt{I_1}$ dependencies at $\tau_{\mathrm{Ref}} = 76$ and 81 ps. Samely organized two-dimensional plots as dependence amplitude of the second pulse: (d) $\sqrt{I_2}$ using HHH polarization protocol; (e) $\sqrt{I_2}$ using HVH polarization protocol; (f) the slices of $\sqrt{I_1}$ dependencies at $\tau_{\mathrm{Ref}} = 80$ ps.*

on $\sqrt{I_2}$ are shown in Fig. 4.7(f) by blue and red curves for HHH and HVH polarization protocols respectively. The behaviour of both 2PE dependencies on θ_2 is quite the same, excluding the higher contrast of the HVH i.e. the lower signal between the $\pi/2$ and $3\pi/2$ maximums.

Thus, due to the presence of both X^0 and X^- components in the optical response of the studied sample, the 2PE in the HHH polarization protocol is stronger, but the minima between the peaks are worse pronounced and the damping of the signal is stronger. It can happen because of the different dipole moments of X^0 and X^-, which have minima at slightly different pulse areas. For the following work, we choose the HVH polarization protocol, which gives us a signal only from the X^- subensemble.

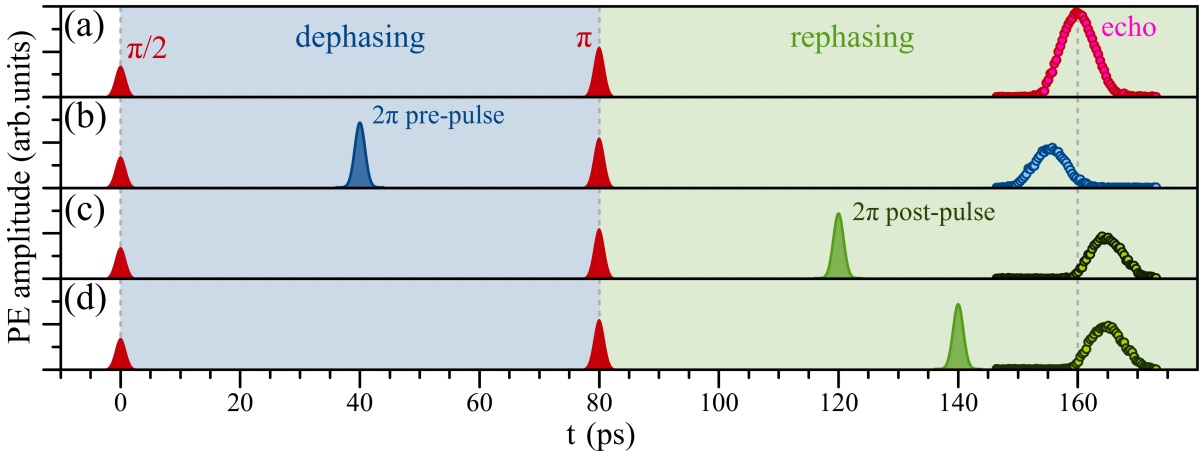

Figure 4.8: *Temporal profiles of the 2PE measured (a) without a control pulse; (b) with 2π pre-pulse; (c) with 2π post-pulse; (d) differently placed 2π post-pulse.*

4.4 Impact of control pulse on PE timing

Now we move to the experimental proof of the dephasing and rephasing freezing. The characterization has shown that the most suitable polarization protocol is HVH at the photon energy 1.3534 eV. We will use $\tau_{12} = 80$ ps in order to keep the signal strong enough but be free to vary the control pulse arrival moment in a wide range avoiding overlapping of the prime 2PE and ones formed by the first and control pulse or the 3PE made with the control pulse. We set the $\theta_1 \leq \pi/2$ and $\theta_2 \approx \pi$ to maximize the 2PE amplitude, the areas corresponding to the pulse energy densities of $I_1 = 4\,\mathrm{nJ/cm^2}$ and $I_2 = 23\,\mathrm{nJ/cm^2}$. At such conditions, the 2PE appears exactly at $2\tau_{12}$ as it shown in Fig. 4.8(a). Here the sequence of the applied pulses at $t = 0$ and 80 ps are schematically indicated by red peaks. During the time range (0, 80) ps the ensemble dephases, the range is highlighted by a blue area, while in the time range (80, 160) ps the ensemble rephases, the area is assigned by green colour. The 2PE temporal profile is shown by the magenta dots, its maximum is at exactly 160 ps and FWHM is about 6.5 ps.

Application of the 2π pre-pulse is shown in Fig. 4.8(b). It leads to ≈ 5 ps earlier 2PE formation. The shape remains close to Gaussian, but its amplitude is almost double lower, and its FWHM remains roughly the same. Application of the 2π post-pulse is shown in Fig. 4.8(c). The 2PE is formed ≈ 5 ps later, its shape is the same for the pre and post-pulse of 2π. The certain position of the control pulse within the regime of dephasing or rephasing does not impact the echo temporal position, which is seen in the comparison of the Figs. 4.8(c) and (d), where the 2π post-pulse arrives at the different moments during rephasing. The shift of the 2PE by 5 ps is quite sufficient, while its field has a duration of 3.8 ps.

In Fig. 4.9 the two-dimensional plot shows 2PE temporal profiles at the different pulse areas $\theta_1 \propto \sqrt{I_1}$. The top row of the figures corresponds to the experimental data, while the bottom one to the numerical simulations. The simulation of $|E_{2PE}|$ is based on the numerical solution of the extended optical Bloch equation [Pol+17; AE75], the conventional form of the equations is shown here in Sec. 2.12. The main assumptions are the inhomogeneous broadening of the ensemble and a two-dimensional Gaussian distribution of the power at the spot on the sample, which is already enough to reach quite a good similarity between the experiment and the simulation. Since the manuscript is mostly dedicated to the experimental rather than theoretical part of the work. The numerical methods are described in the work [Kos+20].

The effect of freezing is supposed to be independent of the 2PE since it slows down the linear rise of the oscillator's phase. We modified the first pulse area to see if it changes the freezing, recording the temporal profiles. In Fig. 4.9 (a-c) the temporal profiles were measured at the double delay $\tau_{12} = 80$ ps, $\theta_2 \approx \pi$ and the control pulse $\theta_C \approx 2\pi$. The certain structure of the dependence was discussed in the subsection above, here we do not focus on it. The vertical dashed lines emphasize the $2\tau_{12}$ to track the change. The control pulse application leads to a shift of the picture as a whole and a minor change in its structure. The effects of the first pulse and the control pulse are additive since they modify the linear rise of phase at different moments. So, advanced 2PE when $\theta_1 = 3\pi/2$ can be additionally shifted by 2π pre-pulse and the total shift reaches 8 ps. Nevertheless, both the high area of the first pulse and the control pulse leads to the damping of the 2PE signal because of the excitation inhomogeneity and interaction with phonons.

The results of the simulations are shown in Fig. 4.9(e-g), their shape is close to the ones we observe in the experiment. The first two oscillations match well enough, but for the pulse areas $\theta_1 > 3\pi/2$ the experiment shows a sufficiently lower 2PE amplitude rather than the simulation. The deviation between amplitudes of the experiment and simulations occurs since we used a simplified model that takes into account only inhomogeneous excitation. The simulation also predicts some small changes in the 2PE temporal profiles, which are slightly different for the pre- and post-pulse action, which are not recognizable in the experimental data.

For the simplest comparison, we consider the 2PE temporal profiles corresponding to $\theta_1 = \pi/2$ and $3\pi/2$, which are shown in the Figs. 4.9(d) and (h) respectively. Solid lines here correspond to the simulation, while signs to the experiment. Amplitudes of the simulation are normalized to match the 2PE peak at $\theta_1 = \pi/2$ in absence of the control pulse. Blue lines and signs in both the figures match very well, when $\theta_1 = \pi/2$ the FWHM and its temporal positions almost coincide. As for $\theta_1 = 3\pi/2$, the 2PE

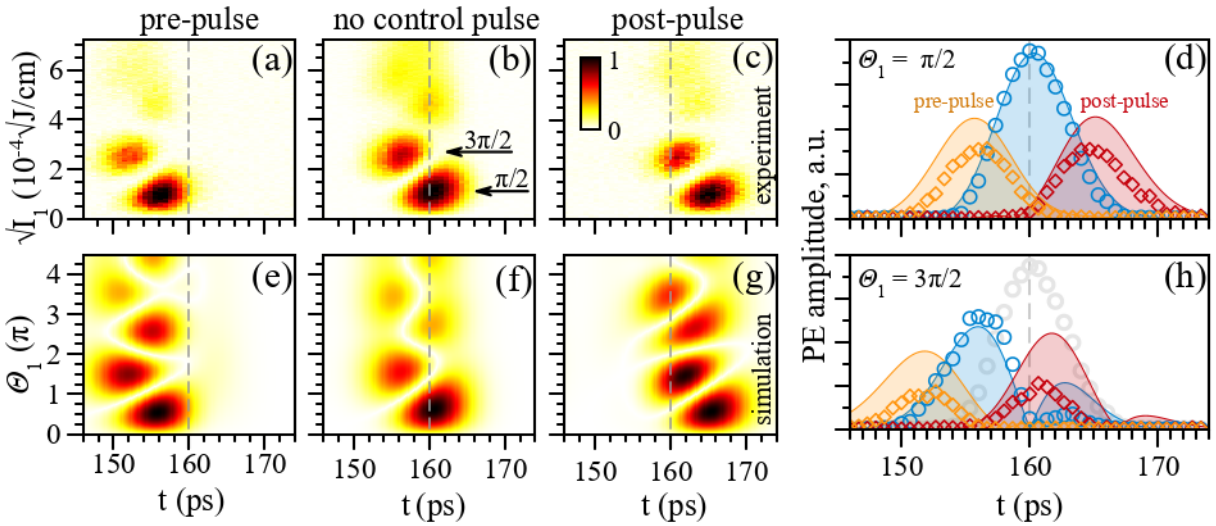

Figure 4.9: *Two-dimensional plots showing the dependence of the 2PE temporal profiles (x-axis) on the amplitude of the first pulse. (a,e) in presence of the 2π pre-pulse; (b,f) without a control pulse; (c,g) in presence of the 2π post-pulse. The top row (a-c) shows the experimental data, the bottom row shows the results of simulations. The temporal profiles from the (a-c) and (e-f) at the $\theta_1 = \pi/2$ are shown in (d); at the $\theta_1 = 3\pi/2$ are shown in (h). Here the blue line and signs correspond to the 2PE profiles without control pulse, yellow and red to the pre- and post-pulse correspondingly. For all the cases $\theta_2 \approx \pi$ and τ_{12} 80 ps.*

temporal profile is split into two parts: one corresponds to the advanced 2PE being in the range of 150-160 ps, and an afterglow of the $\pi/2$ 2PE which remains in the range of 160-170 ps. The shape of the main maximum (150-160 ps) matches the experiment, but the latter has 10% lower amplitude in comparison to the simulation. Meanwhile, the afterglow we see in the simulations is almost not seen in the experiment being 70 % lower than in the simulation.

2PE temporal profiles under the control pulse impact are represented by orange and red curves and signs in Fig. 4.9(d). First, let us look at the peaks corresponding to $\theta_1 = \pi/2$. Both, the experiment and simulations, have bell-curve shapes. The simulation predicts approximately 30 % bigger 2PE amplitudes, and also a slightly bigger temporal shift. A worse match of the experiment and simulation one sees when $\theta_1 = 3\pi/2$ on Fig. 4.9(h). The simulation predicts up to 60% higher amplitude of the signal, but the temporal position matches well. Thus, the model describes well the temporal profiles of 2PE but the experimental data has sufficiently lower amplitudes when the applied pulses have an area of more than $\approx \pi$.

Fig. 4.10 shows 2D plots of the 2PE temporal profiles at the different control pulse areas $\theta_C \propto \sqrt{I_1}$. Panels (a) and (b) show the experimentally measured pre- or post-pulse scan, while the (c) and (d) show us simulations. The pre-pulse was delayed from

the first pulse by 27 ps, while the post-pulse was by 27 ps from the second pulse. Such delays were chosen to avoid an appearance of 2PE generated by the first and control pulse sequence or 3PE at the $2\tau_{12}$.

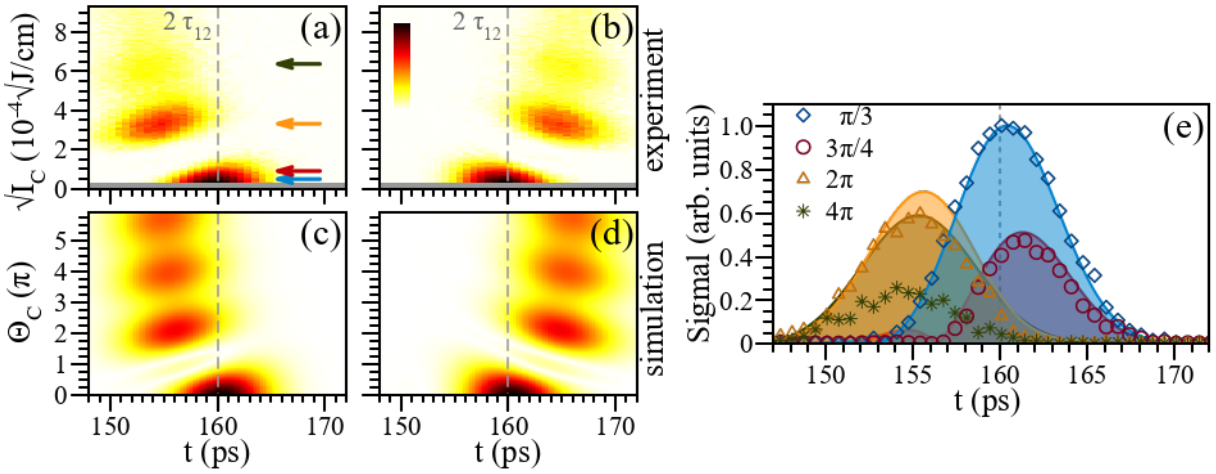

Figure 4.10: *Two-dimensional plots showing the dependence of the 2PE temporal profiles (x-axis) on the amplitude of the control pulse area $\propto \sqrt{I_C}$. (a&c) correspond to the pre-pulse; (b&d) correspond to post-pulse. The upper row shows us the experimental data and the downer row shows the numerical simulations. Temporal profiles at the control pulse area of $\pi/3, 3\pi/4, 2\pi$ and 4π are shown in the (e). The lines represent the numerical simulations, while the dots correspond to the experimental data. Here $\theta_1 \approx \pi/2$, $\theta_2 \approx \pi$ and $\tau_{12} = 80$ ps.*

The dependencies of 2PE on the pre- and post-pulse areas are mirrored relatively to the $2\tau_{12}$, so we describe here the only dependence on pre-pulse, shown in Fig. 4.10(a). The signal depends on the control pulse area as $\cos\theta_C$, having well pronounced maximums at 0, 2π and 4π or $\sqrt{I_C} = 0$, 3×10^{-4} and 6×10^{-4} $J^{1/2}$/cm. So, the maximums occur exactly when the freezing takes place i.e. when TLS does a full turn on the Bloch sphere.

When the area of the control pulse is low, the 2PE appears at around 160 ps. The rise of the control pulse area up to $\approx \pi/2$ reduces the 2PE amplitude. The reduction is not uniform, bigger at the lower times, so effectively a maximum of the 2PE temporal profile shifts towards the longer times while its FWHM reduces. The peak corresponding to the 2π appears 5 ps advanced, its amplitude is roughly 40 % lower in comparison with the low area. The maximum corresponding to 4π has twice the lower amplitude and is already 5.5 ps advanced. The following peak is very poor pronounced, but it continues the trend to drop the amplitude and be slightly more advanced than the previous ones. So, the temporal shifts slowly rise with the increase of control pulse area, but rapidly saturates and the difference between 4π and 6π is already barely distinguishable. The decay of the 2PE maximum amplitudes can be approximated by an

exponential decay by $\exp(-\sqrt{I_C/I_0})$ with $\sqrt{I_0} = 2 \times 10^{-4}$ J$^{1/2}$/cm. The simulations shown in Fig. 4.10(b,c) demonstrate qualitatively the same behaviour as the experiment and properly predict the 2PE timing. Nevertheless, the experimentally observed 2PE decays with the control pulse power sufficiently faster than the simulation predicts.

As above, we do temporal slices of 2D plots to compare the shapes directly. The amplitudes of simulation are normalized to match when $\theta_C = \pi/3$. We choose four $\theta_C = \pi/3$, $3\pi/4$, 2π and 4π, which are assigned on the Fig. 4.10(a) by arrows. They are plotted in Fig. 4.10(e) by the blue rhombuses, red circles, yellow triangles, and green asterisks correspondingly. The simulations are shown here by the lines of the corresponding colour. In all four cases, the temporal profiles have a shape close to the bell-like curve. Their central positions and FWHM match in the simulation and the experiment. At the $\pi/3$ the 2PE peak is almost centred at the $2\tau_{12}$, but is already slightly shifted to an advanced direction, its FWHM is about 7 ps. The simulation excellently matches the experimental data, their amplitudes are set to the unit because of normalization. So we consider the amplitude of $\pi/3$ as a reference. The $3\pi/4$ peak shifts to the longer times by roughly 1.5 ps, FWHM is 5.5 ps and the amplitude is twice lower than the reference. The simulation perfectly describes the experiment. When the control pulse has an area of 2π the echo is 5 ps advanced, its FWHM is again the same as $\pi/3$ case being 7 ps, and its amplitude is roughly 40 % lower than the reference. The simulation predicts roughly the same 2PE timing, but only a 30 % drop in the amplitude relative to the reference. At the 4π the temporal profile 5.5 ps advanced, but the FWHM remains the same as before. The experimental amplitude is about 75 % lower in comparison to the reference, while the simulation predicts a reduction down to 40 %. Thus, here we see the two regimes of the control pulse action: in the range up to $\theta_C < \pi$, it leads to a reduction of the 2PE amplitude and a simultaneous slight shift to the longer times; and the regime of $\theta_C < 2\pi n$ (where $n \in \mathbb{N}$), where the 2PE appears advanced. It is known that intensity-dependent damping of the Rabi oscillations can also arise from the coupling to acoustic phonons as demonstrated for spatially homogeneous systems [Kr05; Mon+13], that was directly confirmed in work [Gri+22]. Nevertheless, here we use a simplified model considering the homogeneity as a dominant mechanism responsible for the Rabi oscillations damping.

We note that intense off-resonant control pulses can be used to influence the dephasing of excitons in QD ensembles. In this case, the ac Stark effect may lead to modulations of the PE amplitude as recently demonstrated in rare earth solids [CH15; Ham17; Bar+18]. This behaviour has also been confirmed within our model where we find, that the temporal shift of the PE decreases in presence of a detuning, for which also the PE amplitude rapidly reduces with increasing intensity of the control pulse.

4.5 Conclusions

Thus, we have shown in the chapter, that the method to vary the 2PE formation moment in both directions in a deterministic way, applying a control pulse during dephasing or rephasing. It happens when a resonantly tuned control pulse with an area of $2\pi n$ is applied (where $n \in \mathbb{N}$). The freezing effect does not also depend on the exact areas and wavevectors of the two pulses forming 2PE. The certain magnitude of the temporal shift is defined by the duration of the control pulse. The 2PE does not experience strong variations of its temporal shape under appropriate conditions, which correspond to a strong driving optical field. The accuracy of the 2PE timing in the variations is determined by the duration of the control pulse, its intensity and its shape.

The method might be applied to control the 2PE timing on the ultrafast timescales and implemented, for example in the memory protocols [Lvo+09; Tit+10; Pol+16]. Furthermore, addressing the spin degrees of freedom in systems with more than two energy levels (V- and Λ-type arrangements) can be used to split the temporal profile of PEs into two counter-polarized pulses making it possible to perform wave-function interferometry of electronic excitations in solid state systems. The method might be non only used to control the 2PE timing with all the possible applications, but also has a fundamental value since establishes a way to temporarily freeze an unavoidable dephasing of the inhomogeneously broadened ensemble of TLSs.

Chapter 5

Microscopic dynamics of electron hopping in a semiconductor quantum well CdTe

Quantum technologies require control of the quantum system evolution [Pre+08]. It is advantageous to accompany such the control by long-term storage of the optical coherence, both of them encourage the development of quantum technologies. The storage of the coherence into the resident electron spin allows one to keep it for nanoseconds overcoming a limitation of the optical recombination time [Lan+14]. The corresponding mechanisms of the optical coherence storage and retrieval via the excitonic complexes were overviewed in Sec. 2.4.4. Once the coherence is stored in the resident electron spin, it decays already by the spin relaxation mechanism.

In this chapter, we analyze the resident electron dynamics and the spin relaxation mechanisms by a complex method including the long-lived three-pulse photon echo (3PE) and the time-resolved Kerr rotation (KR). Such a complex technique allowed us all optically access the microscopic dynamics of the resident electron and measure its localization time τ_L between hops.

5.1 Formation of the Kerr rotation and long-lived 3PE signals

The spin dynamics of the photoexcited or resident carriers can be observed using the time-resolved Kerr rotation (KR) [DK11; Aws+02], (which is overviewed here in Sec. 2.3.1) or long-lived three-pulse photon echo (3PE) [Lan+14; Sal+17b] (which is overviewed here in Sec. 2.4.4). Briefly, the Kerr rotation measures the macroscopic spin polarization being an average over the ensemble of spins, while the spin polarization is introduced by the circularly polarized pump-pulse. It forms a spin polarization along light wavevector $\vec{k} \parallel z$, which is perpendicular to the sample's plane. The applied in-plane magnetic field ($B||x$) causes rotation of the spins in the yz-plane with the Larmor frequency $\omega_{\mathrm{L}} = g_{\mathrm{e}}\mu_{\mathrm{B}}B/\hbar$, where g_{e} is the electron g-factor, μ_{B} is the Bohr magneton, and $\hbar$ is the reduced Planck constant. When a linearly polarized probe-pulse reflects from the sample, it obtains some chirality due to the Kerr effect [Gla12]. We call the signal Kerr rotation referring to the more general case and to keep it consistent with the previous works, while here we measure the ellipticity. Nevertheless, the choice between ellipticity and rotation is mostly defined by the signal intensity in the particular case and both correctly reflect the spin polarization. Variation of the delay between the pump and probe pulses allows one to measure the dynamics of the spin polarization $S_z(t)$ evolution. It consists of the oscillation in the magnetic field and decay with the spin relaxation time $T^*_{2,\mathrm{KR}}$ as $S_z(t) \propto \cos(\omega_{\mathrm{L}}t)\exp(-t/T^*_{2,\mathrm{KR}})$

Meanwhile, the long-lived 3PE technique implies temporary storage of the optical coherence in the resident electron and heavy hole (in case of X^-), with subsequent recovery and formation of the echo signal. Behaviour of the 3PE as a dependence on τ_{23} using HVVH polarization protocol in the magnetic field represent the similar to time-resolved Kerr rotation dynamics of the resident electron spins. So, such PEs can be used as an effective tool for the coherent observation of the spin dynamics [Tri+21]. The PE formation is based on a sequential dephasing and rephasing of the ensemble, which gives access to a homogeneous linewidth of the optical transition avoiding an impact of the inhomogeneous broadening [Har68]. That gives the long-lived 3PE an exceptionally high sensitivity to spectral diffusion, e.g. due to energy relaxation or resonance frequency variation [Web+91]. Nevertheless, the technique was not yet applied to a study of the resident carrier dynamics.

Despite both KR and long-lived 3PE allowing one to track spin dynamics, the signal formation mechanisms sufficiently differ. As was shown in Sec. 2.4.4, long-lived 3PE is based on the coherent response of the fringe created by a sequence of cross-polarized HV pulses with a delay τ_{12} between them. The period of the fringe depends on the

mean excitonic resonance frequency Ω_0 and the delay time τ_{12} between the pulses. The created spin grating in coordinate and frequency space is shaped as:

$$S_y^0 - \mathrm{i}S_z^0 \propto \mathrm{i}\exp\left(\frac{\mathrm{i}\omega_L\tau_{12}}{2}\right)\cos\left(\Omega_0\tau_{12} + \vec{k}_{2,\parallel}\vec{r} - \vec{k}_{1,\parallel}\vec{r}\right), \tag{5.1}$$

where $\vec{k}_{1,\parallel}$ and $\vec{k}_{2,\parallel}$ are in-plane components of the wavevectors. In presence of the in-plane magnetic field ($B||x$), the fringe rotates with Larmor frequency ω_L and decays with a spin relaxation time $T^*_{2,\mathrm{PE}}$. Here we must keep in mind that in general $T^*_{2,\mathrm{KR}} \neq T^*_{2,\mathrm{PE}}$, which is a key point of the current chapter.

Application of the third coherent pulse to the fringe initiates a coherent response, appearing τ_{12} after its action. Here we surely imply the fulfilment of the FWM formation condition [Sha99] described in Eqs. 2.23. Variation of the delay between the sequence of two cross-polarized pulses and the third one τ_{23} when τ_{12} is constant, allows one to see the temporal evolution of the fringe. The measured signal, in that case, is proportional to the projection of the current spin-grating state on the initial one, so:

$$E_{\mathrm{HVVH}}(\tau_{23}) \propto \left[S_\mathrm{y}(\tau_{23}) - \mathrm{i}S_\mathrm{z}(\tau_{23})\right] \cdot \left[S^0_\mathrm{y} + \mathrm{i}S^0_\mathrm{y}\right] \tag{5.2}$$

The typical signal behaves as $E_{\mathrm{HVVH}}(\tau_{23}) \propto \cos(\omega_\mathrm{L}\tau_{23} + \phi)\exp(-\tau_{23}/T^*_{2,\mathrm{PE}})$. ϕ is introduced to the expression in the work [Kos+22] and represents the contribution of the heavy hole precession between the first two pulses' arrival. Since the setup we used is insensitive to the phase of the light, we measure only an absolute value of its amplitude [Pol+18] and can not see signs of the oscillations. In contrast to the established transient spin grating technique [Kor+09; Car+06], where $\tau_{12} \approx 0$, the long-lived 3PE appears when $\Delta\Omega_0\tau_{12} \gg \pi$ with $\Delta\Omega_0$ being the spectral width of the optical transitions. From that, we can conclude that the PE signal is quite sensitive to spectral diffusion of the resident electrons, which takes place if the carriers hop between the localization sites.

5.2 Photon echo from the trions and donor-bound excitons

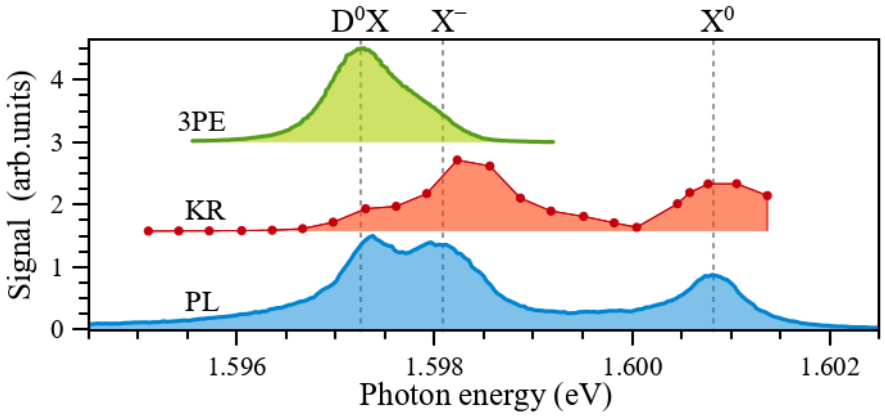

Figure 5.1: *Spectral dependence of the photoluminescence intensity (blue line). The amplitudes of long-lived 3PE (green line) and KR signals (red dots). Both are measured at $B = 0.25$ T at temporal delays sufficiently bigger than T_2. All the measurements were done at $T = 2$ K*

The experiment was performed on the 20 nm-thick CdTe single QW, a comprehensive description of the sample can be found in Sec. 3.1.2. The spectrum of the photoluminescence (PL) is shown in Fig. 5.1 by the blue solid line. The three maxima are attributed to the neutral exciton X^0 at photon energy 1.6008 eV, donor-bound exciton D^0X at 1.5972 eV, and negatively charged exciton (trion) X^- at 1.5981 eV. Here we focus our attention on the D^0X and X^-, which include the resident electrons and allow us to establish interaction with them optically. The resident electrons in this sample appear because of the background impurities.

In Fig. 5.1 we also show KR and long-lived 3PE amplitude spectral dependencies, which were measured at delays exceeding optical T_2 to see only the long-lived components associated with the resident electrons. The spectral dependences of the signal amplitudes of the KR and long-lived 3PE dynamics are shown by red dots and the green line respectively. The long-lived 3PE signal is well seen only from the D^0X and X^- since the neutral exciton does not allow storing the coherence longer than its T_2. Nevertheless, the KR shows us a signal from all three spectral features including X^0. Even in a degenerate time-resolved KR experiment, the excitation and detection of spin polarization may involve different optical transitions which allows us to see the long-lived signal on the X^0 resonance. We do not analyze the spectra shapes and do not compare them since their certain shape depends on many parameters of the particular experiment and are convolutions with the laser spectral width. Nevertheless, we point

out that the spectral positions of the exciton complexes are the same for all methods. The long-lived 3PE shows us the maximal amplitude of the signal from D^0X, while KR from X^-.

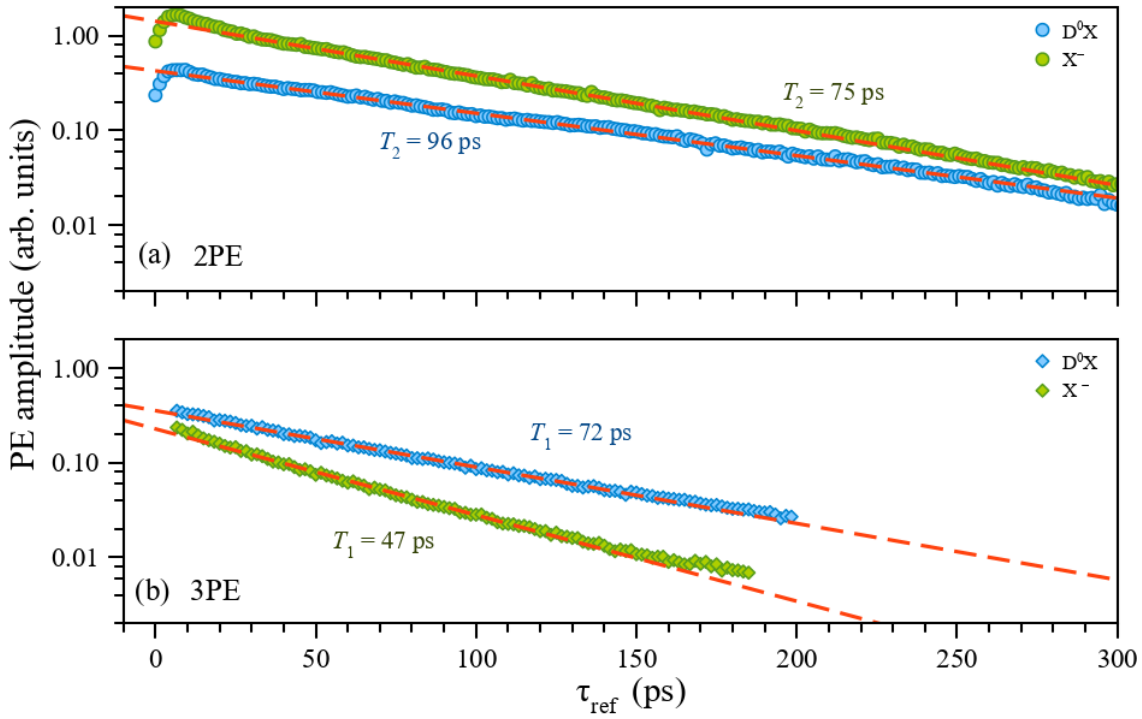

Figure 5.2: *(a) 2PE decays and (b) 3PE decays measured from the D^0X and X^- resonances in co-polarized polarization protocols HHH and HHHH respectively. We kept the temperature of about 2 K.*

Before access to the resident carriers via long-lived 3PE we measure the optical T_1 and T_2 of the X^- and D^0X resonances. In Fig. 5.2 are shown 2PE and 3PE decays, they were measured using co-polarized polarization protocols HHH and HHHH. The blue signs correspond to the spectrally selected D^0X at 1.5972 eV, and the green ones to the X^- at 1.5980 eV. The red dashed lines represent the corresponding fits. All four decays are single-exponential. Fig. 5.2 (a) shows 2PE decays, from fits we extract $T_2 = 96$ ps for the D^0X and $T_2 = 75$ ps for the X^-. The 2PE from X^- has a bigger amplitude and shorter decay time, so we expect its higher oscillator strength. Fig. 5.2 (b) shows 3PE decays, their fits give us $T_1 = 72$ ps for the D^0X and $T_2 = 47$ ps for the X^-. In both cases, $T_2 < 2T_1$, which means the T_2 is defined not only by radiative recombination but also by another decoherence mechanism. The pulse areas were chosen to be sufficiently smaller than π in order to reduce excitation-induced dephasing or other laser-driven decoherence processes.

5.2.1 Long-lived signal in the magnetic field

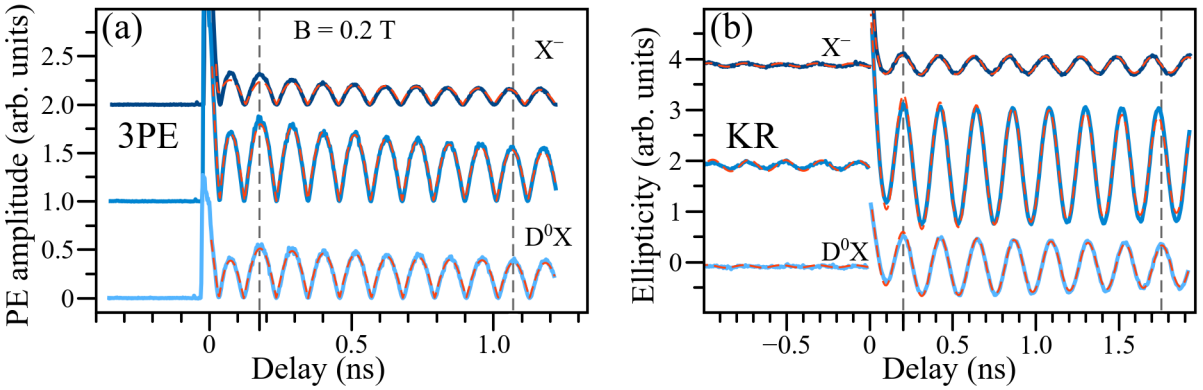

Figure 5.3: *Examples of the long-lived 3PE and time-resolved KR transients measured at $T = 1.5$ K in the magnetic field of $B = 0.2$ T laying in-plane of the sample. The curves placed at the top correspond to the X^- resonance, at the bottom to the D^0X and at the middle corresponds to the intermediate photon energy. (a) 3PE transients measured with the constant $\tau_{12} = 26.7$ ps using HVVH polarization protocol; (b) the KR transients. Dashed curves show fits using Expr. 5.3. At the D^0X both 3PE and KR decay with the $T^*_{2,\mathrm{PE}}$ and $T^*_{2,\mathrm{KR}} \approx 4$ ns, while for the X^- case the 3PE shows us $T^*_{2,\mathrm{PE}} = 3$ ns and KR has $T^*_{2,\mathrm{KR}} = 5$ ns*

We measured the signals of time-resolved KR and long-lived 3PE in the magnetic field of 0.2 T, in the different spectral resonances corresponding to D^0X at 1.5971 eV, X^- at 1.5984 eV resonances and in between them at 1.5978 eV according to Fig. 5.1. The signals represent the dynamics of the resident electrons localized on donor atoms as in the case of D^0X or potential fluctuations in the case of X^-. In Fig. 5.3, the panel (a) corresponds to the 3PE and (b) to the KR signals. The signals observed in both techniques arise from the resident electron spin polarization, they oscillate and decay in time. Nevertheless, in the present signal, we also see a rapid decay within the first ≈ 0.2 ns. It corresponds to the perturbation of the electronic system and decays with approximately T_2. Thus, all the signals can be fit well by the function:

$$A \exp(-t/T^*_{2,\mathrm{e}}) \sin(\omega_L t + \varphi) + B \exp(-t/\tau), \tag{5.3}$$

where τ corresponds to the perturbations of the optical transition. Here we highlight that we measure only the absolute value of the 3PE i.e. $|E_{3\mathrm{PE}}|$, since the setup is not sensitive to its phase. The red dashed lines in Fig. 5.3 represent the fits by Expr. 5.3. In the case of the KR, the fits were done using the signal from the negative delays, while the 3PE signal amplitude was always zero in the negative time range.

The spectral dependence of the oscillation frequencies is seen in both methods. At the D^0X resonance, both techniques show oscillations with frequencies of about

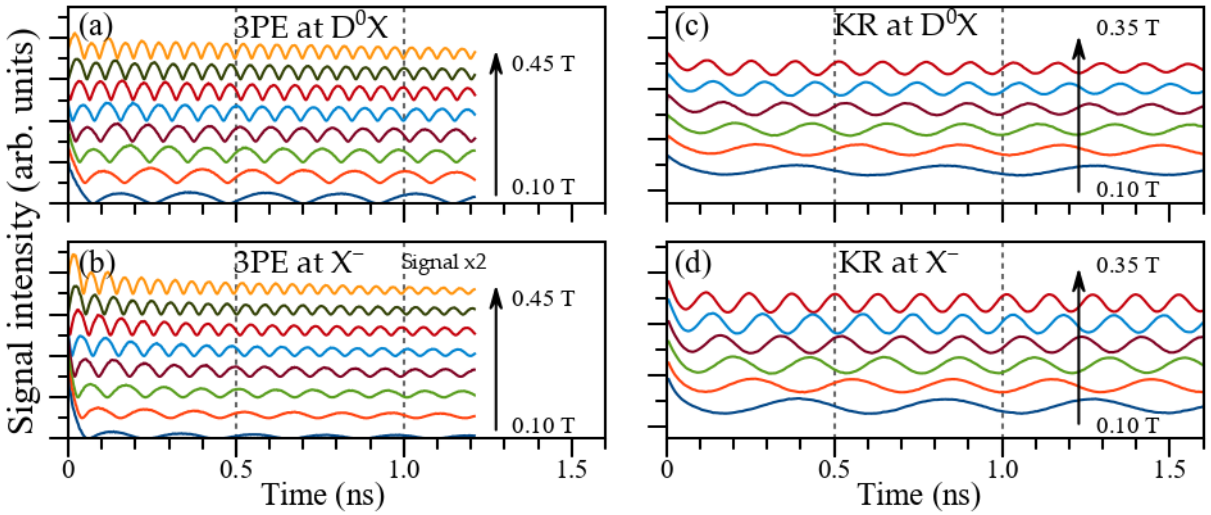

Figure 5.4: *The long-lived 3PE and time-resolved KR transients measured as a dependence of the magnetic field at $T = 2$ K. The 3PE was measured with $\tau_{12} = 26.7$ ps using the HVVH polarization protocol. (a) 3PE measured at D^0X resonant excitation; (b) 3PE measured X^- resonant excitation; (c) KR measured at D^0X resonant excitation; (d) KR measured at X^- resonant excitation.*

28.2 rad/ns, while at X^- they have a few percent higher frequencies. We will discuss that below in more detail. Here we would only like to point out that the difference in ω_L is clearly seen in the transients even visually on the waterfall plots, see the phases of oscillations on the dashed vertical lines.

From the curves in Fig. 5.3, we also can extract their decay times, which represent the spin relaxation time. Both the techniques show the same decay time for D^0X, giving us $T^*_{2,KR} = T^*_{2,PE} \approx 4$ ns. But for the X^- decay times are different, the KR shows decay time of $T^*_{2,KR} = 5$ ns, while 3PE transient decays with $T^*_{2,PE} = 3$ ns. The intermediate spectral point also shows us different decay times, which are close enough to the observed at X^-. Thus, there are two important conclusions from Fig. 5.3: (1) both the techniques show, that the g-factor of the resident electrons accessed via X^- is higher than ones accessed via D^0X; (2) the KR and long-lived 3PE show us the same spin relaxation time at the deeper localized D^0X, while at the X^- the long-lived 3PE gives roughly twice shorter spin relaxation time compared to KR.

Despite in Fig. 5.3 we clearly see the difference in g-factors of the resident electrons accessed via D^0X and X^-, we do not extract their g-factros here. The high precision g-factor values can be extracted from the $\omega_L(B)$ dependence, which requires numerous transients measured at the different magnetic fields. In the four panels of Fig. 5.4 we show such sets, they are measured at D^0X and X^- by 3PE and KR techniques. The

curves are waterfalled from the maximal magnetic field of 0.45 T for 3PE and 0.35 T for KR down to 0.1 T with a step of 0.05 T. The curves which were measured in the same magnetic fields are samely coloured. The dynamics shown here are similar to the ones we saw in Fig. 5.3. We only point out, that the dynamics measured in the higher magnetic fields show us a faster decay time. Such a dependence indicates us that we observe the inhomogeneous spin relaxation time $T_{2,\mathrm{e}}^{*}$ which depends on the magnetic field concerning Expr. 2.4. First, we analyze the Larmor frequency dependence on the magnetic field, then we come back to the spin relaxation time analysis.

In Fig. 5.4 we clearly see, that the signal corresponding to X^{-} is always slightly faster oscillating compared to $D^{0}X$. We have summarized the presented data in the four $\omega_{\mathrm{L}}(B)$ dependencies in Fig. 5.5. The blue circles correspond to the X^{-}, and the red rhombuses to the $D^{0}X$. The full signs to the long-lived 3PE, and the open to the KR. We clearly see a clusterization of the blue and red signs, corresponding to the electrons of different g-factors. A linear fit by a function $\omega_{\mathrm{L}} = \mu_{\mathrm{B}} g B/\hbar$ are shown by dashed lines of corresponding colours. As one can see, independently of the technique the fitting curves show the same slopes of the X^{-} and $D^{0}X$, which give us g-factors of $|g_{\mathrm{e}}| = 1.60$, $|g_{\mathrm{e}}| = 1.57$ respectively. The values are in good agreement with the previous reports [Sal+17b; Zhu+07; Sae+18]. It is known that the g-factor values are negative [Sir+97].

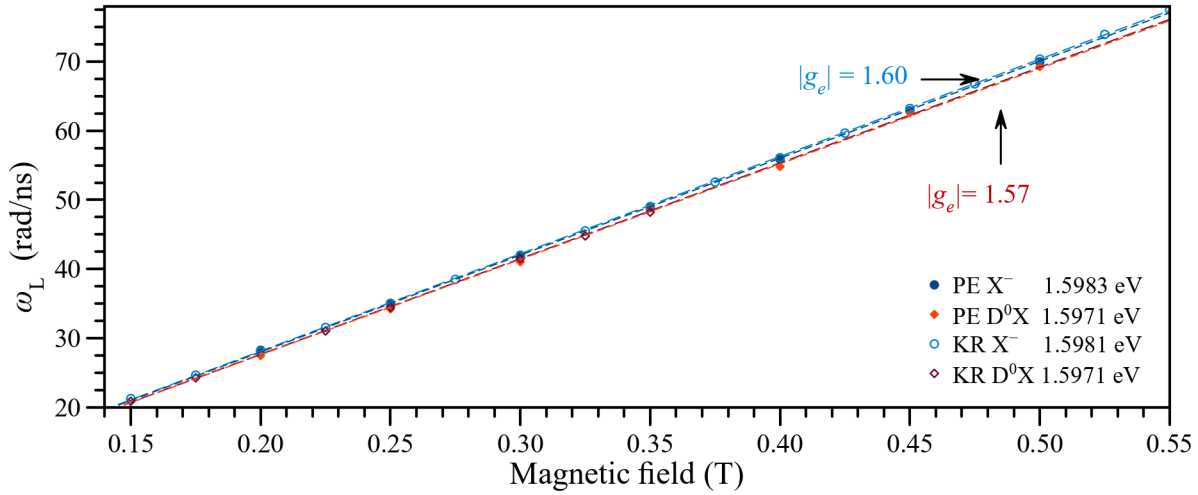

Figure 5.5: *Dependence of the Larmor frequency on the magnetic field, measured by the 3PE (filled symbols) and KR (open symbols) techniques under the resonant excitation of the X^{-} (circles) and $D^{0}X$. Dashed lines represent fits by $\omega_{\mathrm{L}} = \mu_{\mathrm{B}} g B/\hbar$*

In the inhomogeneously broadened ensembles placed in the transverse magnetic fields, spin relaxation can occur because of the dispersion of the Larmor frequencies over the ensemble. Supposing a homogeneous magnetic field in the area we probe (we

suppose the beam diameter below $\approx 500\mu$m) the magnetization, we relay the inhomogeneity to the spread of electron g-factor Δg_e [Zhu+07]. According to the Eq. 2.4, we define the inhomogeneous spin relaxation time $T^*_{2,\mathrm{e}}$ as:

$$1/T^*_{2,e}(B) = 1/T_{2,e} + \Delta g_\mathrm{e}\mu_\mathrm{B}B/\hbar. \tag{5.4}$$

Here the first term represents the microscopic spin relaxation and the second term represents the relaxation of the macroscopic spin because of the ensemble inhomogeneity.

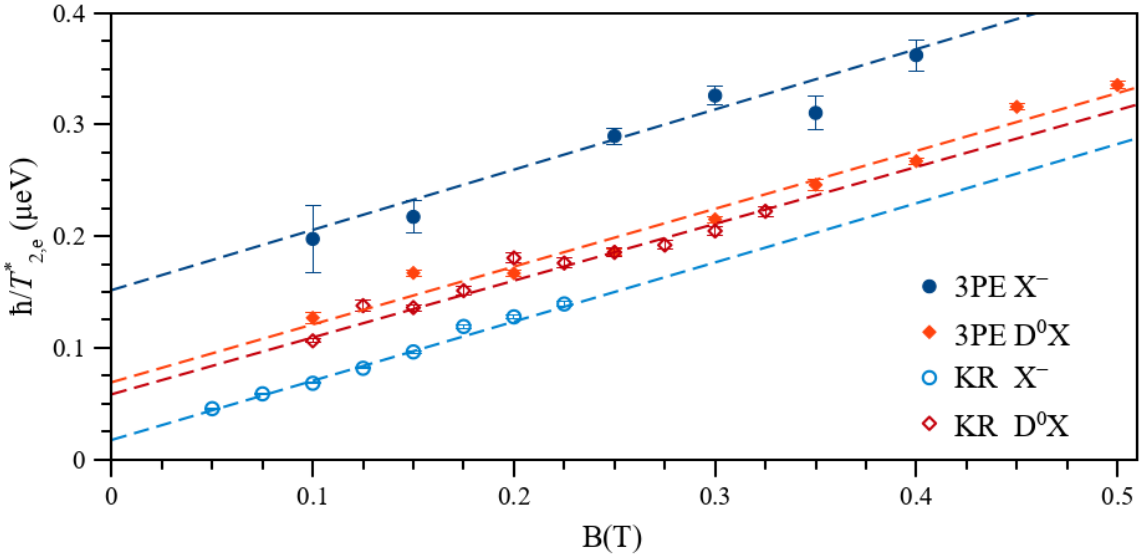

Figure 5.6: *Magnetic field dependence of relaxation rate $\hbar/T^*_{2,e}$ for X^- and D^0X obtained from the KR and PE signals. $T = 1.5$ K, $\tau_{12} = 26.7$ ps. Results are fitted using Expr. 5.4 (dashed lines) with the same $\Delta g_e = 9 \times 10^{-3}$ for all the curves. The X^- gives us $T_{2,\mathrm{KR}} \gtrsim 20$ ns, and $T_{2,\mathrm{PE}} \approx 4$ ns, while D^0X gives us $T_{2,\mathrm{KR}} \approx T_{2,\mathrm{PE}} \approx 10$ ns.*

From the data shown in Fig. 5.4, we have extracted the spin relaxation rates $1/T^*_{2,\mathrm{e}}(B)$ and summarized them in the Fig. 5.6. Here the blue circles correspond to X^- and red rhombuses to D^0X. Full signs to the long-lived 3PE and open to KR. Fits by the linear function according to Eq. 2.4 are shown by dashed lines of corresponding colours. First, the slopes of all the curves are the same. It means in both X^- and D^0X, the inhomogeneity is the same and has a value of $\Delta g_e = 9 \times 10^{-3}$. That proves that the signal originates from the same sub-ensembles of the resident electrons. The only difference between the dashed lines is an intersection, which is defined by the homogeneous spin relaxation time $T_{2,\mathrm{e}}$. As for D^0X, the homogeneous times are roughly the same and $T_{2,\mathrm{KR}} \approx T_{2,\mathrm{PE}} \approx 10$ ns. But for X^-, $T_{2,\mathrm{KR}} \gtrsim 20$ ns and $T_{2,\mathrm{PE}} \approx 4$ ns differ drastically .

In order to analyze the spectral dependencies $T^*_{2,\mathrm{e}}$ and g-factor we did a set of the

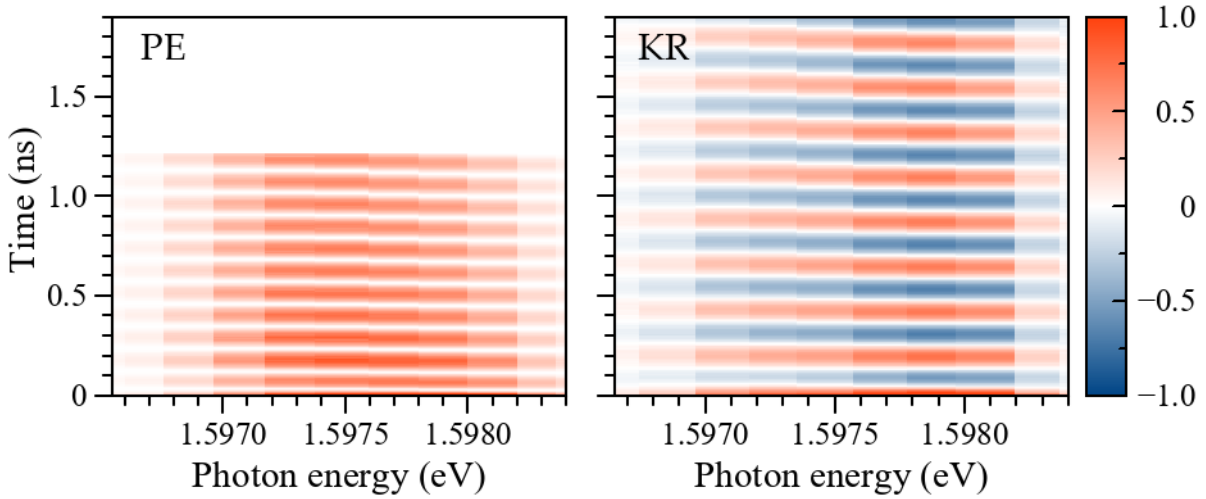

Figure 5.7: *Two-dimensional plot representing the long-lived 3PE and time-resolved KR transients spectral dependence, measured at $T = 2$ K. The 3PE amplitude was measured with $\tau_{12} = 26.7$ ps, and using HVVH polarization protocol. $B = 0.2$ T*

measurements of long-lived 3PE and KR in the magnetic field of 0.2 T in the different spectral points around D^0X and X^- resonances shown in Fig. 5.1. The data is presented in Fig. 5.7 as two-dimensional plots, where the x-axis corresponds to the spectral position, y- to the temporal evolution i.e. τ_{23} in case of 3PE and delay time Δt in case of KR. The colour represents the amplitude of the signal, here 3PE is unipolar while the KR is bipolar. Despite the different ranges of the measurement, we use the same scale of the time axis for easier comparison. As mentioned above, the long-lived 3PE has the maximal amplitude at D^0X, while KR has at X^-. It is clear from both plots, that the Larmor frequencies of the electron bound to the donor are lower as was shown above. Corresponding spectral dependencies will be analyzed below.

5.3 Impact of hopping on the observed spin relaxation times

Such a huge difference in the observed spin relaxation times measured by the two techniques is caused by the difference in the microscopic dynamics of resident electrons responsible for the signal formation. The resident electrons can hop between different localization sites changing their energy with the temperature within $\Delta E = k_B T$. The hopping can be characterized by the localization time τ_L or hopping rate τ_L^{-1}. Change of the resident electron localization sites makes the corresponding excitonic complex differently detuned from the ensemble average, i.e. an event of hopping changes Δ_i. Hence the excitonic complex after recovery of the optical coherence stored in the electron in frames of long-lived 3PE technique, can not contribute anymore to the 3PE signal. The impact of the hopping on the spin polarization or spin fringes is shown in Fig. 5.8(a). As seen in the left top figure, the hopping redistributes the electrons within the fringe $\left[S_y(\tau_{23}) - iS_z(\tau_{23})\right]$ that reduces its amplitudes and fades the contrast.

The case of the KR is shown in Fig. 5.8(b). When the ΔE is small compared to the

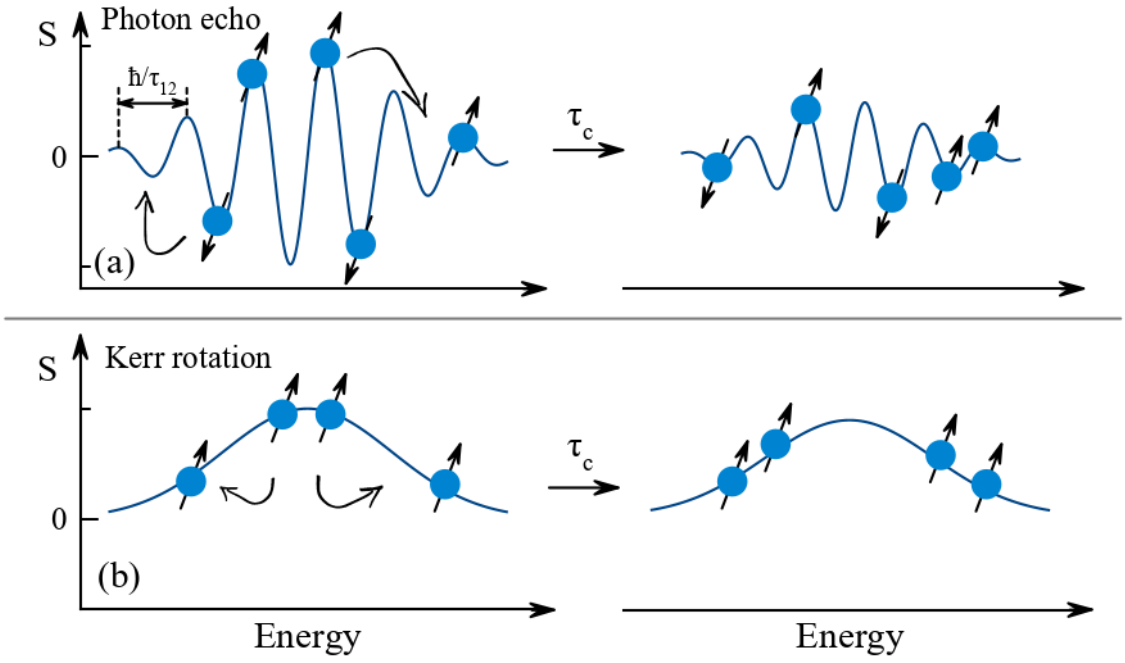

Figure 5.8: *Scheme of the energy distribution of spin density S of localized resident electrons in the KR (top) and PE (bottom) experiments before (left) and after (right) hopping between localization sites. A single hop is accompanied by a change of energy, while spin is conserved. Therefore, hopping destroys the spectral fringe but does not influence the macroscopic spin.*

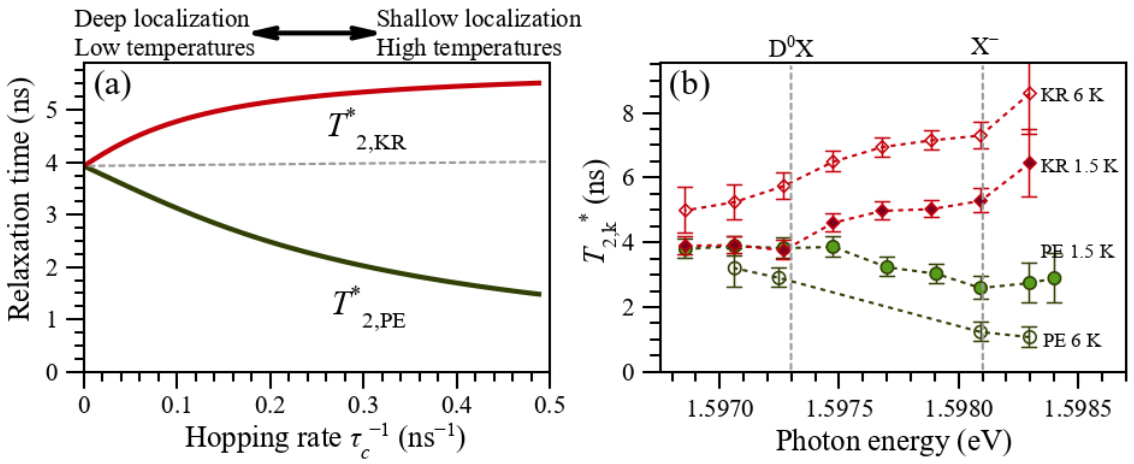

Figure 5.9: *(a) Visualised Expr. 5.5 of relaxation times $T^*_{2,k}$ on hopping rate τ_L^{-1} for $\delta_e = 0.1$ ns^{-1}, $\Delta g_e = 9 \times 10^{-3}$ and $B = 0.2$ T. (b) Spectral dependence of relaxation times $T^*_{2,k}$ measured at $T = 2$ and 6 K for $B = 0.2$ T.*

distribution width, hopping does not change its shape sufficiently. As we see from Fig. 5.3, the shallower localized resident electrons accessed via X$^-$, have longer relaxation time than deeper localized electrons accessed via D^{0}X. So we see that the hopping does not reduce the spin relaxation time, therefore we conclude the conservation of the spin during a sequence of hoppings and the hopping itself does not impact the spin of the resident electron. While the hopping leads to relatively small electron spacial displacement, the 3PE decay is mostly impacted by spectral diffusion. So, the hopping itself when ΔE is small enough does not reduce the S_z KR sensitive to.

In the QW we studied the main mechanism of the electron spin relaxation is a hyperfine coupling with the nuclear spins [Gla18; Mer+02]. When the field of the nuclear fluctuation $\sqrt{\langle\omega_N^2\rangle}$ is small, so $\sqrt{\langle\omega_N^2\rangle}\tau_L \leq 1$, the spin relaxation occurs in several hops and the spin relaxation time in the ensemble depends on the localization time $T_{2,KR}^{-1} \sim \langle\Omega_N^2\rangle\tau_L$ [Gla15; Kav08]. On the other hand, the long-lived 3PE decays with the $T_{2,PE} \sim \tau_L$ independently on the particular spin relaxation mechanism, since as soon the resident electron changes its localization site it can not contribute to the 3PE anymore. The microscopic theory based on the kinetic equations can be found in the Appendix of Ref. [Kos+19]. It defines $T_{2,KR}$ and $T_{2,PE}$ as functions of the τ_L and $\langle\Omega_N^2\rangle$ by the following way:

$$T_{2,KR} = \frac{2\exp[-1/(\delta_e\tau_L)^2]}{\sqrt{\pi}\delta_e \mathrm{erfc}[(\delta_e\tau_L)^{-1}]}, \quad T_{2,PE} = T_{2,KR} - \frac{2}{\delta_e^2\tau_L} \tag{5.5}$$

where $\delta_e^2 = 2\langle\Omega_N^2\rangle/3$ and $\mathrm{erfc}(x)$ being the error function. The spin relaxation times

observed by both methods according to the expression above are shown in Fig. 5.9(a), where they are plotted as a function of the hopping rate τ_c^{-1}. The $\delta_e = 0.1$ ns^{-1} value is defined from the experimental data being the only fitting parameter. The red line corresponds to KR and the green one to long-lived 3PE. At the zero hopping rate i.e. infinite localization time, we see at D^0X $T^*_{2,KR} = T^*_{2,PE} = 4$ ns. The $T^*_{2,KR}$ rises up to 5 ns at the hopping rate of 0.2 ns^{-1}, and then reaches 5.5 ns at 0.5 ns^{-1} having a tend to saturate. $T^*_{2,PE}$ gradually decreases having a value of 2.5 ns at hopping rate 0.2 ns^{-1}, and reaching 2 ns at the hopping rate of 0.5 ns^{-1}. That quantitatively matches the data presented in Fig. 5.3 and estimates the hopping rate as 0.2 ns^{-1} or localization time τ_L = 5 ns.

So, match of the $T^*_{2,KR} = T^*_{2,PE}$ in case of D^0X proves hopping suppression. D^0X has the lowest energy in the spectrum (see Fig. 5.1) and therefore has the deepest resident electron localization. As for the weaker localized X^-, its spin relaxation times measured by KR and long-lived 3PE differ. The model proposed in Eqs. 5.5 and Fig. 5.9(a) allows one to extract the localization time τ_L = 5 ns from a comparison of the experimental data and the analytical dependencies.

To prove the suggested model, we can accelerate the hopping rate and see how does the observed spin relaxation times behave. The hopping rate can be increased by a rise in the temperature. For that, we have measured the transients at the different spectral points corresponding to D^0X, X^- and around which were chosen by PE and KR spectra in Fig. 5.1. The measurements were done at the temperature of 1.5 K as usual (shown in Fig. 5.7) and at 6 K, which must increase the hopping rate. The spin relaxation times obtained by fitting the data are summarized in Fig. 5.9(b), where the circles and rhombuses correspond to 3PE and KR, and filled and open signs correspond to 1.5 and 6 K respectively. First, we see that the D^0X (1.5972 eV) at $T = 1.5$ K gives the same relaxation time of about 4 ns as was shown above. $\langle\Omega_N^2\rangle\tau_c^2 \gg 1$ regime occurs here due to the stronger localization of the electrons [Dzh+02; Mer+02], the electron loses its spin due to the hyperfine coupling which often takes place when the carrier is localized. Addressing the excitonic complexes by a certain laser photon energy we interact with the less localized resident electrons, and therefore the spin relaxation times $T^*_{2,KR}$ and $T^*_{2,PE}$ differ here. The same behaviour gives rise of the temperature, which proves our model and excludes the exchange interaction as a possible mechanism of spin relaxation. Thus, using the Expr. 5.5, we can extract the localization times from the data presented in Fig. 5.9(b). The electrons localized on the potential fluctuation and accessed via X^- have a localization time τ_L = 5 ns at the temperature of 1.5 K and τ_L = 2 ns at the temperature of 6 K. The carriers localized on the donor and accessed via D^0X at the temperature of 6 K are already not totally localized and show us a localization

time τ_L = 5 ns.

5.3.1 Comparison with the resonant spin amplification technique

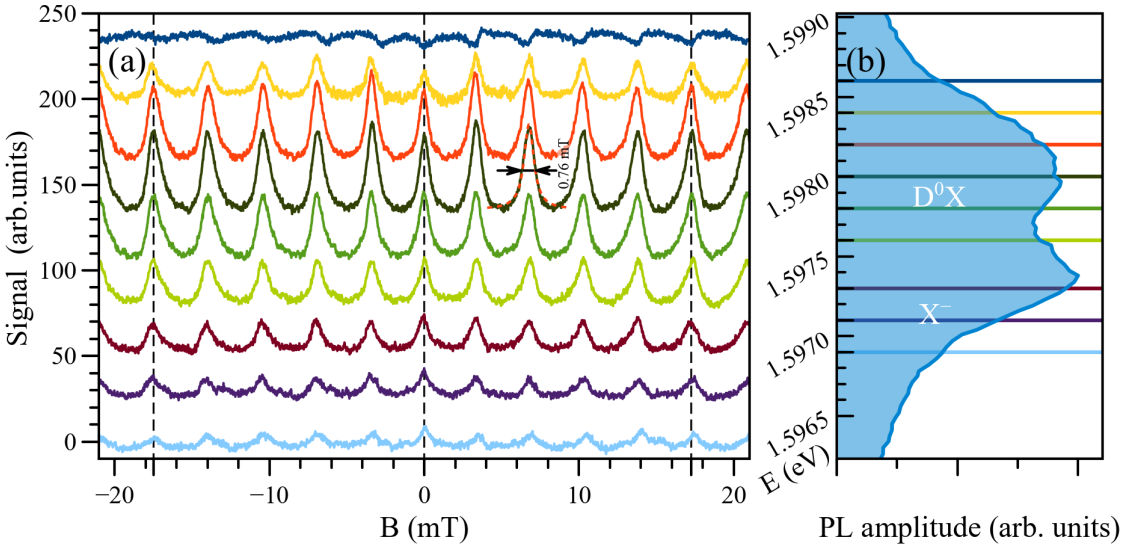

Figure 5.10: *(a) The RSA signals measured at the different photon energies. The probe was set* $\approx$ 10 *ps before the pump pulse. (b) the wavelength of the RSA curves are assigned on the PL spectrum by lines of the corresponding colours.*

We briefly remind that the resonant spin amplification (RSA) is a variation of the time-resolved Kerr rotation technique, where the probe pulse reads out a spin polarization of the long-lived resident electrons at large delays between the pump and probe or right before the pump pulse. When the Larmor frequency is commensurate with the laser pulse repetition frequency, the amplitude of the signal increases. Variation of the magnetic field gives us a set of peaks, which originates from the spins which perform an integer number of rotations in the magnetic field between two pump pulses. A more detailed description of the technique can be found in Sec. 2.3.1 or in Refs. [GI08; Gla12]. The important feature we have to keep in mind, the RSA gives us a signal from the spins which were initialized by numerous previous pulses and were accumulated. It is possible when the spin relaxation time has the same order of magnitude as the laser repetition rate. Taking into account that the resident electron localization time τ_L = 5 ns and the repetition rate of the laser system we utilized is 13.2 ns, the RSA must sense the response from the electrons which have already hopped. Indeed, at the moment of the next pulse arrival, only below 10 % of carriers keep their initial localization site. Meanwhile, the transients represent the spins that were just recently

initialized by a pump pulse and mostly did not yet hop. Thus, a comparison of the KR transients with the RSA signal shows us a difference between the carriers that had a number of hops and carriers keeping their initial localization.

The RSA curves are shown in Fig. 5.10(a) measured at the different spectral regions i.e. selectively interacting with the differently localized resident electrons. The experimental conditions were the same as the KR. The spectral positions of the RSA curves are shown in Fig. 5.10(b) on the PL spectrum. Each curve looks like a horizontal line with evenly spaced Lorenz-like peaks or dips at the upper curve. The vertical dashed lines at the centre and sides of the range show us that the spacing between the peaks is the same for all the curves.

The peak-to-peak intervals ΔB between the Lorentzians are determined by the electron g-factor as $\Delta B = 2\pi\hbar/g_e\mu_B T_R$, where T_R is a period between the laser pulses. Having a few peaks one can extract the g-factor value with very high precision. In our case, the RSA extracted g-factors have a systematical error of about 5% caused by the uncertainty in the magnetic field determination. Hence we do not compare g-factors value measured by the RSA and the other techniques directly.

A precise look at the intervals between the peaks in Fig. 5.10(a) gives us a rather weak difference in the g-factor values within the spectral region, the variation has an order of about 0.2 %. The spectral dependence of g-factor extracted from RSA is shown in Fig. 5.11 by blue dots. They are normalized on the value corresponding to D^0X to be able to compare with the spectral dependencies measured by other techniques. Despite the fact of the dependence is an order of magnitude worse pronounced in comparison to other methods, we clearly see it.

We have extracted the Larmor frequencies from the long-lived 3PE and KR data shown in Fig. 5.7, and the corresponding g-factor dependencies are shown in Fig. 5.11. For the comparison with the RSA, we have normalized the dependence on the low energy spectral region corresponding to D^0X, samely as for RSA. The difference in measured by both KR and 3PE values between D^0X and X^- is about 2 %. The shape of the spectral dependence is quite the same for both long-lived 3PE and KR. The difference is an order of magnitude stronger than RSA shows, which matches the fact that only about 10 % spins remain in its localization site after the T_R.

The width of the peak represents the spin relaxation time as $B_{1/2} = \hbar/g_e\mu_B T_{2,RSA}$. We show one sample of the fit by a Lorentzian function in Fig. 5.10(a) by red dashed line, its FWHM is 0.76 mT, which corresponds roughly to the spin relaxation time $T_{2,RSA} = 17$ ns. The peaks in one curve have roughly the same width, so we have chosen one of the central ones as shown in Fig. 5.10(a). Here we use a simplified approximation of the RSA curve, considering it as a set of Lorentzians while the more

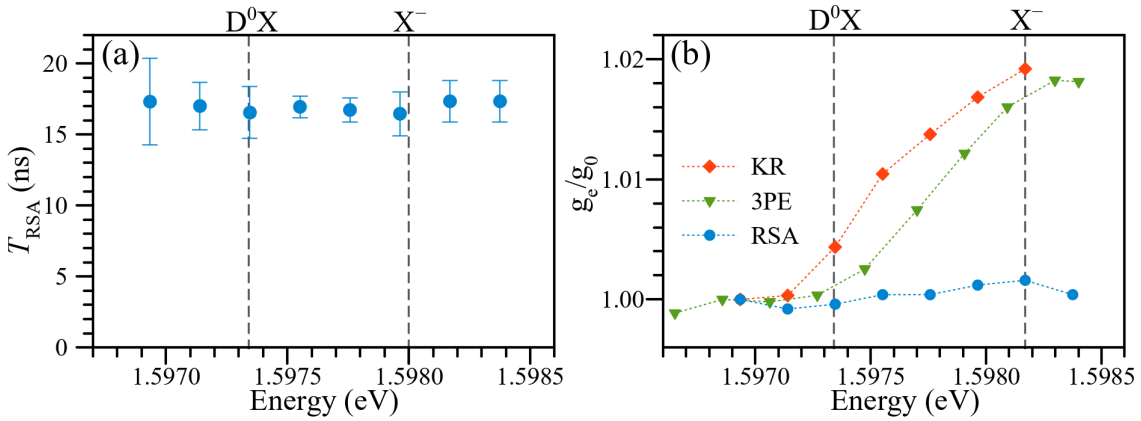

Figure 5.11: *(a) Spectral dependence of the spin relaxation time T_{RSA} extracted from the width of the RSA peaks. (b) Spectral dependence of the g-factors extracted from the 3PE, KR transients and RSA. The g-factor is normalized on the value corresponding to D^0X. 3PE and KR were meeasured at $T = 2$ K and $B = 0.2$ T.*

comprehensive description can be found in work [GI08]. Since RSA is measured at the low magnetic field values, and the zero field peak has the same amplitude as the following, the inhomogeneity impact is low and we can claim the spin relaxation time extracted from RSA is homogeneous. Indeed, the RSA-measured spin relaxation time has a value of the same order as the spin homogeneous spin relaxation times $T_{2,KR}$ and $T_{2,PE}$ we estimated above. The spectral dependence of the RSA-measured spin relaxation times is shown in Fig. 5.11(a). The absence of the spectral dependence of the spin relaxation times and g-factors in the RSA signal shows us that the resident electrons after a sequence of hop are localized in similar potentials and therefore do not show us a difference in their behaviour.

5.4 Conclusions

One of the main achievements of the work presented in the chapter is development the all-optical method of resident electron microscopic dynamics monitoring. The method is based on a comparison of the resident electron spin behaviour revealed by both the long-lived three-pulse photon echo and the time-resolved Kerr rotation (ellipticity) techniques. The signal formation mechanisms of the techniques are differently sensitive to the resident carrier hopping between the localization sites. Hopping decreases the spin relaxation time we see by the long-lived 3PE while increases one we see by the time-resolved Kerr rotation. Establishing the microscopic theory, the certain values of the spin relaxation times measured by those two methods allow one to all-optically evaluate the localization time τ_L i.e. the typical time between the hopping events.

Using the combination of time-resolved KR and long-lived 3PE we have measured the following resident carrier localization times in 10 nm width CdTe-CdMgTe QW: at 1.5 K for the electrons localized on donor do not hop $\tau_L \approx \infty$; the electrons localized on potential roughness $\tau_L \approx 5$ ns; at 6 K for the electrons localized on donor $\tau_L \approx 5$ ns; and the electrons localized on potential roughness $\tau_L \approx 2$ ns.

The resident electron localization time is an important parameter of the resident electron, especially when we consider it as a place to store coherence. In particular, in this chapter, we have observed the spin relaxation caused via the hyperfine interaction, in which the spin relaxation time is defined by the localization time τ_L. Reduction of the localization time leads to an increase in the spin relaxation times, which is provided by the motional narrowing effect and was also demonstrated in the chapter.

The time-resolved techniques as 3PE and KR show us the dynamics of the ensemble right after its initialization during a few nanoseconds, taking into account the spin localization time has a value of units of nanoseconds we see the signal mostly originated from the carriers remaining at the initial spot. Meanwhile, RSA shows us the signal from the carriers were initialized by the previous pulses i.e. at least 13 nanoseconds ago, and most probably have already changed their localization site. After the hopping, resident electrons show us sufficiently different spin relaxation times, and their spectral dependence compared to ones we saw at their initial state in the KR transients.

We have measured the homogeneous spin relaxation times. The electrons localized on the potential fluctuations and accesses via X^- give us homogeneous spin relaxation times $T_{2,KR} \gtrsim 20$ ns measured by time-resolved Kerr rotation, and $T_{2,PE} \approx 4$ ns measured by long-lived 3PE. On the other hand, the electrons localized on the donor atom and accessed via D^0X give us $T_{2,KR} \approx T_{2,PE} \approx 10$ ns using both the techniques. The RSA shows us $T_{2,e} = 17$ ns independently of the optical resonance we used to address the spin of the resident electron.

Chapter 6

Storing optical coherence in spin ensemble of the QD resident electrons

The resident electrons localized in the quantum dot are protected from hopping at the low temperature by their localization depth and show rather long spin-relaxation times reaching units of μs [Kro+04; Gre+09], which makes them attractive for coherence storage. The approach to store the optical coherence into a spin of the resident electron was developed in the ensembles of the quantum wells [Lan+14; Sal+17b; Kos+19] when the resident electron is optically accessed via negatively charged exciton. Such transfer of the coherence allows one to extend the coherence lifetime from tens or hundreds of picoseconds limited by the exciton lifetime to units of nanoseconds limited by spin relaxation time.

Despite the fact, the approach is known for years [Lan+14; Sal+17b], its application to ensembles of quantum dots was hampered by a low spectral density of QDs and therefore a weak long-lived 3PE signal. In this chapter, we report the observation of the long-lived 3PE from the singly charged QDs in the optimally designed sample, where microcavity and the annealing improved the light-matter interaction. Using the structure, it was possible to perform a robust transfer between the optical transition and spin of the resident electron. The transfer was done in frame of the 3PE protocol in the moderate transverse magnetic field.

The long-lived 3PE we observed from the QDs could not be quantitatively explained using the model proposed in work [Lan+14], which implied a sufficient dominance of the electron g-factor value compared to heavy-hole. The assumption is not applicable for the InGaAs QDs, where the g-factors of the electrons and heavy holes have the same order of magnitudes, so the model has been extended.

6.1 Photon echo from trions in QDs

The long-lived 3PE can appear only from the charged QDs where the trion can be formed. In the neutral quantum dot, the exciton has a single qraund state and therefore can not be used for long-lived coherence storage. The energy scheme of the X^- is well described by the four-level scheme with two Kramers doublets in the ground and excited states in absence of the magnetic field, which is shown in the Fig. 6.1(a). The doublet in the ground state is determined by the spin of the resident electron, and the doublet in the excited state by the angular momentum of the heavy hole. Thus, only charged QDs are suitable for the long-lived storage of coherence.

Even though the QDs in the sample are supposed to be negatively charged by closely deposited Si δ-layer, we have to prove the trion formation. One can distinguish between three- and four-level systems using the PE polarimetry technique, which is described in Sec. 2.4.1. In the ensembles of QDs, the inhomogeneous broadening is large compared with the trion binding energy and does not allow to separate X^0 and X^- spectrally as was possible in QWs (see Sec. 5). Moreover, the cavity with a Q-factor of 1000 forms a relatively narrow spectral region defining the laser's wavelength. In Fig. 6.1(b) are shown the 2PE polar plots using HRH and HRV polarization protocols

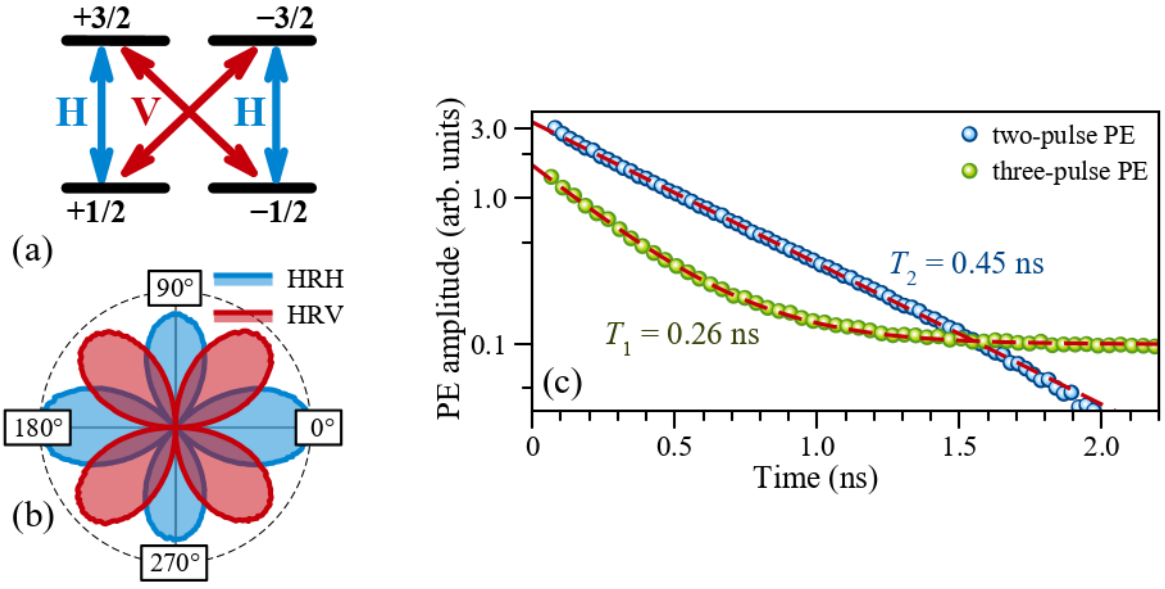

Figure 6.1: *(a) trion energy level diagram; (b) polar plots of 2PE amplitude in HRH and HRV polarization configurations at $t = 2\tau_{12} = 132$ ps; (c) Photon echo from trions in the sample with InGaAs QDs in the cavity with Q-factor of 1000. Decay of the 2PE and 3PE as a function of $2\tau_{12}$ and τ_{23}. In the three-pulse PE the delay time $\tau_{12} = 33.3$ ps. Dashed red curves show the corresponding exponential fits.*

i.e. rotation (R) of the second pulse polarization while the first pulse polarization was kept H and the detection had polarization H or V represented by blue or red curve correspondingly. We set $\tau_{12} = 66$ ps, which is sufficiently shorter than the typical T_2 in QDs [Kos+20; Gri+22]. The polar plots clearly show us the four-lobe dependencies with the clearly seen maxima of the signal in HHH and HVH. It follows a typical dependence $\varphi_{\mathrm{PE}} = 2\varphi_{12}$ for the X^-, where the angle between the H and R linear polarizations is φ_{12}, and the angle between H and PE linear polarizations is φ_{PE}. The 2PE amplitude is independent of the φ_{12}. For the neutral exciton, the polar plot has two-lobe symmetry, the 2PE is co-polarized with the second pulse i.e. $\varphi_{\mathrm{PE}} = 2\varphi_{12}$, and the 2PE amplitude follows $|\cos\varphi_{12}|$. Thus we clearly identify the excitation corresponds to the negatively charged exciton X^-.

The well-seen difference of about 15% between the 2PE amplitudes in HHH and HVH is not sensitive to a rotation of the sample and therefore is not related to the crystal impact on the dipole element anisotropy in the xy-plane. The difference can originate from the neutral exciton contribution to the dominating trion signal, which would increase the only HHH amplitude being two-lobe.

Nevertheless, from Fig 6.1(b) we clearly see that the X^- gives the biggest contribution to the observed signal at the photon energy of 1.434 eV in the studied sample. It shows us that most of the QDs are charged. Considering the platform for the potential application, we point out that the control of the doping is required for the high efficiency of the protocol implementation.

From the 2PE and 3PE decays Fig. 6.1(c) we evaluate T_2 and T_1 of the X^-. The 2PE shows an exponential decay, it was approximated by a single exponent with a decay time $T_2 = 0.45$ ns. The value is in good agreement with the previously seen in InGaAs QDs [Pol+16; Kos+20; Bor+01; Sal+17a]. The 3PE decay shown in Fig. 6.1(c) consists of an exponential decay with an offset, which is almost independent on τ_{23}. The decay time $T_1 = 0.26$ ns represents here the trion lifetime τ_{r}. The offset is weak, having about 5 % of the maximal signal. This weak signal is governed by the dynamics of population grating in the ground state of the QDs ensemble and can occur for many different reasons, which are out of the scope of this work. We point out that $T_2 \approx 2T_1$, which shows us the loss of optical coherence takes place because of radiative recombination of trion.

6.2 Long-lived spin-dependent photon echo in QDs

Both ground and excited states of the X^- consists of the doublets. Application of the magnetic field ($\vec{B} \parallel x$) leads to their Zeeman splitting. The electron spin has a projection of the spin $S_x = \pm 1/2$ which are split by $\hbar\omega_e = g_e \mu_B B$. The X^- states have the angular momentum $J_x = \pm 3/2$ and are split $\hbar\omega_h = g_h \mu_B B$. The splitting in the magnetic field is defined by their g-factors, here ω_e, ω_h are Larmor frequencies, g_e, g_h are the g-factors of the electron and hole.

Using H and V-polarized light we can drive optical transitions according to the scheme shown in Fig. 6.1(a). The four-level structure can be considered as two Λ systems sharing the ground states, the magnetic field makes them asymmetric. In that case, the optical coherence created by the first pulse can be transferred by the second pulse into the spin coherence [Lan+14; Sal+17b].

A sequence of two-linearly polarized pulses separated in time by $\tau_{12} < T_2$ can be used to form a spin fringe in the ground and excited states of the X^-. The certain spin component we address depends on the polarization of the pulses. For instance, two linear co-polarized HH pulses form the spin with the components directed along the magnetic field, which has a shape of:

$$S_x = -J_x \propto \sin\left(\frac{\omega_e - \omega_h}{2}\tau_{12}\right) \exp\left(-\frac{\tau_{12}}{T_2}\right) \cos\left(\omega_0 \tau_{12}\right). \tag{6.1}$$

The deriviation of the expression can be found in the supplementary material of the [Kos+22], where the Expr. 6.1 corresponds to Eq. 35.

The cross-polarized HV sequence of pulses forms a spin grating in the yz-plane, which is perpendicular to the magnetic field direction.

$$S_y + iS_z = J_y - iJ_z \propto i \exp\left(i\frac{\omega_e - \omega_h}{2}\tau_{12}\right) \exp\left(-\frac{\tau_{12}}{T_2}\right) \cos\left(\omega_0 \tau_{12}\right). \tag{6.2}$$

The Expr. 6.2 corresponds to Eqs. 36 and 37 in the supplementary material of [Kos+22]

The spin population and its dynamics in the magnetic field is given by the evolution of spin fringes defined by Eqs. 6.1 and 6.2. First of all, the spin fringe formed in the heavy hole spin states is limited by X^- lifetime. In contrast, the electron spin fringe is associated with the ground state and consequently is not limited by the short lifetimes of the optical excitations, being limited only by spin relaxation mechanisms that are sufficiently longer.

Those spin fringes give a coherent response when an extra pulse fulfilling FWM formation conditions is applied. The third pulse must have the same polarization as the second one, it transfers the spin fringe back to the optical coherence and starts

rephasing resulting in the 3PE. The decay of the long-lived 3PE amplitude as a function of the delay τ_{23} is associated in the case with a decay of the spin fringe. The HHHH polarization protocol reflects S_{x}, which decays with longitudinal spin relaxation time $T_{1,\mathrm{e}}$. The HVVH polarization protocol shows us the evolution of $S_{\mathrm{y}} + iS_{\mathrm{z}}$, which decays with transverse $T^*_{2,\mathrm{e}}$ spin relaxation time.

The existing theoretical model was done to describe the long-lived 3PE from the CdTe/(Cd,Mg)Te QW, where the g-factor of the electron is an order of magnitude bigger than one of the heavy hole. The model was made neglecting the sufficiently weaker heavy hole Zeeman splitting. Nevertheless, in the InGaAs QDs we are interested in, the heavy hole g-factor has the same order of magnitude [Tri+21] being $g_h = 0.18$ for the heavy hole and $g_e = -0.52$ for the electron. Thus, such a simplification is not applicable here and the heavy hole Zeeman splitting must be accounted for. It is also known from the work [Tri+21], that the heavy hole g-factor is anisotropic, i.e. its certain value depends on mutual orientation of the magnetic field and the crystallographic axis. The anisotropy of g-factor is a known phenomenon in A_3B_5 based QWs and QDs [MH00] and can be detected by PE technique as was shown in the work [Pol+20b]. Thus, the impact of the crystal orientation-originated anisotropy is known and can be correctly taken into account. In the chapter, the sample was oriented so the direction [110] was set parallel to the $\vec{B}$, then the corresponding optical frequencies of the H and V polarized optical transitions have the photon energies of $\hbar\omega_0 \pm (\omega_e - \omega_h)$ and $\hbar\omega_0 \pm (\omega_e + \omega_h)$, respectively.

We have measured the 3PE from the InGaAs QDs, the sample description can be found in Sec. 3.1.3. The measurements were done as a dependence on τ_{23} and also as a function of the magnetic field. The dependences on the magnetic field were measured while the delays between the pulses remained constant, where $\tau_{12} = 100$ ps $\ll T_2$ and $\tau_{23} = 2033$ ps $\gg T_1$ in order to separate the long-lived signal from the regular 3PE.

The Fig. 6.2(a) show the transients, measured in HHHH and HVVH polarization protocols, which are shown by the green and blue symbols. Both show a rapidly decaying component corresponding to the optical relaxation times $T_1 = 0.26$ ns, which represents the regular 3PE. The signal range from ≈ 1.5 ns is free from the contribution.

The signal in HHHH polarization protocol was measured at $B = 0.3$ T and $\tau_{12} = 66$ ps, after the short component we see a rather long decay with a relaxation time exceeding tens of nanoseconds so $T_{1,\mathrm{e}} \gg 10$ ns. Since the laser repetition rate is 13.2 ns, accumulative effects can occur and therefore we can only do such an estimation. The same long-lived component but with noticeably lower amplitude is seen in Fig. 6.1(c) in the 3PE. In Fig. 6.2 we see how the 3PE amplitude behaves on the $\tau_{23} \gg T_1$, the signal rises with the magnetic field in the range from 0 to 0.5 T, but not equal to zero

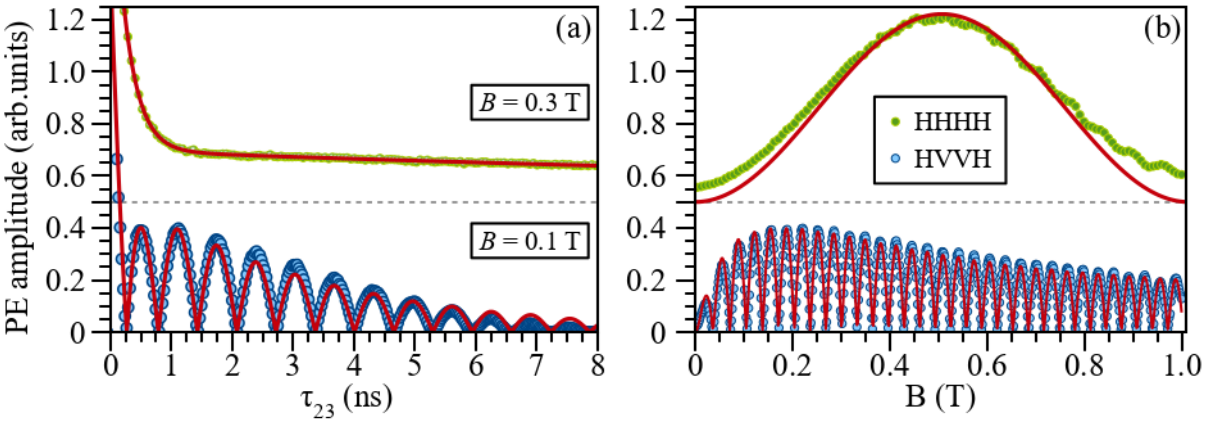

Figure 6.2: *Long-lived 3PE from QDs in cavity with Q-factor of 1000 (a) 3PE amplitude as a function of τ_{23} when $\tau_{12} = 66$ ps. HHHH and HVVH polarization schemes at B =0.3 T and 0.1 T, respectively. (b) Magnetic field dependence of the long-lived 3PE when τ_{12} = 100 ps and τ_{23} = 2.033 ns. Top and bottom curves correspond to signal measured in HHHH and HVVH polarization protocols, respectively. Red lines present the results of the theoretical modeling using Eqs. 6.3 and 6.4 with the following parameters: $g_e = -0.516$, $g_h = 0.18$, $T_T = \tau_r = T_1 = 0.26$ ns, $T_{1,e} = 23$ ns, $T^*_{2,e}$ is evaluated from $T_{2,e} = 4.3$ ns and $\Delta g_e = 0.004$ using Eq. 6.10 (as follows from Fig. 6.4(a)). The signals in HHHH polarization are shifted for clarity with the dashed line corresponding to zero signal level.*

in absence of magnetic field. Nevertheless, we clearly see that in the magnetic field of 0.3 T the major part of the signal is related to the magnetic field, and sufficiently exceeds the offset we see in $B = 0$ T.

The signal in HVVH polarization protocol was measured in $B = 0.1$ T and $\tau_{12} = 66$ ps, it is shown in Fig. 6.2(a) by blue dots. The signal oscillates with the Larmor frequency and decays with $T^*_{2,e} \approx 3.5$ ns. A weaker amplitude of the first oscillation is related to the contribution of the regular 3PE.

Another way of consideration is the dependence of the long-lived 3PE amplitude on the magnetic field. The experimental results are shown in Fig. 6.2(b). The long-lived 3PE signal in the HVVH polarization protocol is shown by the blue dots. In full accord with the theory, the signal is equal to zero in absence of the magnetic field. In the magnetic field, the signal oscillates with the frequency corresponding to the electron rotation during τ_{23}, which is enveloped by a sufficiently more gradual function. The envelope rises in the range of magnetic field from 0 to 0.2 T and then slowly decreases losing roughly half of its amplitude at the field of 1 T.

The HHHH signal makes one slow oscillation, that corresponds to the collective flip of the electron and hole spin in the magnetic field during τ_{12}, i.e. during the spin grating initialization. Since the τ_{12} is almost 20 times shorter than τ_{23}, the resulting oscillation in the HHHH polarization protocol is noticeably slower.

The quantitative description of the effect was done in the approximation of the negligibly small heavy hole states Zeeman splitting [Lan+14], so the model has to be extended. Since the thesis is dedicated to the experimental part of the work, we will not discuss here the corresponding theory in detail and only summarize the results. Meanwhile, the comprehensive solution can be found in the supplementary material of the corresponding work [Kos+22].

Briefly, the analytical description is based on the Lindblad equation solution for the (4×4) density matrix describing the four levels of X^-. It comprehensively describes the behaviour of the system from the initialization by the first pulse up to the second pulse's arrival, when the spin fringes are formed. The evolution of the spin fringes in the magnetic field can be solved already using the Bloch equations, such consideration simplifies the resulting expressions. The resulting long-lived 3PE amplitude reflects the state of the spins at the moment of the third pulse arrival. As a summary, we show below the expressions for the 3PE amplitude for HHHH and HVVH polarization protocols. The amplitude depends on the system properties as the spin trion lifetime T_T^{-1}, trion radiative decay lifetime τ_r, population lifetime T_1, electron longitudinal $T_{2,e}^*$, transverse $T_{1,e}^*$ relaxation times, and g-factors of the electron and heavy-hole g_e and g_e. The only experimental condition in the equations are τ_{12}, τ_{23}, and the magnetic field amplitude B.

$$\begin{aligned} P_{\mathrm{HHHH}} \propto \mathrm{e}^{-\frac{2\tau_{12}}{T_2}} [2\mathrm{e}^{-\frac{\tau_{23}}{\tau_r}} \cos^2\left(\frac{g_e - g_h}{2}\mu_B B\tau_{12}\right) + \\ \mathrm{e}^{-\frac{\tau_{23}}{T_T}} \sin^2\left(\frac{g_e - g_h}{2}\mu_B B\tau_{12}\right) + \\ \mathrm{e}^{-\frac{\tau_{23}}{T_{1e}}} \sin^2\left(\frac{g_e - g_h}{2}\mu_B B\tau_{12}\right)] \end{aligned} \tag{6.3}$$

The spin lifetime of the trion is defined here as $T_T^{-1} = \tau_r^{-1} + T_h^{-1}$, but in the moderate magnetic fields $B \leq 1$ T the hole spin relaxation time T_h is sufficiently longer than the τ_r and, therefore, in our case $T_T = \tau_r$ [Gre+06b]. The first two addends in the formula above are related to the trion contribution, while the last is related to long-lived 3PE from the resident electrons.

For HVVH polarization we obtain

$$\begin{aligned} P_{\mathrm{HVVH}} \propto \mathrm{e}^{-\frac{2\tau_{12}}{T_2}} [\mathrm{e}^{-\frac{\tau_{23}}{T_T}} r_h \cos\left(g_h\mu_B B\tau_{23} - (g_e - g_h)\mu_B B\tau_{12} - \phi_h\right) \\ + \mathrm{e}^{-\frac{\tau_{23}}{T_{2,e}^*}} r_e \cos\left(g_e\mu_B B\tau_{23} + (g_e - g_h)\mu_B B\tau_{12} - \phi_e\right)] \end{aligned} \tag{6.4}$$

In the expression in addition to the introduced above parameters, we used the phases ϕ_{e}, ϕ_{h}, and amplitudes r_{e}, r_{h} which depend on $B, g_{\mathrm{e}}, g_{\mathrm{h}}, \tau_{12}, \tau_{\mathrm{r}}$. According to the theory, they have the following shape:

$$r_e = \sqrt{p_e^2 + q_e^2}, r_h = \sqrt{p_h^2 + q_h^2} \tag{6.5}$$

$$\cos\phi_e = p_e/r_e, \sin\phi_e = q_e/r_e, \cos\phi_h = p_h/r_h, \sin\phi_h = q_h/r_h. \tag{6.6}$$

where we use intermediate parameters p_e, p_h, q_e and q_h, which defined as:

$$\begin{aligned} p_e &= 1 - D_1 - D_2\cos[(\omega_e - \omega_h)\tau_{12}] + D_4\sin[(\omega_e - \omega_h)\tau_{12}] \\ q_e &= -D_3 - D_2\sin[(\omega_e - \omega_h)\tau_{12}] - D_4\cos[(\omega_e - \omega_h)\tau_{12}] \\ p_h &= 1 + D_1 + D_2\cos[(\omega_e - \omega_h)\tau_{12}] + D_4\sin[(\omega_e - \omega_h)\tau_{12}] \\ q_h &= -D_3 - D_2\sin[(\omega_e - \omega_h)\tau_{12}] + D_4\cos[(\omega_e - \omega_h)\tau_{12}] \end{aligned} \tag{6.7}$$

Here the coefficients D_{i} are introduced here for simplification of the Exprs. 6.7 and we do not associate them with certain effects. They are defined in the following way:

$$\begin{aligned} D_1 &= \frac{\gamma}{2\tau_r(\gamma^2 + (\omega_e + \omega_h)^2)} \\ D_2 &= \frac{\gamma}{2\tau_r(\gamma^2 + (\omega_e - \omega_h)^2)} \\ D_3 &= \frac{(\omega_e + \omega_h)}{2\tau_r(\gamma^2 + (\omega_e + \omega_h)^2)} \\ D_4 &= \frac{(\omega_e - \omega_h)}{2\tau_r(\gamma^2 + (\omega_e - \omega_h)^2)} \end{aligned} \tag{6.8}$$

Here we used $\gamma = 1/T_{\mathrm{T}} - 1/T_{2,\mathrm{e}}$. Origination of the Expr. Exps. 6.6,6.7, 6.8 can be found in the supplementary materials of the work [Kos+22]. For the simulations, the g-factors were taken from the previous study [Tri+21; Kam+20].

The Expr. 6.4 describes the behaviour of the system rather comprehensively but can be simplified for the case of the transients. Such type of measurements is usually done with a constant magnetic field amplitude, the parameters ϕ_{e}, r_{e}, r_{e}, $T^*_{2,\mathrm{e}}$ are here just constants. Moreover, considering the ling-lived signal on the τ_{23} bigger than trion relaxation times we can omit the first term associated with the heavy hole contribution. Thus the expression can be represented as:

$$P_{\mathrm{HVVH}} \propto r_e \exp(-\tau_{23}/T^*_{2,\mathrm{e}})\cos(\omega_e\tau_{23} + (\omega_e - \omega_h)\tau_{12} - \phi_e), \tag{6.9}$$

the expression is a more precise version of the Expr. 5.3.

Now we compare the dependence of the parameters ϕ_{e}, r_{e}, $T^*_{2,\mathrm{e}}$ on the magnetic field, using the Exps. 6.6,6.7, 6.8 and the data extracted from the experiment. For this

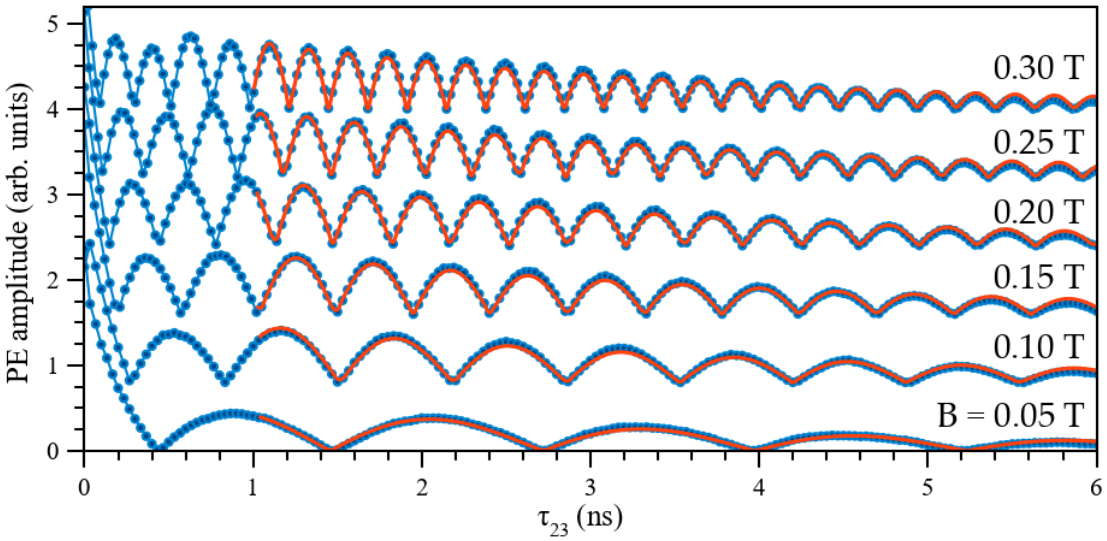

Figure 6.3: *Transients of the long-lived 3PE measured using the HVVH polarization protocol in the different magnetic fields in a range from 0.05 to 0.3 T. The dashed lines represent the fit by the Expr. 6.9.*

purpose, we measured a few transients in a range of B from 0.05 to 1 T, some of the experimental curves shown in Fig. 6.3. The red dashed lines represent fit by Expr. 6.9. Since the beginning of the signal is impacted by a regular 3PE we do not fit in the region $\tau_{23} < 1$ ns. All the dependencies show an excellent match to the experimental data. From them we extract the fitting parameters $\phi_e(B)$, $r_e(B)$, $T^*_{2,e}(B)$ and plot them in Fig. 5.9.

As we have shown above in Sec. 2.1.5, the spin relaxation in the inhomogeneously broadened ensembles occurs from the Larmor frequency dispersion $\Delta\omega$, which we mostly relay to the inhomogeneity of g-factors Δg. So, in the magnetic field, the spin relaxation times we observe must be shortening as:

$$\hbar/T^*_{2,e} = \hbar/T_{2,e} + \Delta g_e \mu_B B, \tag{6.10}$$

The experimentally observed dependence $1/T^*_{2,e}(B)$ is shown in Fig. 6.4 by the blue dots. It clearly represents a linear dependence in full accord with our expectations. The only first point slightly deviates from it, we associate the deviation with the hyperfine interaction with the nuclei, but it goes out of this research scope. Fit by a linear function is shown in Fig. 6.4(a) by the red dashed line, it gives us the homogeneous spin relaxation time $T_{2,e} = 4.3$ ns and inhomogeneity value of $\Delta g_e = 4 \times 10^{-3}$. The $T_{2,e}$ is close to the one we observed previously in the CdMgTe/CdTe QW, while inhomogeneity is roughly doubly smaller [Kos+19].

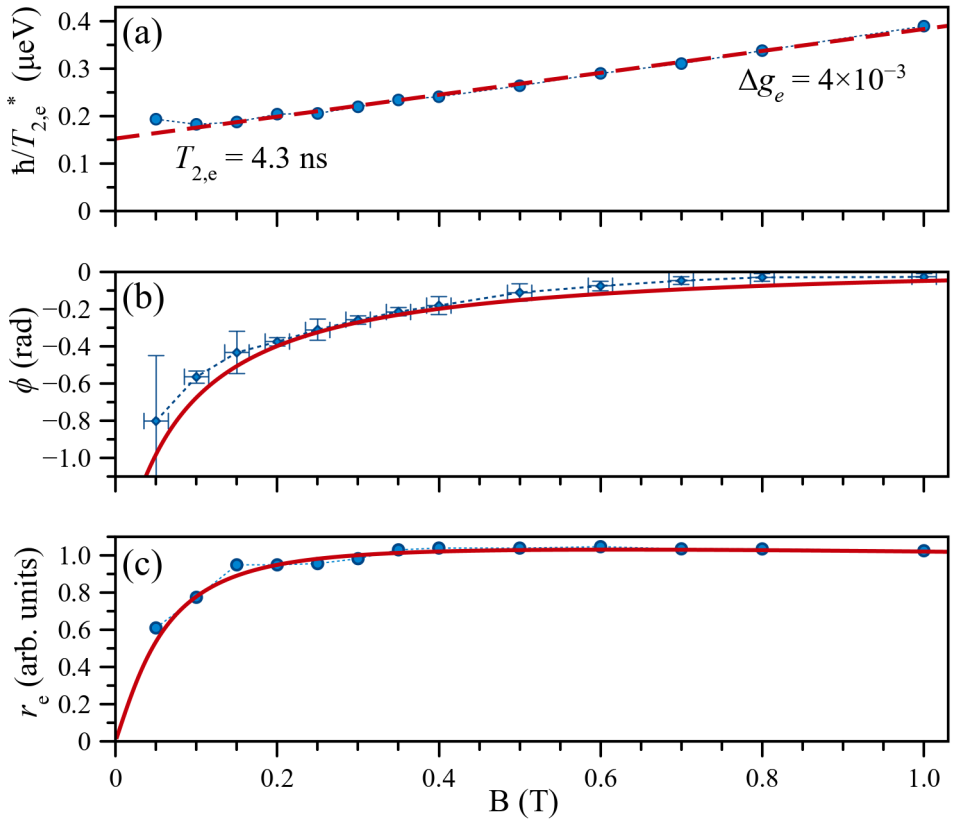

Figure 6.4: *Parameters of the long-lived 3PE depending on the magnetic field. The data summarizes the set of measurements shown in Fig. 6.3. (a) decay time $\hbar/T_{2,e}^{*}$; (b) phase ϕ; (c) amplitude r_e. Blue points correspond to the data resulting from the fit using the last term on the right-hand side in Eq. 6.9. Red dashed line in (a) is fit by linear function from Eq. 6.10 with $T_{2,e} = 4.3$ ns and $\Delta g_e = 4 \times 10^{-3}$. Red solid line in (b) and (c) - magnetic field dependences of φ and r_e given by analytic expressions from supplementary material.*

Fig. 6.4(b) shows a magnetic field dependence of the oscillation's phase $\phi_e(B)$ by the blue points. It has a value of -0.8 rad ($\approx \pi/4$) in the magnetic field below 0.1 T, and it gradually rises up to roughly 0.1 in the field of 0.6 T. In the higher fields, ϕ_e limits to zero, going towards the older model. The red line represents the corresponding analytical dependence, which we obtained from the Expr. 6.6 using here $g_\mathrm{e} = -0.516$, $g_\mathrm{h} = 0.18$, $T_\mathrm{T} = \tau_\mathrm{r} = 0.26$ ns and $\tau_{12} = 33.3$ ps. There is an excellent agreement between the experimental data and analytical expressions.

Fig. 6.4(c) shows a dependence of the signal's amplitude r_r on the magnetic field by blue points. It has a zero amplitude at the zero fields and reaches its maximal possible amplitude around $B = 0.2$ T, where saturates and remains the same at the higher fields. The red solid line shows the prediction of the analytical expressions, which perfectly describes the experimental data.

In the limit of high magnetic fields i.e. $|(\omega_e - \omega_h)|\tau_{12} \gg 1$ the formulas simplify since both long-lived 3PE amplitude ($r_e \rightarrow 1$) and the phase ($\phi_e \rightarrow 0$) reach their limiting values. In that case one can use the simplified expression $P_{\mathrm{HVVH}} \propto \cos[\omega_e \tau_{23} + (\omega_e - \omega_h)\tau_{12}]$. The expression is close to the one we used before, but now takes into account the mutual rotation of the electron and hole during τ_{12}, which was not revealed before.

Knowledge of the parameters $T_{2,e}(B)$, $r_e(B)$ and $\phi_e(B)$ presented in the Fig. 6.4 completely define the long-lived 3PE signals in the HVVH and HHHH polarization protocols. Fitting curves in Fig. 6.2 were done using the parameters, we see an excellent agreement between the experiment and the analytical model. The only deviation we notice is seen in the HHHH polarization protocol, we relay it to the population grating as we discussed above. The HVVH polarization protocol dependence on the magnetic field shows a perfect match of the analytical model and the experimental data.

6.3 Conclusion

We have shown that the resident electron spin degrees of freedom can be utilized for the sufficient extension of the coherence lifetime in the InGaAs quantum dots. Using an HVVH polarization protocol in the magnetic field in the frame of 3PE has allowed us to transfer the optical coherence into the resident electron spin sub-ensemble, extending its lifetime by an order of magnitude from hundreds of picoseconds to units of nanoseconds. Now the coherence lifetime is limited by the hyperfine interaction with the nuclei [Mer+02; Gla18], which differently impacts each particular QD. Nevertheless, the spin relaxation time can be extended here by a combination of the spin echo techniques with dynamic decoupling, which potentially allows one to reach a range of microseconds [Gre+06a; Bec+15; Hut+18] in our case. Moreover, the longitudinal spin relaxation time can reach up to a few seconds [Gil+21].

Qualitatively, the effect we have observed in the InGaAs QDs is the same as the one we saw in CdTe QW [Kos+19] or Sec. 5, nevertheless, the QD is more perspective platform for the quantum science and technology, which is defined by the more robust optically driven Rabi oscillations, longer T_2 and the weaker excitation induced dephasing than in the quantum wells [Kos+20]. The parameters are essential for optical coherence retrieval.

Conclusions

In the work, we have studied the ultrafast coherent optical dynamics of the charged excitons. In **Chapter 4**, we have considered the behaviour of the inhomogeneously broadened ensemble of InGaAs QDs, and the method to freeze the dephasing of the inhomogeneously broadened ensemble under an action of the resonantly tuned optical pulse with an area of 2π. We show how the coherent pulses with an area of 2π or multiple numbers such pulses lead to an inhibition of dephasing (rephasing) during the pulse action. The main conclusions of the chapter:

- We demonstrate that application of control pulse with an area of $2\pi n$ (where $n \in \mathbb{N}$) of a finite duration freezes dephasing (rephasing) of the inhomogeneously broadened ensemble. It is fair for the following assumption $\Omega_R \gg \Delta$ and $(\Delta/\Omega_R)\tau_C\Delta \ll 1$, where Δ is spectral width of the inhomogeneous ensemble, Ω_R is Rabi frequency, τ_C is a pulse duration.

- Duration of the dephasing (rephasing) freezing depends on the control pulse duration and does not depend on the certain moment of the control pulse application within dephasing or rephasing regimes.

- We have used the concept to vary the moment of two-pulse photon echo formation, while its temporal shape does not experience strong variations. The echo timing was varied on the timescale comparable with its duration.

- The observed variations of the photon echo timing were described by a model based on the optical Bloch equations, taking into account the inhomogeneity of the excitation laser spot.

The deterministic control of the PE timing can on the ultrafast timescales e.g. for timing correction in memory protocols [Lvo+09; Tit+10; Zho+17].

In **Chapter 5** we have investigated the microscopic dynamics of the resident electron in the CdTe QW. The main conclusions of the chapter:

- We demonstrated that independently of the particular spin relaxation mechanism, the hopping of resident electrons leads to a shortening of the photon echo decay time.
- The transverse spin relaxation time evaluated from pump-probe transients increases due to the motional narrowing of spin dynamics in the fluctuating effective magnetic field of the lattice nuclei.
- Combination of the long-lived three-pulse photon echo and time-resolved Kerr rotation allowed us all-optically measure the resident electron localization time.
- We evaluated the localization times of the resident electrons with the density of 10^{11} cm^{-2} between the hopping events τ_L in the 20 nm CdTe QW structure: at 1.5 K for the electrons localized on donor do not hop; the electrons localized on potential roughness $\tau_L \approx 5$ ns; at 6 K for the electrons localized on donor $\tau_L \approx 5$ ns; and the electrons localized on potential roughness $\tau_L \approx 2$ ns.
- comparison with the resonant amplification technique has shown us that during 13.2 ns most of the electrons have hopped to the localization place, where their properties do not show pronounced spectral dependence.

By controlling the electron spin correlation time τ_c, it is possible to optimize interaction between the nuclear spins and spin of the residen electron, since τ_c has a direct impact on the hyperfine interaction-induced dynamical nuclear polarization, as indicated by references [Gla18; MZ84].

In **Chapter 6** we have demonstrated the long-lived three-pulse photon echo from an ensemble of the negatively charged excitons in the InGaAs QDs.

- We presented a successful transfer from trion optical coherence to spin coherence of resident electrons in the negatively charged exciton in the InGaAs quantum dots and its retrieval with a subsequent 3PE emission.
- The experimental data determined that the existing model was extended in order to include a heavy hole Zeeman splitting in the magnetic field
- We have evaluated the spin relaxation time of resident electrons to be $T_{2,e} = 4$ ns.

The ability to involve the spin degrees of freedom for extension of the coherent response in the ensembles of InGaAs QDs in the presence of a moderate transverse magnetic field is rather important for quantum memory devices with high bandwidth. The storage of the coherence in the spin ensemble allowed to extend its lifetime by an order from 0.5 to 4 ns, now it is limited by the spin dephasing originating from the hyperfine interaction with the nuclei [Mer+02; Gla18]. Usage of the spin echo techniques combined with dynamic decoupling can be used to extend the decay time up to the microsecond time range [Gre+06a; Bec+15; Hut+18], while longitudinal spin relaxation can even reach several seconds [Gil+21].

On the other hand, the implementation of the protocol on the long-lived 3PE on the QDs is more advantageous, compared to QWs. QDs allow establishing robust Rabi oscillations using pulse areas of multiple π [Kos+20], which are required for the quantum memory protocols [Lvo+09].

List of publications

1. A. N. Kosarev, A.V. Trifonov, I.A. Yugova, I.I. Yanibekov, S.V. Poltavtsev, A.N. Kamenskii, S.E. Scholz, C.A. Sgroi, A. Ludwig, A. D Wieck, D.R. Yakovlev, M. Bayer, I.A. Akimov **Extending the time of coherent optical response in ensemble of singly-charged InGaAs quantum dots** *Communications Physics 5.1 (2022): 1-7.*

2. A.N. Kosarev, V.V. Chaldyshev, and N. Cherkashin. **Experimentally-Verified Modeling of InGaAs Quantum Dots** *Nanomaterials 12.12 (2022): 1967.*

3. A.V. Trifonov, S. Grisard, A.N. Kosarev, I.A. Akimov, D.R. Yakovlev, J. Höcker, V. Dyakonov, M. Bayer **Photon Echo Polarimetry of Excitons and Biexcitons in a $CH_3NH_3PbI_3$ Perovskite Single Crystal** *ACS Photonics 9.2 (2022): 621-629.*

4. A.N. Kosarev and V. V. Chaldyshev. **Carrier Localization by a Quantum Dot in a Quantum Well** *Physical Review Applied 16.4 (2021): 044046.*

5. A.V. Trifonov, I.A. Akimov, L.E. Golub, E.L. Ivchenko, I.A. Yugova, A.N. Kosarev, S.E. Scholz, C. Sgroi, A. Ludwig, A.D. Wieck, D.R. Yakovlev, M. Bayer **Homogeneous optical anisotropy in an ensemble of InGaAs quantum dots induced by strong enhancement of the heavy-hole band LandÃ© parameter q** *Physical Review B 104.16 (2021): L161405.*

6. M. Reichelt, H. Rose, A.N. Kosarev, S.V. Poltavtsev, M. Bayer, I.A. Akimov, C. Schneider, M. Kamp, S. Höfling, T. Meier **Controlling the emission time of photon echoes by optical freezing of exciton dephasing and rephasing in quantum-dot ensembles** *Ultrafast Phenomena and Nanophotonics XXV. Vol. 11684. SPIE, 2021.*

7. A.N. Kosarev, H. Rose, S.V. Poltavtsev, M. Reichelt, C. Schneider, M. Kamp, S. Höfling, M. Bayer, T. Meier, I.A. Akimov **Accurate photon echo timing by optical**

freezing of exciton dephasing and rephasing in quantum dots *Communications Physics 3.1 (2020): 1-9.*

8. A.N. Kosarev and V.V. Chaldyshev. **Carrier localization in self-organized quantum dots: An interplay between quantum and solid mechanics** *Applied Physics Letters 117.20 (2020): 202103.*

9. S.V. Poltavtsev, I.A. Yugova, A.N. Kosarev, D.R. Yakovlev, G. Karczewski, S. Chusnutdinow, T. Wojtowicz, I.A. Akimov, M. Bayer **In-plane anisotropy of the hole g factor in CdTe/(Cd, Mg) Te quantum wells studied by spin-dependent photon echoes** *Physical Review Research 2.2 (2020): 023160.*

10. A.N. Kosarev, S.V. Poltavtsev, L.E. Golub, M.M. Glazov, M. Salewski, N.V. Kozyrev, E.A. Zhukov, D.R. Yakovlev, G. Karczewski, S. Chusnutdinow, T. Wojtowicz, I.A. Akimov, M. Bayer **Microscopic dynamics of electron hopping in a semiconductor quantum well probed by spin-dependent photon echoes** *Physical Review B 100.12 (2019): 121401.*

11. A.N. Kosarev, V.V. Chaldyshev, A.A. Kondikov, T.A. Vartanyan, N.A. Toropov, I.A. Gladskikh, P.V. Gladskikh, I. Akimov, M. Bayer, V.V. Preobrazhenskii, M.A. Putyato, B.R. Semyagin **Epitaxial InGaAs quantum dots in Al0. 29Ga0. 71As matrix: intensity and kinetics of luminescence in the near field of silver nanoparticles** *Optics and Spectroscopy 126.5 (2019): 492-496.*

12. A. Kosarev, N. Bert, V. Nevedomskii, V. Chaldyshev, V. Preobrazhenskii, M. Putyato, B. Semyagin **Photoluminescence from InAs Quantum Dots Buried Under Low-Temperature-Grown GaAs** *physica status solidi (b) 256.5 (2019): 1800479.*

13. A. Kosarev, V. Chaldyshev, N. Toropov, I. Gladskikh, P. Gladskikh, K. Baryshnikova, V. Preobrazhenskiy, M. Putyato, B. Semyagin, T. Vartanyan **Fabrication and characterization of coupled ensembles of epitaxial quantum dots and metal nanoparticles supporting localized surface plasmons** *Plasmonics: Design, Materials, Fabrication, Characterization, and Applications XV. Vol. 10346. SPIE, 2017.*

14. S.V. Poltavtsev, A.N. Kosarev, I.A. Akimov, D.R. Yakovlev, S. Sadofev, J. Puls, S.P. Hoffmann, M. Albert, C. Meier, T. Meier, M. Bayer. **Time-resolved photon echoes from donor-bound excitons in ZnO epitaxial layers** *Physical Review B 96.3 (2017): 035203.*

15. N.A. Toropov, I.A. Gladskikh, P.V. Gladskikh, A.N. Kosarev, V.V. Preobrazhenskii, M.A. Putyato, B.R. Semyagin, V.V. Chaldyshev, T.A. Vartanyan **Absorption**

and photoluminescence of epitaxial quantum dots in the near field of silver nanostructures *Journal of Optical Technology 84.7 (2017): 459-461.*

16. A.N. Kosarev, V.V. Chaldyshev, V.V. Preobrazhenskii, M.A. Putyato, B.R. Semyagin **Effect of a low-temperature-grown GaAs layer on InAs quantum-dot photoluminescence** *Semiconductors 50.11 (2016): 1499-1505.*

17. A. Kosarev, E. Apushkinskiy, K. Maximov, E. Ripchinskaya, P. Shamray **Investigation of nonlinear transformations of the signal spectrum** *Journal of Physics: Conference Series. Vol. 574. No. 1. IOP Publishing, 2015.*

Acknowledgements

There is no easy way from the master's to the PhD, so I would like to thank so many people who supported me on the path and hope I have not forgotten to mention someone. First of all, I would like to thank the group of Experimentally Physik 2 for the opportunity to take a part in the team, and especially Prof. Dr. Manfred Bayer for gathering so wonderful people at the same place.

A special thanks to my supervisor Prof. Dr. Ilya Akimov for the guidance and rather pleasant work in the top lab, for uncovering the time-resolved and coherent spectroscopy worlds, and for very welcoming communication. I am very happy with our unimaginably broad areas of research and spectra of techniques beginning from the resident electron dynamics we studied by spin-dependent photon echoes and finishing with the microscopic multicolour pump-probe study of the strain waves in perovskite crystals.

I am very glad to have had the nice experience of working with Dr. Sergey Poltavtsev, who has shown me so complex setup I was working several years with, and even has helped me understand myself better. I thank Dr. Artur Trifonov for his support and long-term mutual work, and Prof. Dr. Dmitri Yakovlev for his contribution to our work.

I am grateful to Dr. Vladimir Chaldyshev for our almost decade of mutual work, his support, supervision during my bachelor's and master's, and for permanently and fruitfully distracting me from the presented work.

It was a pleasure to work with all lab D coworkers, so I thank Jonas Vondran, Dr. Dmytro Horiachyi, Dr. Felix Godejohann, Dr. Ina Kalitukha, Dr. Olga Ken, Dr. Vladimir Korenev, Rilana Reichhardt and Eyüp Yalcin.

I would like to thank the whole E2 for the welcoming and all the members in partic-

ular! I could not achieve anything without the continuous support of my dear friends Lars Klompmaker, Alexander Kamenskii, Dmytro Yaremkevich, Stefan Grisard, Erik Kirstein, Andreas Farenbruch, Nikolay Kozyrev, Rustam Akhmadullin and Dr. Pavel Sokolov. I appreciate Lars' great contribution to my local integration. It was a pleasure to meet here such friendly people as Dr. Matthias Salewski, Dr. Eiko Evers, Dr. Bernt Berger, Dr. Gang Qiang, Dr. Daniel Schmidt, surely Dr. Felix Spitzer and many others.

I thank Dr. Michal Kobecki for the establishment of the "Friday for interesting discussions" club and all the members of the society. It was also a pleasure to take a part in the E2 soccer team.

I also would like to thank Dr. Elena Rozas Jimenez, Dr. Mladen Kotrur, Dr. Natasha Kopteva, Dr. Elena Schornikova, and Dr. Sergiu Anghel for the nice communication during my work at E2.

The work would be impossible without the support of Lars Wieschollek, Katharina Goldack and Michaela Wäscher.

I am thankful to all participants of the TRR 160 and 142 collaborations for our mutual projects, especially I am thankful to the Ioffe Institute, St. Peterburg State University and Paderborn University teams for the collaboration.

I would like my friends outside the TU for the support, especially I am thankful to my kommilitonen Aleksei Konovalov and Aleksandra Ilina for the support on the way.

It is important to thank my family and especially my wife Margarita for the support on the way through difficulties to the completion of the manuscript.

Bibliography

[AE75] L. Allen and J. H. Eberly. *Optical Resonance and Two-Level Atoms*. New York: Wiley, 1975.

[Ale+83] A. Alekseev, A. Basharov, and V. Beloborodov. "Photon-echo quantum beats in a magnetic field". In: *Journal of Physics B: Atomic and Molecular Physics* 16.24 (1983), p. 4697.

[Alf01] Z. I. Alferov. "Nobel Lecture: The double heterostructure concept and its applications in physics, electronics, and technology". en. In: *Reviews of Modern Physics* 73.3 (2001), pp. 767–782. DOI: 10.1103/RevModPhys.73.767.

[Alf+76] Z. I. Alferov, D. Garbuzov, V. S. Grigor'ev, et al. "Injection luminescence of epitaxial heterojunctions in the GaP-GaAs system". In: *Sov. Phys. Solid State* 9 (1976), p. 208.

[Alf98] Z. I. Alferov. "The history and future of semiconductor heterostructures". en. In: *Semiconductors* 32.1 (1998), pp. 1–14. DOI: 10.1134/1.1187350.

[AS82] Y. Arakawa and H. Sakaki. "Multidimensional quantum well laser and temperature dependence of its threshold current". In: *Applied physics letters* 40.11 (1982), pp. 939–941.

[Aws+02] D. D. Awschalom, D. Loss, and N. Samarth. *Semiconductor Spintronics and Quantum Computation*. Berlin: Springer, 2002.

[Bar+18] J. G. Bartholomew, T. Zhong, J. M. Kindem, R. Lopez-Rios, J. Rochman, I. Craiciu, E. Miyazono, and A. Faraon. "Controlling rare-earth ions in a nanophotonic resonator using the ac Stark shift". In: *Physical Review A* 97.6 (2018). Publisher: American Physical Society, p. 063854. DOI: 10.1103/PhysRevA.97.063854.

[Bay19] M. Bayer. "Bridging Two Worlds: Colloidal versus Epitaxial Quantum Dots". en. In: *Annalen der Physik* 531.6 (2019), p. 1900039. DOI: https://doi.org/10.1002/andp.201900039.

[Bec+15] A. Bechtold, D. Rauch, F. Li, et al. "Three-stage decoherence dynamics of an electron spin qubit in an optically active quantum dot". In: *Nature Physics* 11.12 (2015), pp. 1005–1008.

[BF02] M Bayer and A. Forchel. "Temperature dependence of the exciton homogeneous linewidth in In 0.60 Ga 0.40 As/GaAs self-assembled quantum dots". In: *Physical Review B* 65.4 (2002), p. 041308.

[Bir+75] G. Bir, A. Aronov, and G. Pikus. "Spin relaxation of electrons due to scattering by holes". In: *Zh. Eksp. Teor. Fiz* 69.4 (1975), p. 1382.

[BM11] P. R. Berman and V. S. Malinovsky. *Principles of Laser Spectroscopy and Quantum Optics*. en. Google-Books-ID: YLumDwAAQBAJ. Princeton University Press, 2011.

[Bol+17] A. S. Bolshakov, V. V. Chaldyshev, E. E. Zavarin, A. V. Sakharov, W. V. Lundin, A. F. Tsatsulnikov, and M. A. Yagovkina. "Room temperature exciton-polariton resonant reflection and suppressed absorption in periodic systems of InGaN quantum wells". en. In: *Journal of Applied Physics* 121.13 (2017), p. 133101. DOI: 10.1063/1.4979636.

[Bon+98] N. H. Bonadeo, J. Erland, D. Gammon, D. Park, D. S. Katzer, and D. G. Steel. "Coherent Optical Control of the Quantum State of a Single Quantum Dot". en. In: *Science* 282.5393 (1998). Publisher: American Association for the Advancement of Science Section: Report, pp. 1473–1476. DOI: 10.1126/science.282.5393.1473.

[Bor+01] P. Borri, W. Langbein, S. Schneider, U. Woggon, R. L. Sellin, D. Ouyang, and D. Bimberg. "Ultralong Dephasing Time in InGaAs Quantum Dots". In: *Physical Review Letters* 87.15 (2001). Publisher: American Physical Society, p. 157401. DOI: 10.1103/PhysRevLett.87.157401.

[Bri+09] A. Bristow, D Karaiskaj, X Dai, T Zhang, C Carlsson, K. Hagen, R Jimenez, and S. Cundiff. "A versatile ultrastable platform for optical multidimensional Fourier-transform spectroscopy". In: *Review of Scientific Instruments* 80.7 (2009), p. 073108.

[Cap87] F. Capasso. "Band-Gap Engineering: From Physics and Materials to New Semiconductor Devices". en. In: *Science* 235.4785 (1987), pp. 172–176. DOI: 10.1126/science.235.4785.172.

[Car+06] S. G. Carter, Z. Chen, and S. T. Cundiff. "Optical Measurement and Control of Spin Diffusion in n-Doped GaAs Quantum Wells". In: *Physical Review Letters* 97.13 (2006). Publisher: American Physical Society, p. 136602. DOI: 10.1103/PhysRevLett.97.136602.

[Car+84] N. W. Carlson, W. R. Babbitt, Y. S. Bai, and T. W. Mossberg. "Field-inhibited optical dephasing and shape locking of photon echoes". EN. In: *Optics Letters* 9.6 (1984). Publisher: Optical Society of America, pp. 232–234. DOI: 10.1364/OL.9.000232.

[CH15] T. ChaneliÃšre and G. HÃ©tet. "Light-shift-modulated photon-echo". EN. In: *Optics Letters* 40.7 (2015). Publisher: Optical Society of America, pp. 1294–1297. DOI: 10.1364/OL.40.001294.

[CM13] S. T. Cundiff and S. Mukamel. "Optical multidimensional coherent spectroscopy". In: *Phys. Today* 66.7 (2013), pp. 44–49.

[CP54] H. Y. Carr and E. M. Purcell. "Effects of Diffusion on Free Precession in Nuclear Magnetic Resonance Experiments". In: *Physical Review* 94.3 (1954). Publisher: American Physical Society, pp. 630–638. DOI: 10.1103/PhysRev.94.630.

[CS01] D. Chemla and J. Shah. "Many-body and correlation effects in semiconductors". In: *Nature* 411.6837 (2001), pp. 549–557.

[Dat97] S. Datta. *Electronic transport in mesoscopic systems*. Cambridge university press, 1997.

[DG+13] K. De Greve, D. Press, P. L. McMahon, and Y. Yamamoto. "Ultrafast optical control of individual quantum dot spin qubits". In: *Reports on Progress in physics* 76.9 (2013), p. 092501.

[DK08] M. I. Dyakonov and A. Khaetskii. *Spin physics in semiconductors*. Vol. 157. Springer, 2008.

[DK11] M. I. Dyakonov and A. Khaetskii. *Spin Physics in Semiconductors*. Vol. 1. Berlin: Springer, 2011.

[DP54] M. Dyakonov and V. Perel. "Theory of optical spin orientation of electrons". In: *Teor. Fiz* 60 (1954), p. 1971.

[DP72] M. Dyakonov and V. Perel. "Spin relaxation of conduction electrons in noncentrosymmetric semiconductors". In: *Soviet Physics Solid State, Ussr* 13.12 (1972), pp. 3023–3026.

[Dre55] G. Dresselhaus. "Spin-orbit coupling effects in zinc blende structures". In: *Physical Review* 100.2 (1955), p. 580.

[Dzh+02] R. I. Dzhioev, K. V. Kavokin, V. L. Korenev, et al. "Low-temperature spin relaxation in n-type GaAs". In: *Physical Review B* 66.24 (2002). Publisher: American Physical Society, p. 245204. DOI: 10.1103/PhysRevB.66.245204.

[EE82] A. Efros and A. Efros. "Interband Light Absorption in Semiconductor Spheres". In: *Soviet physics. Semiconductors* 16 (1982), pp. 772–775.

[Eki+85] A. I. Ekimov, A. L. Efros, and A. A. Onushchenko. "Quantum size effect in semiconductor microcrystals". In: *Solid State Communications* 56.11 (1985), pp. 921–924.

[Ell54] R. J. Elliott. "Theory of the effect of spin-orbit coupling on magnetic resonance in some semiconductors". In: *Physical Review* 96.2 (1954), p. 266.

[Fli+04] T. Flissikowski, A. Betke, I. A. Akimov, and F. Henneberger. "Two-Photon Coherent Control of a Single Quantum Dot". In: *Physical Review Letters* 92.22 (2004). Publisher: American Physical Society, p. 227401. DOI: 10.1103/PhysRevLett.92.227401.

[Fox06] M. Fox. *Quantum Optics: An Introduction*. en. OUP Oxford, 2006.

[FS04] L. B. Freund and S. Suresh. *Thin film materials: stress, defect formation and surface evolution*. Cambridge university press, 2004.

[GI08] M. Glazov and E. Ivchenko. "Resonant spin amplification in nanostructures with anisotropic spin relaxation and spread of the electronic g factor". In: *Semiconductors* 42.8 (2008), pp. 951–957.

[Gil+21] G. Gillard, I. M. Griffiths, G. Ragunathan, A. Ulhaq, C. McEwan, E. Clarke, and E. A. Chekhovich. "Fundamental limits of electron and nuclear spin qubit lifetimes in an isolated self-assembled quantum dot". In: *npj Quantum Information* 7.1 (2021), p. 43.

[Gla12] M. M. Glazov. "Coherent spin dynamics of electrons and excitons in nanostructures (a review)". en. In: *Physics of the Solid State* 54.1 (2012), pp. 1–27. DOI: 10.1134/S1063783412010143.

[Gla15] M. Glazov. "Spin noise of localized electrons: Interplay of hopping and hyperfine interaction". In: *Physical Review B* 91.19 (2015), p. 195301.

[Gla18] M. M. Glazov. *Electron & Nuclear Spin Dynamics in Semiconductor Nanostructures*. eng. Series on Semiconductor Science and Technology. Oxford: Oxford University Press, 2018. DOI: 10.1093/oso/9780198807308.001.0001.

[Gre+06a] A. Greilich, D. R. Yakovlev, A. Shabaev, et al. "Mode Locking of Electron Spin Coherences in Singly Charged Quantum Dots". en. In: *Science* 313.5785 (2006), pp. 341–345. DOI: 10.1126/science.1128215.

[Gre+06b] A. Greilich, R Oulton, E. Zhukov, et al. "Optical control of spin coherence in singly charged (In, Ga) As/GaAs quantum dots". In: *Physical review letters* 96.22 (2006), p. 227401.

[Gre+09] A. Greilich, D. R. Yakovlev, and M. Bayer. "Optical tailoring of electron spin coherence in quantum dots". In: *Solid state communications* 149.35-36 (2009), pp. 1466–1471.

[Gri+22] S. Grisard, H. Rose, A. V. Trifonov, et al. "Multiple Rabi rotations of trions in InGaAs quantum dots observed by photon echo spectroscopy with spatially shaped laser pulses". In: *Phys. Rev. B* 106 (20 2022), p. 205408. DOI: 10.1103/PhysRevB.106.205408.

[Gru02] M. Grundmann. *Nano-optoelectronics: concepts, physics and devices*. Springer Science & Business Media, 2002.

[Gru10] M. Grundmann. *Physics of semiconductors*. Vol. 11. Springer, 2010.

[Gru+95] M. Grundmann, O. Stier, and D. Bimberg. "InAs/GaAs pyramidal quantum dots: Strain distribution, optical phonons, and electronic structure". In: *Physical Review B* 52.16 (1995), p. 11969.

[Gup+01] J. A. Gupta, R. Knobel, N. Samarth, and D. D. Awschalom. "Ultrafast Manipulation of Electron Spin Coherence". en. In: *Science* 292.5526 (2001), pp. 2458–2461. DOI: 10.1126/science.1061169.

[Hah50] E. L. Hahn. "Spin echoes". In: *Physical review* 80.4 (1950), p. 580.

[Ham17] B. S. Ham. "A controlled ac Stark echo for quantum memories". en. In: *Scientific Reports* 7.1 (2017). Number: 1 Publisher: Nature Publishing Group, p. 7655. DOI: 10.1038/s41598-017-08051-5.

[Han24] W. Hanle. "Über magnetische beeinflussung der polarisation der resonanzfluoreszenz". In: *Zeitschrift für Physik* 30.1 (1924), pp. 93–105.

[Har68] S. Hartmann. "Photon, spin, and Raman echoes". In: *IEEE Journal of Quantum Electronics* 4.11 (1968). Conference Name: IEEE Journal of Quantum Electronics, pp. 802–807. DOI: 10.1109/JQE.1968.1075009.

[He+21] J. He, W.-C. Cheng, Q. Wang, K. Cheng, H. Yu, and Y. Chai. "Recent advances in GaN-based power HEMT devices". In: *Advanced Electronic Materials* 7.4 (2021), p. 2001045.

[Hei+98] F Heinrichsdorff, M Grundmann, O Stier, A Krost, and D Bimberg. "Influence of In/Ga intermixing on the optical properties of InGaAs/GaAs quantum dots". In: *Journal of crystal growth* 195.1-4 (1998), pp. 540–545.

[HH62] S. R. Hartmann and E. L. Hahn. "Nuclear Double Resonance in the Rotating Frame". In: *Physical Review* 128.5 (1962). Publisher: American Physical Society, pp. 2042–2053. DOI: 10.1103/PhysRev.128.2042.

[Hto+02] H Htoon, T Takagahara, D Kulik, O Baklenov, A. Holmes Jr, and C. Shih. "Interplay of Rabi oscillations and quantum interference in semiconductor quantum dots". In: *Physical review letters* 88.8 (2002), p. 087401.

[Hut+18] L Huthmacher, R Stockill, E Clarke, M. Hugues, C. Le Gall, and M Atatüre. "Coherence of a dynamically decoupled quantum-dot hole spin". In: *Physical Review B* 97.24 (2018), p. 241413.

[Ima+99] A Imamog, D. D. Awschalom, G. Burkard, D. P. DiVincenzo, D. Loss, M Sherwin, A Small, et al. "Quantum information processing using quantum dot spins and cavity QED". In: *Physical review letters* 83.20 (1999), p. 4204.

[Jof+88] M. Joffre, C. B. la Guillaume, N. Peyghambarian, M. Lindberg, D. Hulin, A. Migus, S. W. Koch, and A. Antonetti. "Coherent effects in pumpâprobe spectroscopy of excitons". en. In: *Optics Letters* 13.4 (1988), p. 276. DOI: 10.1364/OL.13.000276.

[KA98] J. Kikkawa and D. Awschalom. "Resonant spin amplification in n-type GaAs". In: *Physical Review Letters* 80.19 (1998), p. 4313.

[Kal+15] A. M. Kalashnikova, A. V. Kimel, and R. V. Pisarev. "Ultrafast opto-magnetism". en. In: *Physics-Uspekhi* 58.10 (2015). Publisher: IOP Publishing, p. 969. DOI: 10.3367/UFNe.0185.201510j.1064.

[Kam+20] A. Kamenskii, M. Y. Petrov, G. Kozlov, et al. "Detection and amplification of spin noise using scattered laser light in a quantum-dot microcavity". In: *Physical Review B* 101.4 (2020), p. 041401.

[Kan57] E. O. Kane. "Band structure of indium antimonide". In: *Journal of Physics and Chemistry of Solids* 1.4 (1957), pp. 249–261.

[Kav08] K. Kavokin. "Spin relaxation of localized electrons in n-type semiconductors". In: *Semiconductor Science and Technology* 23.11 (2008), p. 114009.

[KC21] A. Kosarev and V. Chaldyshev. "Carrier Localization by a Quantum Dot in a Quantum Well". In: *Physical Review Applied* 16.4 (2021), p. 044046.

[Kil01] J. S. C. Kilby. "Turning potential into realities: The invention of the integrated circuit (Nobel lecture)". In: *ChemPhysChem* 2.8-9 (2001), pp. 482–489.

[Kim+11] D. Kim, S. G. Carter, A. Greilich, A. S. Bracker, and D. Gammon. "Ultrafast optical control of entanglement between two quantum-dot spins". In: *Nature Physics* 7.3 (2011), pp. 223–229.

[Kir+22] E Kirstein, D. Yakovlev, M. Glazov, et al. "The Landé factors of electrons and holes in lead halide perovskites: universal dependence on the band gap". In: *Nature Communications* 13.1 (2022), pp. 1–8.

[Kir+23] E Kirstein, N. Kopteva, D. Yakovlev, et al. "Mode locking of hole spin coherences in CsPb (Cl, Br) 3 perovskite nanocrystals". In: *Nature Communications* 14.1 (2023), p. 699.

[Kit05] C. Kittel. *Introduction to solid state physics*. en. 8th ed. Hoboken, NJ: Wiley, 2005.

[Kob+22] M. Kobecki, A. V. Scherbakov, S. M. Kukhtaruk, et al. “Giant photoelasticity of polaritons for detection of coherent phonons in a superlattice with quantum sensitivity”. In: *Physical Review Letters* 128.15 (2022), p. 157401.

[Kop+06] F. H. L. Koppens, C. Buizert, K. J. Tielrooij, I. T. Vink, K. C. Nowack, T. Meunier, L. P. Kouwenhoven, and L. M. K. Vandersypen. “Driven coherent oscillations of a single electron spin in a quantum dot”. en. In: *Nature* 442.7104 (2006), pp. 766–771. DOI: 10.1038/nature05065.

[Kor+09] J. D. Koralek, C. P. Weber, J. Orenstein, B. A. Bernevig, S.-C. Zhang, S. Mack, and D. D. Awschalom. “Emergence of the persistent spin helix in semiconductor quantum wells”. en. In: *Nature* 458.7238 (2009), pp. 610–613. DOI: 10.1038/nature07871.

[Kos+19] A. Kosarev, N. Bert, V. Nevedomskii, V. Chaldyshev, V. Preobrazhenskii, M. Putyato, and B. Semyagin. “Photoluminescence from InAs Quantum Dots Buried Under Low-Temperature-Grown GaAs”. In: *physica status solidi (b)* 256.5 (2019), p. 1800479.

[Kos+20] A. N. Kosarev, H. Rose, S. V. Poltavtsev, et al. “Accurate photon echo timing by optical freezing of exciton dephasing and rephasing in quantum dots”. In: *Communications Physics* 3.1 (2020), pp. 1–9.

[Kos+22] A. N. Kosarev, A. V. Trifonov, I. A. Yugova, et al. “Extending the time of coherent optical response in ensemble of singly-charged InGaAs quantum dots”. In: *Communications Physics* 5.1 (2022), pp. 1–7.

[Kr05] A. Krügel, V. Axt, T. Kuhn, P. Machnikowski, and A. Vagov. “The role of acoustic phonons for Rabi oscillations in semiconductor quantum dots”. en. In: *Applied Physics B* 81.7 (2005), pp. 897–904. DOI: 10.1007/s00340-005-1984-1.

[Kro01] H. Kroemer. “Nobel Lecture: Quasielectric fields and band offsets: teaching electrons new tricks”. In: *Reviews of modern physics* 73.3 (2001), p. 783.

[Kro+04] M. Kroutvar, Y. Ducommun, D. Heiss, M. Bichler, D. Schuh, G. Abstreiter, and J. J. Finley. “Optically programmable electron spin memory using semiconductor quantum dots”. In: *Nature* 432.7013 (2004), pp. 81–84.

[Kur+07] K Kuroda, T Kuroda, K Watanabe, T Mano, K Sakoda, G Kido, and N Koguchi. “Final-state readout of exciton qubits by observing resonantly excited photoluminescence in quantum dots”. In: *Applied Physics Letters* 90.5 (2007), p. 051909.

[Kur+64] N. Kurnit, I. Abella, and S. Hartmann. “Observation of a photon echo”. In: *Physical Review Letters* 13.19 (1964), p. 567.

[Lan+12] L. Langer, S. V. Poltavtsev, I. A. Yugova, et al. "Magnetic-Field Control of Photon Echo from the Electron-Trion System in a CdTe Quantum Well: Shuffling Coherence between Optically Accessible and Inaccessible States". In: *Physical Review Letters* 109.15 (2012). Publisher: American Physical Society, p. 157403. DOI: 10.1103/PhysRevLett.109.157403.

[Lan+14] L. Langer, S. V. Poltavtsev, I. A. Yugova, et al. "Access to long-term optical memories using photon echoes retrieved from semiconductor spins". en. In: *Nature Photonics* 8.11 (2014), pp. 851–857. DOI: 10.1038/nphoton.2014.219.

[Li+03] X. Li, Y. Wu, D. Steel, et al. "An all-optical quantum gate in a semiconductor quantum dot". In: *Science* 301.5634 (2003), pp. 809–811.

[Li+21] L. Li, C. Hu, and G. Shen. "Low-Dimensional Nanostructure Based Flexible Photodetectors: Device Configuration, Functional Design, Integration, and Applications". In: *Accounts of Materials Research* 2.10 (2021), pp. 954–965.

[Lvo+09] A. I. Lvovsky, B. C. Sanders, and W. Tittel. "Optical quantum memory". en. In: *Nature Photonics* 3.12 (2009). Number: 12 Publisher: Nature Publishing Group, pp. 706–714. DOI: 10.1038/nphoton.2009.231.

[MB74] J. Matthews and A. Blakeslee. "Defects in epitaxial multilayers: I. Misfit dislocations". In: *Journal of Crystal growth* 27 (1974), pp. 118–125.

[MC65] H. W. Mocker and R. Collins. "Mode competition and self-locking effects in aq-switched ruby laser". In: *Applied Physics Letters* 7.10 (1965), pp. 270–273.

[Mer+02] I. Merkulov, A. L. Efros, and M Rosen. "Electron spin relaxation by nuclei in semiconductor quantum dots". In: *Physical review B* 65.20 (2002), p. 205309.

[MG19] C.-T. Ma and Z.-H. Gu. "Review of GaN HEMT applications in power converters over 500 W". In: *Electronics* 8.12 (2019), p. 1401.

[MG58] S. Meiboom and D. Gill. "Modified SpinâEcho Method for Measuring Nuclear Relaxation Times". In: *Review of Scientific Instruments* 29.8 (1958). Publisher: American Institute of Physics, pp. 688–691. DOI: 10.1063/1.1716296.

[MH00] A Malinowski and R. Harley. "Anisotropy of the electron g factor in lattice-matched and strained-layer III-V quantum wells". In: *Physical Review B* 62.3 (2000), p. 2051.

[Mon+13] L. Monniello, C. Tonin, R. Hostein, A. Lemaitre, A. Martinez, V. Voliotis, and R. Grousson. "Excitation-Induced Dephasing in a Resonantly Driven $\mathrm{InAs}/\mathrm{GaAs}$ Quantum Dot". In: *Physical Review Letters* 111.2 (2013). Publisher: American Physical Society, p. 026403. DOI: 10.1103/PhysRevLett.111.026403.

[Moo+11] G Moody, M. Siemens, A. Bristow, X Dai, A. Bracker, D Gammon, and S. Cundiff. "Exciton relaxation and coupling dynamics in a GaAs/Al x Ga 1- x As quantum well and quantum dot ensemble". In: *Physical Review B* 83.24 (2011), p. 245316.

[Moo+65] G. E. Moore et al. *Cramming more components onto integrated circuits*. 1965.

[Mos+79] T. Mossberg, A Flusberg, R Kachru, and S. Hartmann. "Total scattering cross section for Na on He measured by stimulated photon echoes". In: *Physical Review Letters* 42.25 (1979), p. 1665.

[MZ84] F. Meier and B. P. Zakharchenya. *Optical Orientation*. New York: North-Holland, 1984.

[Nak15] S. Nakamura. "Nobel Lecture: Background story of the invention of efficient blue InGaN light emitting diodes". In: *Reviews of Modern Physics* 87.4 (2015), p. 1139.

[Nis+17] K. Nishi, K. Takemasa, M. Sugawara, and Y. Arakawa. "Development of quantum dot lasers for data-com and silicon photonics applications". In: *IEEE Journal of Selected Topics in Quantum Electronics* 23.6 (2017), pp. 1–7.

[Nol+90] G Noll, U Siegner, S. Shevel, and E. Göbel. "Picosecond stimulated photon echo due to intrinsic excitations in semiconductor mixed crystals". In: *Physical review letters* 64.7 (1990), p. 792.

[Par69] R. Parsons. "Band-to-band optical pumping in solids and polarized photoluminescence". In: *Physical Review Letters* 23.20 (1969), p. 1152.

[Pas+18] F. Passmann, S. Anghel, T. Tischler, et al. "Persistent spin helix manipulation by optical doping of a CdTe quantum well". en. In: *Physical Review B* 97.20 (2018), p. 201413. DOI: 10.1103/PhysRevB.97.201413.

[PB55] G. Pearson and W. H. Brattain. "History of semiconductor research". In: *Proceedings of the IRE* 43.12 (1955), pp. 1794–1806.

[Pet+07] M. Y. Petrov, I. Ignatiev, S. Poltavtsev, A Greilich, A Bauschulte, D. Yakovlev, and M Bayer. "Effect of annealing on the hyperfine interaction in InAs/GaAs quantum dots". In: *arXiv preprint arXiv:0710.5091* (2007).

[Pol+16] S. V. Poltavtsev, M. Salewski, Y. V. Kapitonov, et al. "Photon echo transients from an inhomogeneous ensemble of semiconductor quantum dots". In: *Physical Review B* 93.12 (2016). Publisher: American Physical Society, p. 121304. DOI: 10.1103/PhysRevB.93.121304.

[Pol+17] S. V. Poltavtsev, M. Reichelt, I. A. Akimov, et al. "Damping of Rabi oscillations in intensity-dependent photon echoes from exciton complexes in a CdTe/(Cd,Mg)Te single quantum well". In: *Physical Review B* 96.7 (2017). Publisher: American Physical Society, p. 075306. DOI: 10.1103/PhysRevB.96.075306.

[Pol+18] S. V. Poltavtsev, I. A. Yugova, I. A. Akimov, D. R. Yakovlev, and M. Bayer. "Photon Echo from Localized Excitons in Semiconductor Nanostructures". en. In: *Physics of the Solid State* 60.8 (2018), pp. 1635–1644. DOI: 10.1134/S1063783418080188.

[Pol+19] S. V. Poltavtsev, Y. V. Kapitonov, I. A. Yugova, et al. "Polarimetry of photon echo on charged and neutral excitons in semiconductor quantum wells". en. In: *Scientific Reports* 9.1 (2019). Number: 1 Publisher: Nature Publishing Group, p. 5666. DOI: 10.1038/s41598-019-42208-8.

[Pol+20a] S. Poltavtsev, I. Yugova, I. A. Babenko, et al. "Quantum beats in the polarization of the spin-dependent photon echo from donor-bound excitons in CdTe/(Cd, Mg) Te quantum wells". In: *Physical Review B* 101.8 (2020), p. 081409.

[Pol+20b] S. Poltavtsev, I. Yugova, A. Kosarev, et al. "In-plane anisotropy of the hole g factor in CdTe/(Cd, Mg) Te quantum wells studied by spin-dependent photon echoes". In: *Physical Review Research* 2.2 (2020), p. 023160.

[Pre+08] D. Press, T. D. Ladd, B. Zhang, and Y. Yamamoto. "Complete quantum control of a single quantum dot spin using ultrafast optical pulses". en. In: *Nature* 456.7219 (2008), pp. 218–221. DOI: 10.1038/nature07530.

[Pri+22] M. B. Price, P. A. Hume, A. Ilina, et al. "Free charge photogeneration in a single component high photovoltaic efficiency organic semiconductor". In: *Nature Communications* 13.1 (2022), pp. 1–10.

[Ram+10] A. Ramsay, T. Godden, S. Boyle, E. M. Gauger, A. Nazir, B. W. Lovett, A. Fox, and M. Skolnick. "Phonon-induced Rabi-frequency renormalization of optically driven single InGaAs/GaAs quantum dots". In: *Physical review letters* 105.17 (2010), p. 177402.

[Rod+20] S. Rodt, S. Reitzenstein, and T. Heindel. "Deterministically fabricated solid-state quantum-light sources". In: *Journal of Physics: Condensed Matter* 32.15 (2020), p. 153003.

[Ros18] H. Rose. "Numerische Simulationen zum Multi-Wellen-Mischen an Ensemblen von Zwei-Niveau-Systemen". Bachelor Thesis. Universit\"at Paderborn, 2018.

[Rub+04] N. Rubtsova, V. Ishchenko, E. Khvorostov, S. Kochubei, V. Reshetov, and I. Yevseyev. "Non-Faraday rotation of photon-echo polarization in ytterbium vapor". In: *Physical Review A* 70.2 (2004), p. 023403.

[Sae+18] F Saeed, M Kuhnert, I. Akimov, et al. "Single-beam optical measurement of spin dynamics in CdTe/(Cd, Mg) Te quantum wells". In: *Physical Review B* 98.7 (2018), p. 075308.

[Sal+17a] M. Salewski, S. V. Poltavtsev, Y. V. Kapitonov, et al. "Photon echoes from (In,Ga)As quantum dots embedded in a Tamm-plasmon microcavity". In: *Physical Review B* 95.3 (2017). Publisher: American Physical Society, p. 035312. DOI: 10.1103/PhysRevB.95.035312.

[Sal+17b] M. Salewski, S. Poltavtsev, I. Yugova, et al. "High-Resolution Two-Dimensional Optical Spectroscopy of Electron Spins". In: *Physical Review X* 7.3 (2017). Publisher: American Physical Society, p. 031030. DOI: 10.1103/PhysRevX.7.031030.

[Sam+78] V. Samartsev, R. Usmanov, G. Ershov, and B Sh. "Advance and delay effects in photon echo signals". In: *JETP* 47 (1978), p. 1030.

[Sch+85] L Schultheis, M. Sturge, and J Hegarty. "Photon echoes from two-dimensional excitons in GaAs-AlGaAs quantum wells". In: *Applied physics letters* 47.9 (1985), pp. 995–997.

[Sel+20] G. S. Selopal, H. Zhao, Z. M. Wang, and F. Rosei. "Core/shell quantum dots solar cells". In: *Advanced Functional Materials* 30.13 (2020), p. 1908762.

[Ser+12] L. Seravalli, G. Trevisi, and P. Frigeri. "Design and growth of metamorphic InAs/InGaAs quantum dots for single photon emission in the telecom window". In: *CrystEngComm* 14.20 (2012), pp. 6833–6838.

[Sha+79] C. V. Shank, R. L. Fork, R. F. Leheny, and J. Shah. "Dynamics of Photoexcited GaAs Band-Edge Absorption with Subpicosecond Resolution". en. In: *Physical Review Letters* 42.2 (1979), pp. 112–115. DOI: 10.1103/PhysRevLett.42.112.

[Sha+87] J. Shah, B. Deveaud, T. C. Damen, W. T. Tsang, A. C. Gossard, and P. Lugli. "Determination of intervalley scattering rates in GaAs by subpicosecond luminescence spectroscopy". en. In: *Physical Review Letters* 59.19 (1987), pp. 2222–2225. DOI: 10.1103/PhysRevLett.59.2222.

[Sha99] J. Shah. *Ultrafast Spectroscopy of Semiconductors and Semiconductor Nanostructures*. Vol. 115. Springer Series in Solid-State Sciences. New York: Springer Science \& Business Media, 1999.

[Sho56] W. Shockley. "Transistor technology evokes new physics". In: *Nobel lecture* 11 (1956).

[Sie+10] M. E. Siemens, G. Moody, H. Li, A. D. Bristow, and S. T. Cundiff. "Resonance lineshapes in two-dimensional Fourier transform spectroscopy". In: *Optics express* 18.17 (2010), pp. 17699–17708.

[Sim+11] C.-M. Simon, T. Belhadj, B. Chatel, et al. "Robust Quantum Dot Exciton Generation via Adiabatic Passage with Frequency-Swept Optical Pulses". In: *Physical Review Letters* 106.16 (2011). Publisher: American Physical Society, p. 166801. DOI: 10.1103/PhysRevLett.106.166801.

[Sir+97] A. Sirenko, T Ruf, M Cardona, D. Yakovlev, W Ossau, A Waag, and G Landwehr. "Electron and hole g factors measured by spin-flip Raman scattering in CdTe/Cd 1- x Mg x Te single quantum wells". In: *Physical Review B* 56.4 (1997), p. 2114.

[SK37] I. N. Stranski and L. Krastanow. "Zur Theorie der orientierten Ausscheidung von Ionenkristallen aufeinander". In: *Monatshefte für Chemie und verwandte Teile anderer Wissenschaften* 71 (1937), pp. 351–364.

[Sle+86] E. T. Sleva, I. M. Xavier, and A. H. Zewail. "Photon locking". EN. In: *JOSA B* 3.4 (1986). Publisher: Optical Society of America, pp. 483–487. DOI: 10.1364/JOSAB.3.000483.

[Sli13] C. P. Slichter. *Principles of Magnetic Resonance*. en. Springer Science & Business Media, 2013.

[Sog+16] T. Sogabe, Q. Shen, and K. Yamaguchi. "Recent progress on quantum dot solar cells: a review". In: *Journal of Photonics for Energy* 6.4 (2016), pp. 040901–040901.

[Spi+16] F Spitzer, B. Glavin, V. Belotelov, et al. "Enhancement of electron hot spot relaxation in photoexcited plasmonic structures by thermal diffusion". In: *Physical Review B* 94.20 (2016), p. 201118.

[Sta+04] J. Stangl, V. Holỳ, and G. Bauer. "Structural properties of self-organized semiconductor nanostructures". In: *Reviews of modern physics* 76.3 (2004), p. 725.

[Sti+01] T. H. Stievater, X. Li, D. G. Steel, D. Gammon, D. S. Katzer, D. Park, C. Piermarocchi, and L. J. Sham. "Rabi Oscillations of Excitons in Single Quantum Dots". en. In: *Physical Review Letters* 87.13 (2001), p. 133603. DOI: 10.1103/PhysRevLett.87.133603.

[Stu+06] S. Stufler, P. Ester, A. Zrenner, and M. Bichler. "Ramsey Fringes in an Electric-Field-Tunable Quantum Dot System". In: *Physical Review Letters* 96.3 (2006). Publisher: American Physical Society, p. 037402. DOI: 10.1103/PhysRevLett.96.037402.

[Suz+16] T. Suzuki, R. Singh, M. Bayer, A. Ludwig, A. D. Wieck, and S. T. Cundiff. "Coherent Control of the Exciton-Biexciton System in an InAs Self-Assembled Quantum Dot Ensemble". In: *Physical Review Letters* 117.15 (2016). Publisher: American Physical Society, p. 157402. DOI: 10.1103/PhysRevLett.117.157402.

[SZ97] M. Scully and M. Zubairy. *Quantum Optics*. Cambridge Univ. Press, 1997.

[Tho+86] C Thomsen, H. T. Grahn, H. J. Maris, and J. Tauc. "Surface generation and detection of phonons by picosecond light pulses". In: *Physical Review B* 34.6 (1986), p. 4129.

[Tit+10] W. Tittel, M. Afzelius, T. Chaneliere, R. L. Cone, S. Kröll, S. A. Moiseev, and M. Sellars. "Photon-echo quantum memory in solid state systems". In: *Laser & Photonics Reviews* 4.2 (2010), pp. 244–267.

[Tok+06] Y. Tokura, W. G. van der Wiel, T. Obata, and S. Tarucha. "Coherent Single Electron Spin Control in a Slanting Zeeman Field". en. In: *Physical Review Letters* 96.4 (2006), p. 047202. DOI: 10.1103/PhysRevLett.96.047202.

[Tri+21] A. Trifonov, I. Akimov, L. Golub, et al. "Strong enhancement of heavy-hole Land\'e factor q in InGaAs symmetric quantum dots revealed by coherent optical spectroscopy". In: *arXiv preprint arXiv:2103.13653* (2021).

[TS74] N Takeuchi and A Szabo. "Observation of photon echoes using a nitrogen laser pumped dye laser". In: *Physics Letters A* 50.5 (1974), pp. 361–362.

[Vas+10] S. Michaelis de Vasconcellos, S. Gordon, M. Bichler, T. Meier, and A. Zrenner. "Coherent control of a single exciton qubit by optoelectronic manipulation". en. In: *Nature Photonics* 4.8 (2010). Number: 8 Publisher: Nature Publishing Group, pp. 545–548. DOI: 10.1038/nphoton.2010.124.

[Vol82] A. Volta. "XVI. Del modo di render sensibilissima la più debole elettricità sia natural, sia artificiale". In: *Philosophical Transactions of the Royal Society of London* 72 (1782), pp. 237–280.

[Web+91] M. D. Webb, S. T. Cundiff, and D. G. Steel. "Observation of time-resolved picosecond stimulated photon echoes and free polarization decay in GaAs/AlGaAs multiple quantum wells". In: *Physical Review Letters* 66.7 (1991). Publisher: American Physical Society, pp. 934–937. DOI: 10.1103/PhysRevLett.66.934.

[Wig+18] D. Wigger, C. Schneider, S. Gerhardt, M. Kamp, S. HÃ¶fling, T. Kuhn, and J. Kasprzak. "Rabi oscillations of a quantum dot exciton coupled to acoustic phonons: coherence and population readout". EN. In: *Optica* 5.11 (2018). Publisher: Optical Society of America, pp. 1442–1450. DOI: 10.1364/OPTICA.5.001442.

[Wu+11] Y. Wu, I. M. Piper, M. Ediger, et al. "Population Inversion in a Single InGaAs Quantum Dot Using the Method of Adiabatic Rapid Passage". In: *Physical Review Letters* 106.6 (2011). Publisher: American Physical Society, p. 067401. DOI: 10.1103/PhysRevLett.106.067401.

[Yaf63] Y Yafet. "g Factors and spin-lattice relaxation of conduction electrons". In: *Solid state physics*. Vol. 14. Elsevier, 1963, pp. 1–98.

[Yan+20] J. Yang, M. K. Choi, U. J. Yang, S. Y. Kim, Y. S. Kim, J. H. Kim, D.-H. Kim, and T. Hyeon. "Toward full-color electroluminescent quantum dot displays". In: *Nano Letters* 21.1 (2020), pp. 26–33.

[Yan+21] Z. Yang, T. Albrow-Owen, W. Cai, and T. Hasan. "Miniaturization of optical spectrometers". In: *Science* 371.6528 (2021), eabe0722.

[Yod+84] A. G. Yodh, J. Golub, N. W. Carlson, and T. W. Mossberg. "Optically Inhibited Collisional Dephasing". In: *Physical Review Letters* 53.7 (1984). Publisher: American Physical Society, pp. 659–662. DOI: 10.1103/PhysRevLett.53.659.

[Zho+17] T. Zhong, J. M. Kindem, J. G. Bartholomew, et al. "Nanophotonic rare-earth quantum memory with optically controlled retrieval". In: *Science* 357.6358 (2017), pp. 1392–1395.

[Zhu+06] E. Zhukov, D. Yakovlev, M Bayer, G Karczewski, T Wojtowicz, and J Kossut. "Spin coherence of two-dimensional electron gas in CdTe/(Cd, Mg) Te quantum wells". In: *physica status solidi (b)* 243.4 (2006), pp. 878–881.

[Zhu+07] E. A. Zhukov, D. R. Yakovlev, M. Bayer, M. M. Glazov, E. L. Ivchenko, G. Karczewski, T. Wojtowicz, and J. Kossut. "Spin coherence of a two-dimensional electron gas induced by resonant excitation of trions and excitons in Cd Te/(Cd, Mg) Te quantum wells". In: *Physical Review B* 76.20 (2007). Publisher: American Physical Society, p. 205310. DOI: 10.1103/PhysRevB.76.205310.

[Zre+02] A. Zrenner, E Beham, S Stufler, F Findeis, M Bichler, and G. Abstreiter. "Coherent properties of a two-level system based on a quantum-dot photodiode". In: *Nature* 418.6898 (2002), pp. 612–614.